To the Graduate Council:

I am submitting herewith a thesis written by Richard David Loewen entitled “Analysis of Cavity Flow and The Effects of a Rod in Crossflow.” I have examined the final electronic copy of this thesis for form and content and recommend that it be accepted in partial fulfillment of the requirements for the degree of Master of Science, with a major in Aerospace Engineering.

Ahmad D. Vakili, Major Professor

We have read this thesis
and recommend its acceptance:

Roy J. Schulz

Gary Flandro

Accepted for the Council:

Carolyn R. Hodges
Vice Provost and Dean of the Graduate School

(Original signatures are on file with official student records.)

# ANALYSIS OF CAVITY FLOW AND THE EFFECTS OF A ROD IN CROSSFLOW

A Thesis
Presented for the
Master of Science
Degree
The University of Tennessee, Knoxville

**RICHARD DAVID LOEWEN**

**DECEMBER 2008**

# DEDICATION

I dedicate this work to my paternal grandfather, David Cornelius Loewen, who through his encouragement and support motivated me to challenge myself and to pursue any educational opportunity that may arise.

To my daughters, Anna and Katie, I wish for each of you success in all your endeavours. May you find the courage, perseverance, and conviction to pursue your dreams and know that all things are possible. We offer you our love, support, and encouragement as you venture down the paths that lie ahead.

## ACKNOWLEDGEMENTS

I would like to thank each of the Faculty Professors, Staff Members, and Fellow Classmates who shared their expertise, offered assistance, and gave of themselves, throughout my time at the University of Tennessee Space Institute. You have given me a wealth of knowledge, experiences, and memories from which I will be able to draw upon and share with others as I face the journey ahead.

In particular, I express my sincere appreciation to Dr. Ahmad Vakili. As one of my Professors you taught me the basics and stressed the importance of ‘First Principles’, ‘Fundamental Equations’, ‘Non-Dimensional Analysis’, and ‘The Experimental Method’. As my Advisor you were more of a coach who pointed me in the right direction, encouraged me along the way, and didn’t let me stray to far off track before bringing me back on course. There were times along the way I wasn’t too sure how it would turn out, but you had the proper perspective and words to share that seemed to make it not look so bad. Thank you for your willingness to guide *another* Canadian student down the path of academic success.

To the Gas Dynamics Lab and Machine Shop personnel, Jim, Keith, Joel, Gary, and Chris, thank you for your efforts and cooperation in putting all the pieces together. Your individual contributions not only played an integral part in preparing for and completing the testing in a timely manner, but were greatly appreciated.

Last, but certainly not least, I thank my wife, Sandra, and daughters, Anna and Katie, for sharing this adventure with me. It wasn’t always easy, but together we made it through, even managed to have some fun along the way, and are that much stronger as a family.

# ABSTRACT

Subsonic cavity flow tests of an L/D = 3.5 cavity, with three different diameter rods in crossflow, 1/8", 3/16", and 1/4", were conducted using the High Speed Wind Tunnel in the University of Tennessee Space Institute's Gas Dynamic Laboratory. The average Mach number flow over the duration of the four phase testing sequence was 0.52, with a unit Reynolds number of 13.8 x $10^6$. With the use of a dynamic pressure transducer and a laser PIV system, Spectral and Flow Visualization data was collected with aim of investigating the effect of the rods in crossflow on cavity flow. However, for reasons beyond the control of this investigation, a converging-diverging supersonic nozzle was used in place of a subsonic nozzle. As a result, the separated, or near separated, flow on the diverging side of the nozzle created a region of low kinetic energy flow approximately 5 mm above the floor of the tunnel test section. Despite the presence of this undesirable feature, the Baseline cavity, without a rod in crossflow, was found to resonate at 1413 Hz and produced an average peak amplitude tone of 148.7 dB SPL. The effect of placing different diameter rods in the crossflow was to reduce the amount, and intensity, of shear layer interactions, by helping to loft the flow over the trailing edge of the cavity. The best results were achieved with a 1/4" diameter rod, which, on average, provided 15.1 dB SPL of acoustic suppression. It was concluded that the suppression observed in this particular experiment was the result of blockage and lofting effects, which helped the shear layer to span the length of the cavity and reduce the intensity of the shear layer interactions at the trailing edge.

# Table of Contents

# LIST OF TABLES

# LIST OF FIGURES

# NOMENCLATURE

| | |
|---|---|
| $D$ | - Cavity depth |
| $K_v$ | - Ratio of convective velocity of vortices to freestream velocity |
| $L$ | - Cavity length |
| $L/D$ | - Cavity length to depth ratio |
| $M$ | - Mach number |
| $S$ | - Strouhal number |
| $U$, $V$ | - Velocity |
| $W$ | - Cavity width |
| $W/D$ | - Cavity width to depth ratio |
| $c$ | - Speed of sound |
| $f$ | - Frequency |
| $m$ | - Mode number for cavity oscillations |
| $n$ | - Phase delay between acoustic wave and new vortex |
| $p$ | - Pressure |
| $\delta$ | - Boundary layer thickness |
| $\theta$ | - Momentum thickness |
| $\theta/L$ | - Shear layer thickness to length ratio |
| $\gamma$ | - Ratio of specific heats |

Subscripts

| | |
|---|---|
| $\infty$ | - Freestream |
| $c$ | - Convective |
| $o$ | - Stagnation |
| L | - Length |

# CHAPTER 1

# INTRODUCTION

## Background

Fluid passing over the opening of a confined space, or cavity, of an otherwise continuous body occurs in many different engineering applications and structures. Flows of this nature often result in undesirable flow patterns, increased drag, and potentially damaging pressure fluctuations. Rossiter [1] indicated that these “cavity flow” scenarios began to be investigated much more closely in the early 1950’s, with emphasis being placed on the flow over an aircraft cavity like a weapons bay. The study of cavity flow has also expanded to include application to solid rocket motors, where small fluctuations in pressure result in proportional fluctuations in thrust. A more common cavity flow example arises any time a vehicle is driven with a window or sunroof open. In this configuration, the vehicle interior volume acts like a cavity and with increasing velocity the flow over the opening will create a noticeable buffeting, which includes an increase in noise and varying flow conditions associated with pressure fluctuations occurring within the cabin. Not only can these side effects be uncomfortable for the occupants inside the automobile, but in the case of an aircraft where the velocities involved are much greater, Heller and Bliss [2] point out that the varying pressure fluctuations within a cavity can become significant and lead to structural fatigue or damage to sensitive components, including delicate sensors and weapons systems.

Over the last several decades a considerable effort has been put forth to grow the level of theoretical and physical understanding so that cavity flow problems may be approached in an intelligent manner and effective solutions designed to remedy the situation. While much of the early work focused on understanding the flow field dynamics and physical mechanisms that resulted in elevated pressure fluctuations, attention also quickly turned to designing potential suppression techniques that could be utilized to reduce the amplitude of those pressure fluctuations. Significant progress has been made, and a portion of this thesis is dedicated to reviewing some of the major advances and developments on both of those fronts.

Some of the more noteworthy contributions in the early understanding of the cavity flow problem and its physical processes were made by Krishnamurty [3] and Roshko [4], who were among the first to describe and define the problem.  Not long after, Rossiter [1] was one of the first to identify some of the relevant physical parameters and fluid properties when he presented an empirical model to represent the resonant frequencies identified by experimental measurements.  In the search to minimize the effects of the resonant pressure oscillations, early suppression methods involved adjusting the physical construction of the cavity by way of sloped, or even permeable, surfaces, while others introduced ramps and fences ahead of the cavity.  Those gave way to more robust methods like upstream mass injection and the rod in crossflow technique, while some of the most recent techniques have become relatively complex by incorporating both sensing instruments and feedback loops to create active control systems.

## Objective

For the purposes of this study, the rod in the crossflow technique is the focus of this investigation aimed at understanding how it affects the cavity shear layer and how it is able to suppress the amplitude of the resonant frequency.  With that as the basis, this thesis has two complementary objectives:

- To measure and compare the level of acoustic suppression offered by different diameter rods positioned in perpendicular crossflow above the leading edge of the cavity; and

- To use Particle Image Velocimetry (PIV), to examine the shear layer structure that develops in the subsonic flow over an open cavity with and without cylindrical rods of varying diameter positioned over the cavity leading edge.

## General Approach

The University of Tennessee Space Institute (UTSI) High Speed Wind Tunnel (HSWT) and TSI LASERPULSE Particle Image Velocimetry (PIV) system was used to complete four phases of testing that were identified as required to undertake this subsonic cavity flow study. Each phase of testing focused on the collection of acoustic sound pressure levels (dB SPL) measured by a dynamic pressure transducer as well as flow field velocity and vorticity characteristics imaged and processed using the aforementioned PIV system. A detailed description of the UTSI HSWT design and setup, along with all other associated test apparatus and models, is provided in Chapter 3. Preliminary testing in the early months of this study offered the opportunity to become familiar with the operation of the HSWT and PIV systems. This early testing also identified that a cavity with length to depth ratio, L/D, of 3.5 would create resonant tones at a flow Mach number around 0.55.

With the test conditions determined, the first phase of testing involved operating the tunnel in a "Clean" configuration. Without a cavity or any other model in the test section it was possible to obtain an initial assessment of the acoustic and flow field characteristics of the tunnel. Collection of this clean test section data helped to identify any peculiarities in the flow that were inherent to the existing setup of the tunnel, and was useful for comparison to data collected in each of the other phases.

The goal of the second phase was to collect the acoustic and wake "Signature(s)" resulting from introduction of a single circular rod of chosen diameter into the crossflow of a subsonic, M = 0.55, Mach number flow upstream of the cavity. This phase of testing required that supports be used to mount one cylindrical rod at a time into the test section. The rods were centered over the location where the leading edge of the cavity would begin and at a height determined by the flow field conditions observed in the preliminary stages of testing.

The third phase of testing was conducted with just a cavity installed into the test section by way of a removable floor plate, and was referred to as the “Baseline” configuration. The rectangular cavity under test had a length to depth ratio, $L/D = 3.5$, and width to depth ratio, $W/D = 2$. The dimensions of the cavity and a description of the wind tunnel systems and layout are provided in Chapter 3. The aim of collecting both acoustic and vorticity data with only the cavity inserted into the floor of the tunnel was to identify the resonant tone(s) of the cavity and capture images of the shear layer in the Baseline configuration.

In preparing to complete the final phase of testing, rod supports with one of the three different diameter rods were added to removable floor plate and positioned the cylindrical rod into the crossflow, centered at a pre-determined height directly over the leading edge of the cavity. This configuration was chosen for research because it is one of several methods known to suppress acoustic resonance tones in a variety of cavity flow applications. With this “Cavity + Rod” configuration in place both the level of acoustic suppression available from each of the rods, and the effect of the wake from the rods on the cavity shear layer were measured and assessed.

# CHAPTER 2

# TECHNICAL REVIEW AND ANALYSIS

## Cavity Flow Review

As noted earlier, concentrated efforts investigating the physical phenomenon associated with cavity flow began in the early 1950's, and research results obtained by Krishnamurty [3] and Roshko [4] in 1955 continue to be cited as foundational to the study of cavity flows. Working together at times, the two investigators reported related findings each from a different perspective. Krishnamurty examined the acoustic radiation from shallow wall gaps of varying length and found that the cavities emitted strong acoustic tones, as high as 160 dB. Roshko, who was initially interested in the drag resulting from the presence of a cavity, conducted experiments with a model of varying depth and concluded that the pressure on the cavity walls accounted for almost all of the increased drag. Both men noted the presence of vortex motion within the cavity, but it was Roshko who noted that "*the formation of the vortex occurs by the deflection of part of the separated boundary layer into the cavity, this deflection occurring at the downstream edge and creating a relatively high pressure on the cavity wall in that vicinity*." It was from this point that the scientific study of cavity flow began to develop.

In 1962, Plumblee, Gibson, and Lassiter [5] reported their cavity flow investigations and presented a theory for the prediction of resonant frequencies and pressure amplifications of a rectangular cavity in a flow field. Despite the detailed analysis of the prediction technique, Shaw and Mcgrath [6] noted that because it was an iterative approach that did not readily converge, the method received little attention, mainly due to the difficulty in use of it. They do however, in the same paper, highlight that one of the most referenced historical works in the study of flow induced cavity acoustics is that of J. E. Rossiter [1].

The primary conclusion of Rossiter's research [1] was that the unsteady pressures acting in and around a rectangular cavity in subsonic and transonic flow may predominantly contain random components for shallow cavities (L/D > 4), while a deep cavity (L/D < 4) will predominantly contain periodic components. In addition to his conclusions, Rossiter found that the frequencies he had measured in the Mach number range, 0.4 < M < 1.2, could be represented by empirical Equation (1):

$$f = \frac{U_\infty}{L} \frac{(m-n)}{\left(\frac{1}{K_v} + M\right)} \quad (1)$$

where $f$ is the frequency that arises based upon the cavity length $L$, freestream velocity $U_\infty$, Mach number $M$, and $K_v$ the ratio of convective velocity of the vortices to freestream velocity. It should be noted that $U_\infty/L$ can be considered as a reference or characteristic frequency, or alternately, $L/U_\infty$ can be thought of as a characteristic time period for the cavity flow. The mode is represented by $m$, and refers to the sequence of frequencies, while $n$ is a factor that Rossiter assigned to different length to depth ratio cavities to account for the delay between acoustic wave generation at the trailing edge and vortex creation at the leading edge. For an L/D = 4 cavity, Rossiter [1] derived values for the convective velocity ratio and phase delay factor of, $K_v$= 0.57 and n = 0.25, respectively.

Heller, Holmes, and Covert [7] improved upon Rossiter's formula for broader Mach number ranges by assuming that the cavity sound speed is equal to the free-stream stagnation sound speed (i.e. cavity recovery factor closer to 1), rather than the free-stream speed of sound (i.e. cavity recovery factor equal to 0). The modified Rossiter Equation (2), adds the effect of the ratio of specific heats, $\gamma$, and is denoted by $S_1^*$ when the resonant frequencies are normalized with the freestream flow speed, $U_\infty$, or by $S_2^*$ when the resonant frequencies are normalized with the stagnation sound speed, $c_o$.

$$S_1^* = \frac{fL}{U_\infty} = (m-n) \Big/ \left\{ \frac{M}{[1+(\gamma-1)M^2/2]^{1/2}} + \frac{1}{K_v} \right\} \quad (2)$$

Heller, Holmes, and Covert [7] showed good agreement between this equation and experimental data collected over a Mach number range, 0.2 to 3.2.

By 1973, Covert joined forces with Bilanin [8] and introduced a mathematical model to estimate the excitation frequencies from shallow cavities. In their two-dimensional model, the mixing (shear) layer was approximated by a vortex sheet that separated the inviscid convective flow above from the quiescent inviscid fluid within the cavity. They noted that the unsteady behavior of the vortex sheet impacting the trailing edge of the cavity results in pressure fluctuations from the apparent mass flux into and out of the cavity, leading to the excitation of the mixing layer at the leading edge. They modelled this feature of the flow by a single periodic acoustic monopole located directly at the trailing edge of the cavity. Comparison of Bilanin and Covert's mathematical results with experimental data collected earlier by Heller, et al [7] suggested that their model was able to offer reasonable approximations for cavity excitation frequencies.

In 1975, Heller, together with Bliss [2], continued the work started earlier and presented a more detailed description of the physical mechanisms understood to be involved in flow-induced cavity oscillations. They stated that the oscillation process results from "*interaction of the free shear layer and the cavity internal medium, which involves both acoustic and hydrodynamic mechanisms*". Their six step process introduced the "pseudo-piston" effect to describe how, for a shallow cavity, mass addition and removal at the rear bulkhead produced forward travelling waves that would reflect from the front bulkhead to become rearward travelling waves, all the time forcing the shear layer in an unsteady manner. They also suggested a feedback loop where the shear layer motion just described, was in turn responsible for the mass addition and removal near the trailing edge, thus creating a sort of self sustaining cyclical process.

Despite these developments of cavity flow theory, Tam and Block [9] believed that earlier models had failed to consider, or even misrepresented, some of the influencing factors necessary to gain a more complete understanding of the physical mechanisms of acoustic wave generation. The following, which they note differs significantly from Bilanin & Covert's [8] mass addition and removal model, is Tam & Block's proposal for the acoustic wave generation process:

> "*During the upward motion of the cycle the fluid of the shear layer shields the trailing edge of the cavity from the external flow … and no pressure waves of any significance are generated. When the shear layer is deflecting downward there is an inflow of external fluid into the cavity*" and "*a high-pressure region forms momentarily near the trailing edge of the cavity. The transient nature of the flow causes the emission of a compression wave. The compression wave propagates in all directions*" and will "*be modified by the convection effect of the mean flow as it radiates away from the trailing edge of the cavity*." [9]

Based on the above hypothesis, Tam & Block's contribution to the analysis of cavity flow characteristics was the development of a mathematical model designed to predict the frequencies that will oscillate from a rectangular cavity under given flow conditions. Like Rossiter's model, their work incorporates the non-dimensional parameters of Strouhal and Mach numbers, but it also emphasizes the importance of the momentum thickness to length ratio, $\theta/L$, as well as the length to depth ratio, $L/D$, both of which are parameters related to the stability characteristics of the shear layer.

There are two particular features of this model that Tam and Block believe help to more accurately represent the visual observations reported by Krishnamurty [3] and Heller & Bliss [2]. First, as illustrated in Figure 1, they utilized a periodic line source at the trailing edge to simulate emission of the compression wave, EE′E″, from the trailing edge as it propagates above and below the shear layer, and two other periodic line image sources ahead of and below the cavity, A and B respectively, to reproduce the reflected acoustic waves within the cavity, A′A″ and B′B″. The second feature, which they note completes the model, is inclusion of the effects that the acoustic wave field travelling both inside and outside the cavity has on the instabilities present within the shear layer.

Although the application of Tam and Block's mathematical model was outside the scope of this study, their results are shown in Figure 2 (their Figure 19 [9]), which predict

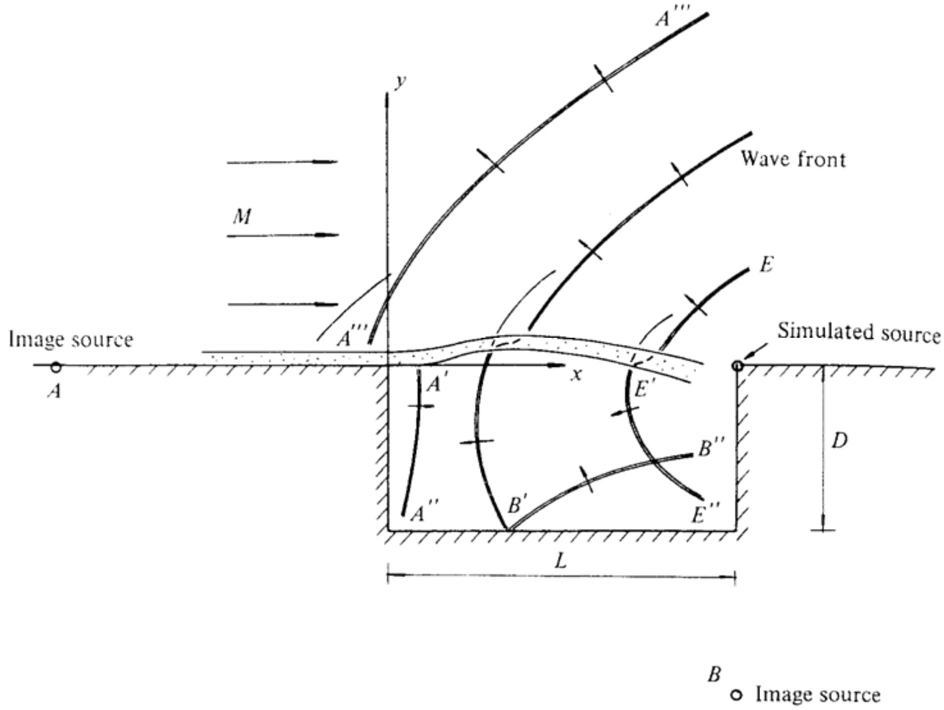


**Figure 1: Theoretical Model as proposed by Tam & Block [9]**

discrete tone frequencies as a function of Mach number, and are compared to Rossiter's [1] data. Figure 2 contains data that will be compared to the results of this current study.

There are two other elements related to the review of relevant cavity flow information that are valuable to mention but will not be discussed in detail in this thesis, rather, the reader is referred to an earlier thesis on this subject by Christian Gauthier [10]. In his work he provided a summary of the three categories of cavity flow, Open, Transition, and Closed, according to an increasing length to depth ratio, L/D, as well as a review of the classification of the different behaviors encountered, namely, Fluid-Dynamic, Fluid-Resonant, and Fluid-Elastic. This thesis will focus on open cavity flows, where the shear layer spans the cavity, and Fluid-Dynamic interactions, where shear layer instabilities characteristics and feedback mechanisms will create peak resonant tones within the cavity.

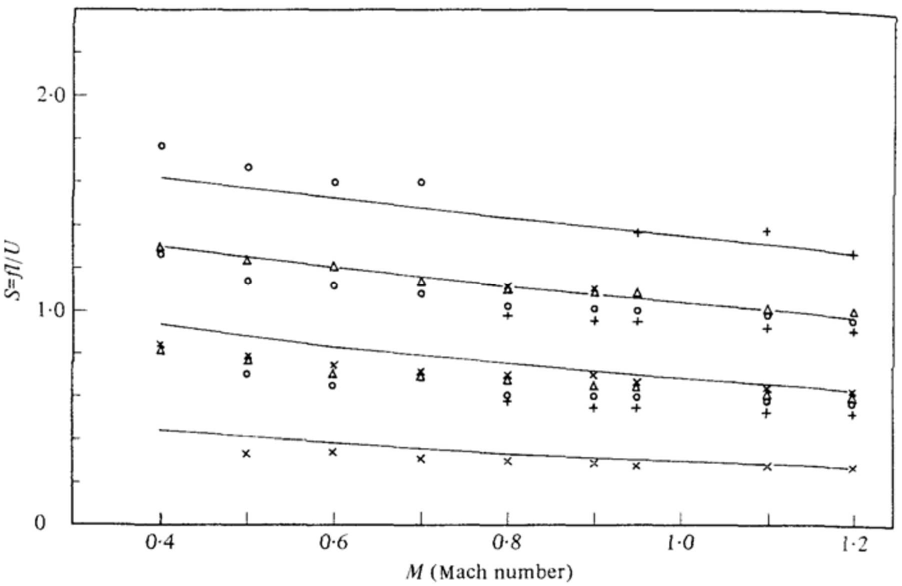


**Figure 2: Comparison of Tam & Block's theoretical results to Rossiter's (1964) experimental data.** (their Figure 19), x, L/D = 4; △, L/D = 6; o, L/D = 8; +, L/D = 10. ——— , their Equations (21) and (19) **[9].**

## Shear Layer Analysis, Stability, and Forcing

Because both wall and free shear layers are integral components of the development of cavity flow oscillations, it is worth reviewing the basics concerning their origin, distinguishing features, stability characteristics, and also the relationship between free and cavity shear layers.

In referring to the free shear layer shown in Figure 3, Ho and Huerre [11] describe the conceptual framework of stability theory applied to two laminar streams of the same fluid with velocity $U_1$ and $U_2$ ($U_1 > U_2$), which are assumed to give rise, by viscous diffusion, to a weakly diverging *steady* basic flow *U(y;x)*. They also note that the momentum thickness, $\theta(x)$, initially increases as the square root of *x*. They go on to describe that shear layer flow can be characterized by two non-dimensional parameters, namely the velocity ratio, $R = \Delta U / (2\bar{U})$, and the Reynolds number, $\mathrm{Re}_o = \bar{U}\theta_o / \nu$. The

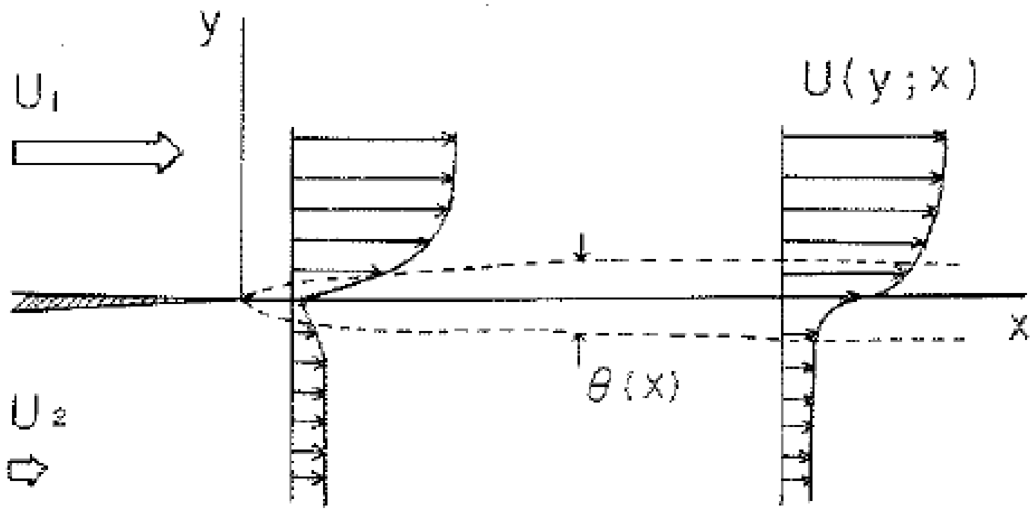


**Figure 3: Sketch of spatially developing mixing layer (from Ho & Huerre [11]).**

velocity ratio measures the relative magnitude of the total shear, $\Delta U = U_1 - U_2$, as compared to the average velocity $\bar{U} = (U_1 + U_2)/2$, while the Reynolds number, based on initial momentum thickness, $\theta_o$, and kinematic viscosity, ν, accounts for viscous effects.

White [12] has provided valuable discussion of shear layer stability when describing linear stability theory as it applies to parallel viscous flows. Following a derivation of the linearized Orr-Sommerfeld equation (Eqn 5-18 [12]), White outlines five important stability theorems all related to the velocity profile, *U(y)*, within an inviscid flow field. The meanings of two of those five theorems are depicted in the four velocity profiles of Figure 4 (a) thru (d), and they state:

> **Theorem 1** [Rayleigh (1880)] – It is necessary for instability that the velocity profile have a point of inflection.

> **Theorem 3** [Fjørtoft (1950)] – If a point of inflection exists, it is further necessary that $U''(U - U_{PI}) < 0$ somewhere on the profile, where $U_{PI}$ is the velocity at the point of inflection.

White identifies flow fields with velocity profiles that resemble Figure 4(d), which are unstable even in the inviscid limit described by the theorems, as: a) boundary layers with adverse pressure gradients; b) the shear layer between parallel streams; and c) as jet and wake flows.

White [12] discusses the nature of the eigenvalues of the dimensionless, fourth-order, linear, homogeneous Orr-Sommerfeld ordinary differential equation (White's Eqn 5-23 [12]) that provide some insight into the flow stability tendencies based on its *U(y)* velocity profile. Specifically, he highlights that a solution will be unstable if eigenvalues for temporal instability, $C_i^* > 0$ and/or spatial instability, $\alpha_i^* < 0$, are found. White also describes the analysis of Betchov and Szewczyk [13], where it was determined that a two-dimensional parallel flow shear layer of the form, $U = U_o \tanh(y/L)$, possessed temporal and spatial instability eigenvalues on the Orr-Sommerfeld thumb curves of $C_{i,max} = 0.19$ and $\alpha L = 0.5$, making it unconditionally unstable for all Reynolds numbers.

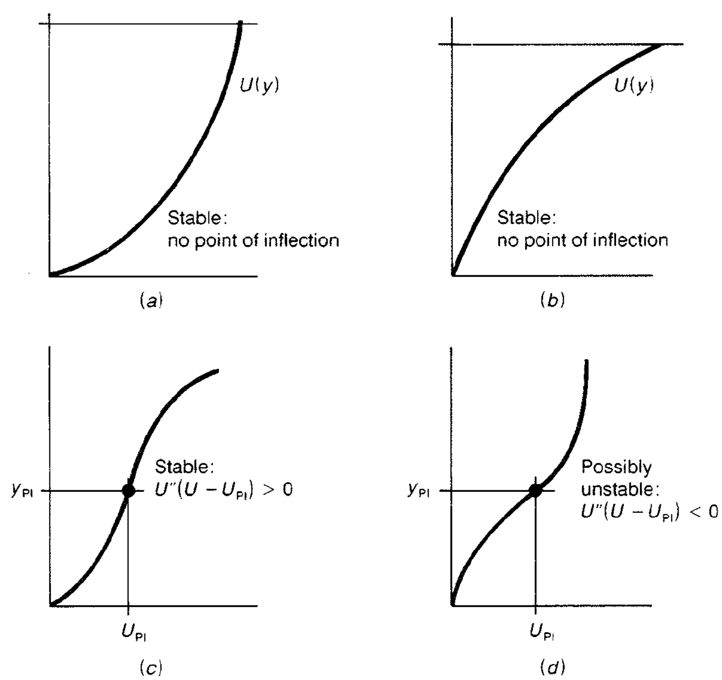


**Figure 4: Velocity profiles evaluated for stability by Theorems 1 & 3 (from White [12]).**

The discussion of shear layers and stability theory are harmonized in the comments by Ho and Huerre [11], who state that the basic vorticity distribution of a (mixing) shear layer is inviscidly unstable to small perturbations via the Kelvin-Helmholtz (K-H) instability mechanism. The result being that two-dimensional waves begin to grow exponentially with downstream distance from a disturbance as they roll up into vortices, and continue to grow as neighboring vortices merge into pairings that stack up, one above the other, normal to the mean flow direction. Ho and Huerre [11] show by way of the numerical and experimental results and data in Figure 5 the variation of spatial and temporal instabilities of the shear layer as a function of a momentum-thickness based Strouhal number, $St = \frac{f\theta}{\bar{U}}$. The data in Figure 5 are the spatial growth rate, $\frac{-\alpha_i \theta}{R}$, and phase velocity, $\frac{C_r - \bar{U}}{\bar{U}R^2}$, normalized by the shear layer momentum thickness θ, velocity ratio R, and average velocity $\bar{U}$. The Strouhal number, $St_n = 0.032$, represents the most amplified wave, corresponding to the natural frequency, $f_n$, of the shear layer and only changes by 5% for the velocity ratio represented by: '–––' *for R* << 1, and '——' *for* *R* = 1 .

It is of significance to note that Strouhal number based on momentum thickness of the shear layer plays the key role in the growth of instabilities. As such, configurational changes, which significantly influence the shear layer profile and hence its momentum thickness, play fundamentally complex roles in their stability behaviour, more so than a simplistic frequency effect if present. Higher frequencies in a shear layer flow can change available energy in various regimes for instability growth and amplifications of cavity flow development.

However, Ho and Huerre [11] point out that in most cases a shear layer flow is influenced by some specific forcing frequency, $f_f$. The charts provided in Figure 6 and Figure 7 illustrate the effect that forcing a shear layer at or below its natural frequency, $f_n$, will have on the development of K-H instabilities downstream of the initial disturbance. In

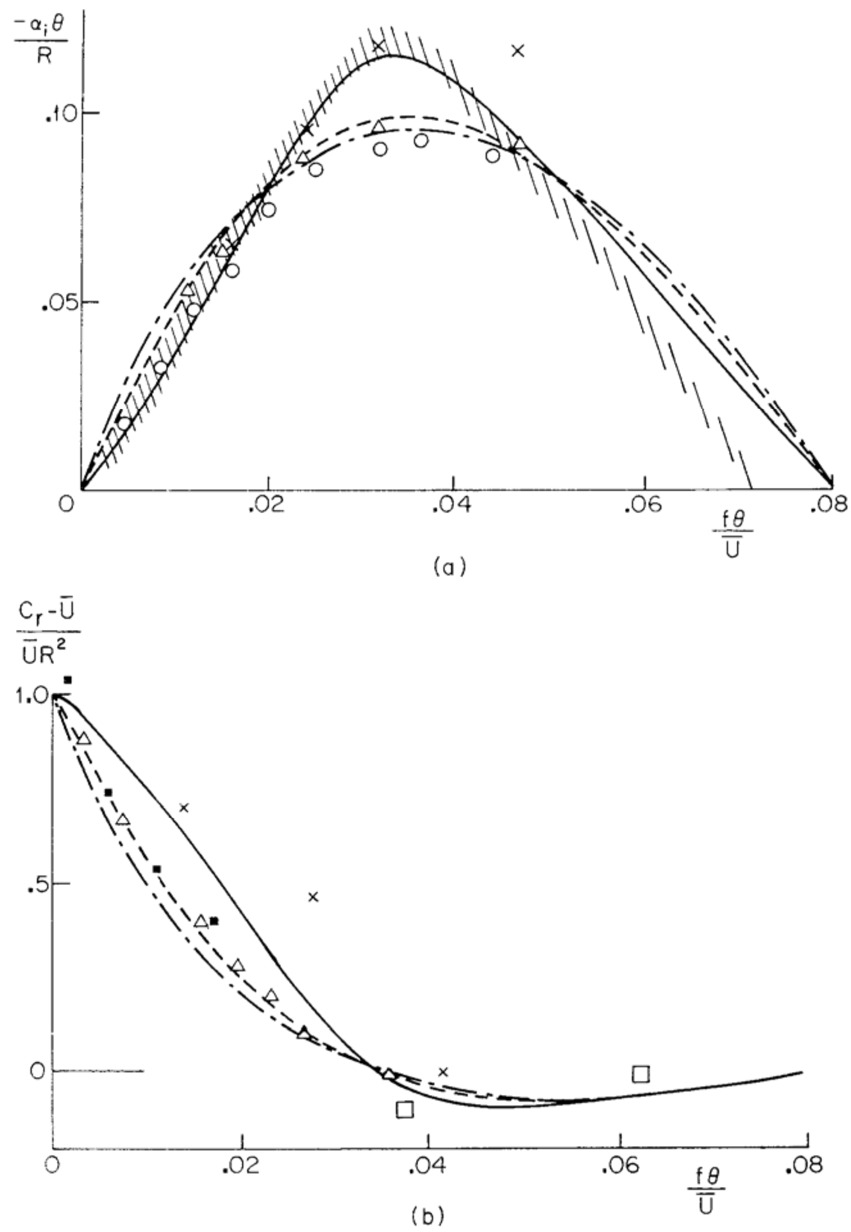


**Figure 5: Shear layer variations of (a) spatial growth rate and (b) phase velocity with Strouhal number. Numerical data respresented by lines, and experimental data represented by markers. (from Ho & Huerre[11])**

each figure the shear layer velocity ratio is R = 0.31, and the evolution of spectral components are shown in 6(a) and 7(a) along with the response frequency, $f_r$, depicted by '+', while the growth of the shear layer momentum thickness, θ, downstream of the disturbance is depicted in 6(b) by '•' and in 7(b) by '△'.

The interpretation of the numerical and experimental results contained within Figures 6 and 7 is best described by the following excerpt from Ho and Huerre.

> *"The initial vortex-formation frequency $f_r$ is seen to correspond to that particular harmonic of the forcing frequency $f_f$ that is nearest to but smaller than $f_n$. In the range* $(1/2)\,f_n < f_f \lesssim 2\,f_n$, *$f_r$ is found to be equal to $f_f$, and vortices form at the forcing frequency. The downstream evolution of the corresponding spectral components is shown in* Figure 6. *The higher initial level of fundamental $f_f$ temporarily suppresses the growth of the subharmonic $f_f$ /2, and vortex pairing is delayed. When* $(1/3)\,f_n < f_f < (1/2)\,f_n$, *the response frequency $f_r$ jumps to the first harmonic $2f_f$ closest to the natural frequency $f_n$* (Figure 7). *In other words, the excitation becomes the first subharmonic of the initial vortex passage frequency $f_r$; neighboring vortices are laterally displaced and subsequently wrap around each other to form a single structure. In contrast with the previous case, vortex pairing is promoted*." Ho & Huerre [11]

One remaining aspect of free shear layers to be discussed is their relationship with cavity flows. By definition, free shear layers are unaffected by walls, White [12]. The question then arises; do all the factors previously discussed also apply to the shear layer that develops over a cavity? Despite the presence of walls that act as reflecting and impinging surfaces, there are sufficient similarities between the two to warrant the thoughtful application of free shear layer theories, models, and knowledge base to their cavity flow counterparts.

The preceding discussion of shear layer origins, features, stability characteristics, and forcing has only provided a brief introduction to a topic that has received a

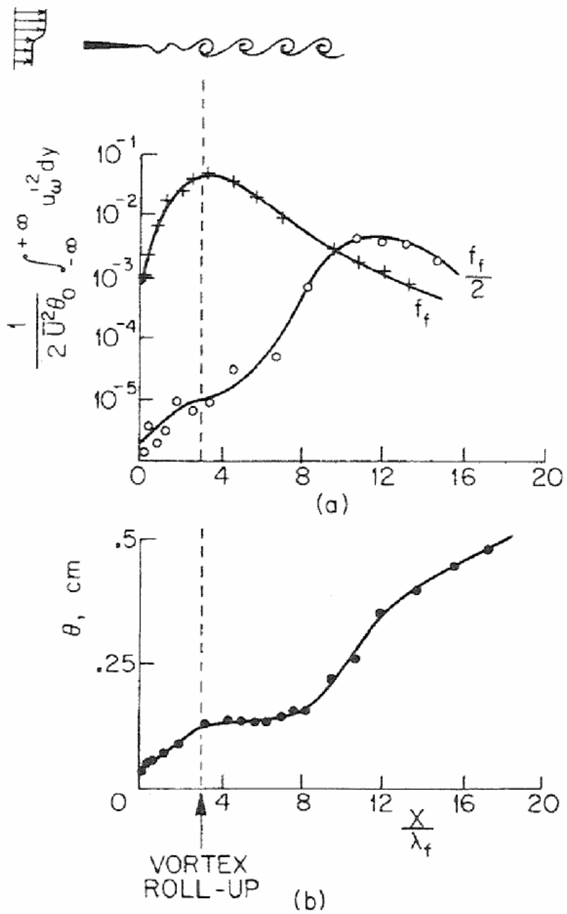


**Figure 6: Evolution of (a) spectral components and (b) momentum thickness with downstream distance for $f_n/2 < f_f \leq f_n$ and R = 0.31 (from Ho & Huang 1982).** $u'_\omega$ is the narrow-band velocity fluctuation centered at $\omega=2\pi f$; $\lambda_f = \lambda_r$. **[11]**

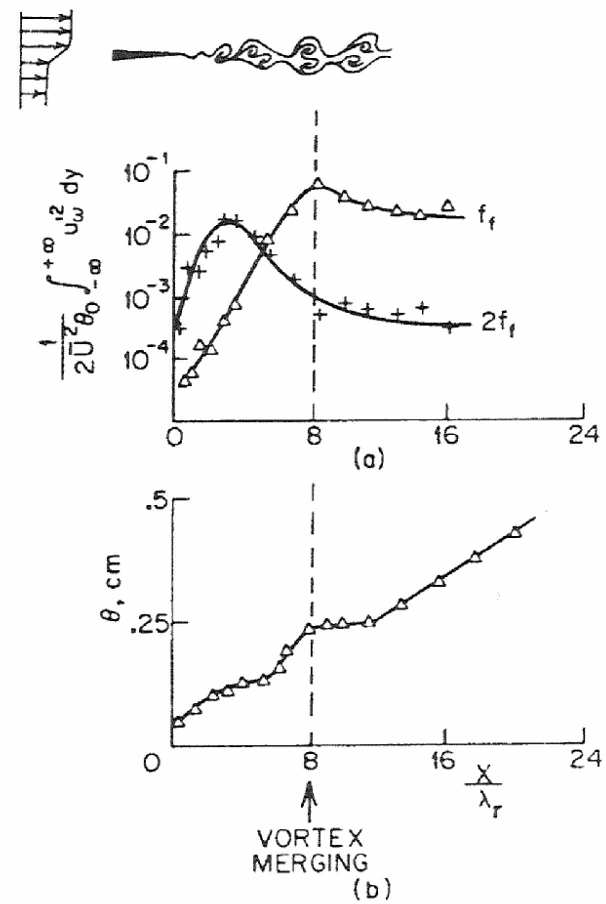


**Figure 7: Evolution of (a) spectral components and (b) momentum thickness versus downstream distance for $f_n/4 < f_f \leq f_n/2$ and R = 0.31 (from Ho & Huang 1982)** . $\lambda_f = 2\lambda_r$. **[11]**

considerable amount of theoretical, analytical, and experimental attention over the last several decades. It has however provided enough information to preface the following section and main interest of the current study, cavity resonance suppression.

## Acoustic Suppression of Cavity Resonant Tones

All of the time and research that has gone into trying to understand and describe the physical mechanisms of cavity flow shear layers has been motivated by the necessary task of minimizing the elevated sound pressure levels within a structural cavity that lead to fatigue and damage. Having gained some insight into the physical mechanisms involved in the oscillation process, Heller and Bliss [9] recorded acoustic noise suppression levels of approximately 20 decibels, and concluded the latter part of their paper with the topic of suppression techniques by stating:

> *"Oscillation amplitudes can be reduced by the stabilization of the shear layer, by the prevention of the periodic trailing-edge mass addition process, or by a combination of both. Shear layer stabilization is achieved either through the introduction of vorticity into the shear layer by upstream vortex-generators or spoilers, or by the provision of an inherently stabilizing trailing-edge geometry (a slanted trailing edge)."*

Their positive results seemingly paved the way for future cavity noise suppression research, as it was from that point forward that a vast majority of papers began to explore various techniques aimed at controlling cavity noise levels. Experimental results from Vakili and Gauthier [14], following their research of upstream mass injection to control cavity flow, reported a 27 dB reduction in the cavity oscillation amplitude not only support the above hypothesis, but are indicative of the success that has been achieved.

Before discussing acoustic suppression further, familiarity with the logarithmic decibel Sound Pressure Level (dB SPL) scale reveals that a reduction of 20 decibels provides a substantial reduction in the pressure forces acting upon the structure and

**Table 1: Conversion of dB SPL to Metric and English rms pressure values.**

| dB SPL | Pressure rms (N/m$^2$) | Pressure rms (lbf/in$^2$) |
|---|---|---|
| 100 | 2.0 | 0.000290 |
| 125 | 35.6 | 0.00516 |
| 150 | 632 | 0.0917 |
| 160 | 2000 | 0.290 |
| 175 | 11250 | 1.63 |

contents of a cavity. The metric unit conversion between dB SPL and the root mean square (rms) value for pressure, $p_{rms}$, is given by Equation (4), while Table 1 provides both the corresponding Metric and English unit values.

$$dB\ SPL = 20\log_{10}\left[\frac{p_{rms}\left(N/m^2\right)}{2\times10^{-5}\left(N/m^2\right)}\right] \quad (4)$$

Since the mid 1970's, numerous cavity noise suppression techniques and devices have been investigated. The field of study has developed to the point where techniques aimed at suppressing cavity oscillations have been classified by Cattafesta III, Williams, Rowley, and Farrukh [15] as either "passive" or "active" control approaches, which (they remark) is consistent with terminology used in active noise and vibration control. They highlight the distinction that active control provides external energy to the flow or takes it out of the flow, while passive control techniques do not. By this definition, any forced oscillation of a flap, pumping of a jet, or powered resonance tubes would fall into the active control classification. While a stationary fence, cylindrical rod, or sloped trailing edge would be considered passive control techniques. Active or passive, it is control of the sound pressure levels created by the flow-induced cavity oscillations that is important.

## High Frequency Suppression Techniques

One method that has proven to be an effective means of suppressing cavity oscillations, and has received increasing attention over the last decade, is high frequency forcing of the shear layer. The high frequency approach aims to stabilize the shear layer by forcing it at a frequency above which the instabilities in the shear layer can be amplified (refer back to Figure 5(a)). Wiltse and Glezer [16] provided some insights into the high frequency manipulation of cavity flow shear layers when they reported on their investigation of the mixing process in free shear layer flows. After conducting tests where a pair of piezoelectric actuators was used to introduce a high-frequency waveform with amplitude modulated low-frequency sidebands to the free shear layer at the base of the exit plane of a square air jet, they concluded that "*direct small scale excitation results in enhanced energy transfer from the large to the small scales and in a substantial increase in the dissipation and in the decay rate of turbulent kinetic energy*."

Working with the data collected by Wiltse and Glezer [16], Stanek, along with his fellow collaborators,[17,18] conducted further research and presented their own model describing how they believed high frequency forcing affected the cavity shear layer. In referring to Wiltse and Glezer's conclusion, Stanek, et al [17] submit that *"it is more physically consistent to describe the effect of high frequency flow control as shear layer stabilization"*, meeting the objective previously highlighted by Heller and Bliss. Further examination of experimental data and reference to classical turbulence theory led to the following description of the "Stanek" model. It states:

> *"the cause of the suppression of large-scale structures after high frequency forcing is an alteration of the mean turbulent flow. The alteration modifies the inviscid stability properties of the mean flow in such a way as to stabilize the mean shear flow and prevent the growth of large-scale instabilities in the first place."*[18]

Following publication of the Stanek high frequency acoustic suppression model described above, Stanek together with Ross, Odedra, and Peto[19] presented data collected from a series of large, 1/10$^{th}$ scale, experiments investigating the use of a cylindrical rod in crossflow as a high frequency suppression device. Their experimental results provide evidence of the effectiveness of rod in crossflow as an acoustic suppression device, “roughly 10dB difference” in the reported subsonic flow (Mach 0.85), and “about a 16 dB difference in the suppression of Rossiter tones” in the supersonic flow (Mach 1.19). Their results also offered several guidelines to follow when designing rod actuators for cavity flows. Those guidelines will be referenced again later in the experimental setup describe in Chapter 3. Another concluding remark by Stanek, et al [19], indicates that the rise in high frequency broadband acoustic levels is consistent with intense accelerated mixing near the cavity leading edge, which in turn is consistent with enhanced diffusion of momentum, leading to modification of the mean velocity profiles.

One of the most recent contributions on the topic of high frequency suppression of cavity oscillations is offered by Panickar and Raman [20], the latter of whom had partnered with Stanek on an earlier work [18]. In an effort to more clearly understand the physics of the high frequency technique, they aimed to investigate whether the acoustic suppression brought about by high frequency excitation was in fact the result of shear layer stabilization, and if so what mechanism led to the stabilization. After testing their “shedding+wake” rod in crossflow configuration, Panickar and Raman [20] reported that not only were the peak amplitudes of the Rossiter modes dramatically reduced, but linear stability calculations of the measured velocity profiles revealed that the spatial growth rates of shear layer instabilities also saw significant reductions in comparison to the baseline. Similar to the spatial growth rate versus Strouhal number figure introduced in the shear layer discussion earlier, Figure 8 presents a comparison of the amplification envelopes obtained from linear stability calculations of the mean velocity profiles for both the baseline “——”, and the shedding+wake “–··–” configurations taken at two downstream locations, X/D = 0.1 and 1.0.

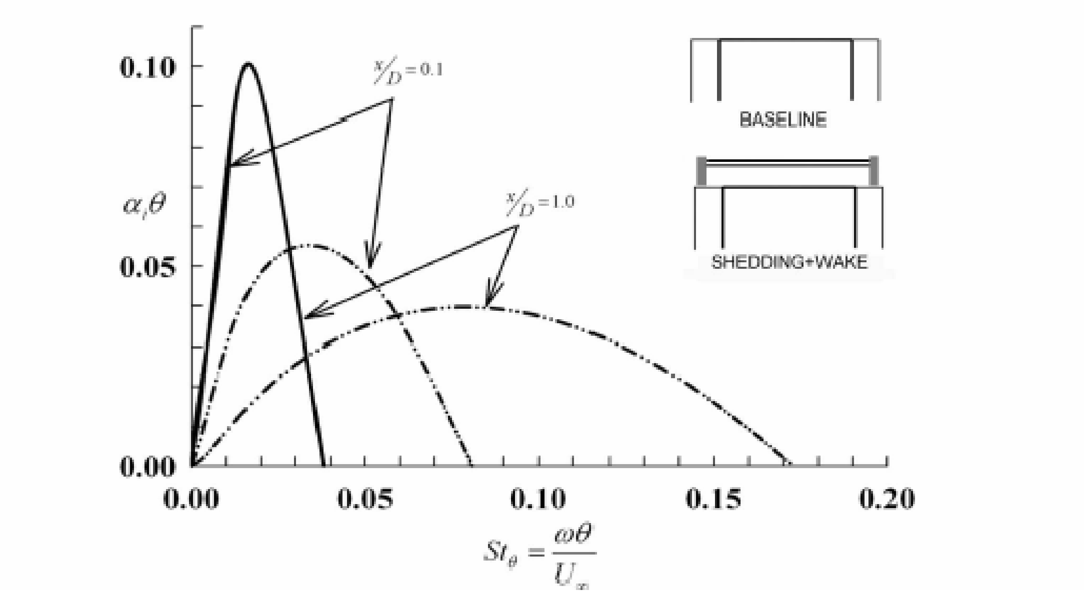


**Figure 8: Comparison of shear layer spatial growth with and without high frequency forcing (from Panickar & Raman [20]).**

Pleased with the results presented in Figure 8, but not yet convinced that it was the high frequency forcing component that resulted in the acoustic suppression, Panickar and Raman[21] conducted follow-on research with a slightly modified rod in crossflow. This second configuration, which they refer to as "non-shedding+wake", added a helical wire wrap to the rod so as to eliminate the high frequency vortex shedding while maintaining a wake like velocity profile. Analysis of the experimental and analytical results from this additional testing led Panickar and Raman to conclude that the "*mechanism for resonance suppression is the rapid spatial decay of all structures; such an effect is only brought about due to high frequency excitation in the cylinder-in-crossflow configuration.*"

With these most recent results from Panickar and Raman [20,21] the current understanding of the high frequency acoustic suppression technique waits for further research to expand and clarify our knowledge. Their results and analysis support the model submitted by Stanek [18] proposing that high frequency forcing modifies the inviscid stability properties of the mean flow resulting in a stabilized shear layer flow and prevention of the growth of large-scale instabilities.

Although the extensive body of literature on cavity flow related work has not been discussed herein, the background, historical, theoretical, and experimental review presented above is certainly sufficient to preface the current study presented in this thesis.

# CHAPTER 3

# EXPERIMENTAL METHODS AND PROCEDURES

This chapter will begin with an overview of the Particle Image Velocimetry (PIV) technique, and then expand upon the general approach of the experiments that was provided in the introduction. A complete description of the High Speed Wind Tunnel (HSWT) installation located at the University of Tennessee Space Institute (UTSI) will be given, including components of the air supply system, nozzle, test section, seeding system, and test model configurations utilized for this study. This will be followed by a review of the instrumentation systems used to control tunnel operation and to collect and analyze all data gathered over the course of testing. Next, the approach taken to select the dimensions and location of the rod(s) in crossflow for acoustic suppression will be reviewed. Following a detailed description of the test procedure that was followed through each of the four phases of testing, the chapter will close with a discussion of two of the factors known to have affected the experimental test results.

## Particle Image Velocimetry Technique

Laser PIV offers a relatively non-intrusive means of imaging a flow field. It uses a double pulse laser to illuminate a region of the flow that has been “seeded” with particles, and a camera to capture instantaneous images of the particles in the flow field. In the case of this study an atomized solution of Isopropyl Alcohol (70% Isopropyl Alcohol and 30% Water) and Rhodamine 6G dye was used to seed the flow ahead of the throat of the nozzle. When excited by the Nd:YAG laser the dye in the liquid particles fluoresced, and the emission was captured as particle images on a CCD digital camera.

By operating the laser in the LASERPULSE system in the Frame Straddle exposure mode, the laser pulsed twice, separated by an elapsed time, $\Delta t$, and two successive images of the illuminated flow field were captured as illustrated in Figure 9.

Image A from the first pulse was captured in Frame 1, and Image B from the second pulse in Frame 2.

The INSIGHT$^{TM}$ software then took the “image pair”, and performed an analysis method called Cross-Correlation. This cross correlation between the two images determined the distances, $\Delta x$ and $\Delta y$, that each individual particle had traveled over the elapsed separation time, $\Delta t$, and computed the 2-D velocity of the flow field particles. As depicted in Figure 9 (b), cross correlation was performed by dividing each image up into small interrogation regions, or spots, determining the spatial resolution of the measurements. In using two-frame cross-correlation the initial pulse delay was adjusted to ensure that the first laser pulse occurred precisely towards the end of the first frame. It was also recommended that the selected spot size be at least four times larger than the maximum displacement of the seeding particles [22]. Further discussion of the PIV system setup and parameters specific to this investigation is provided in the HSWT Controls and Data Acquisition Systems section below the heading of Imaging Control System.

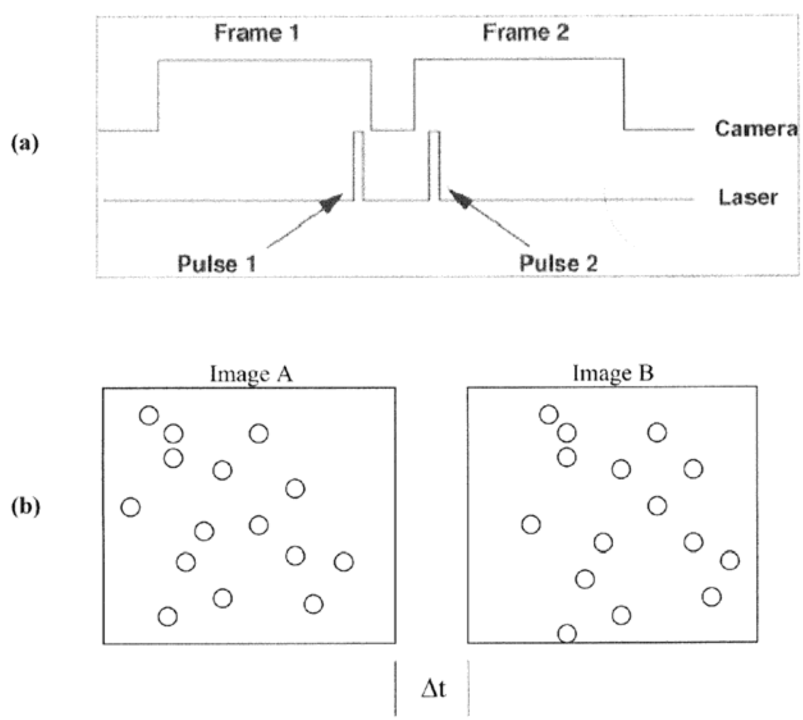


**Figure 9: (a) Frame Straddle mode; (b) Cross Correlation of particles within PIV image pairs.**

## HSWT Installations

The UTSI High Speed Wind Tunnel operates in a blow-down configuration and, along with the control and data acquisition instrumentation used throughout this study, is depicted in the sketch provided in Figure 10. Eighteen high pressure air cylinders, capable of being charged to a maximum of 3000 psi, serve as the reservoir of unconditioned compressed air that was routed to the tunnel via a computer controlled, pneumatically driven ValTek FlowServe valve. Downstream of the valve, the compressed air flows into a four section plenum that, through a combination of honeycomb grid and screens, homogenized the flow ahead of the nozzle. For reasons to be discussed later, this study was conducted using a converging-diverging nozzle designed for supersonic flow velocities of Mach 1.8. The nozzle was also designed to transition the circular cross-section flow over to a square cross-section flow ahead of the 8" x 8" test section. The test section measured four feet in length and had glass observation windows on each side and top, allowing for the use of a Schlieren or laser velocimetry system. Aft of the test section the flow was diffused and vented to atmospheric conditions.

As a means of seeding the flow for particle imaging using the laser Particle Image Velocimetry (PIV) technique, a 1/8" tube was inserted on the converging side of the nozzle approximately one foot ahead of the throat at the "six o-clock" position. This position allowed the Isopropyl Alcohol and Rhodamine solution to be atomized by the accelerating flow and disperse within the flow field prior to entering the test section. A small cylinder, pressurized by low pressure shop air was mounted to the outside of the tunnel in close proximity to the nozzle and served as the seeding solution reservoir. A pressure regulator and manually operated valve were used to control the flow of seeding particles ahead of the nozzle throat.

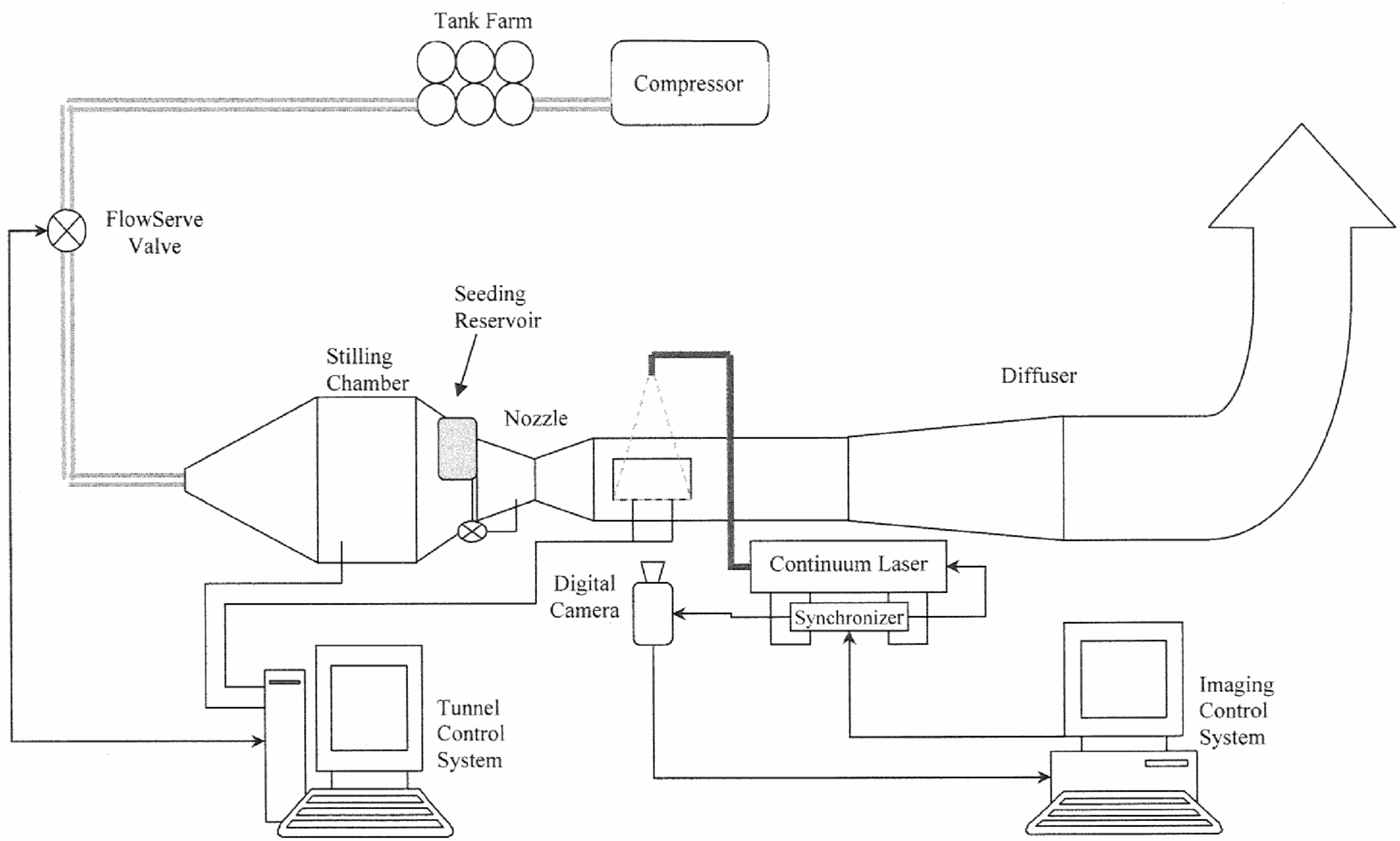


**Figure 10: Sketch of HSWT layout and associated test apparatus.**

## Test Configurations

The four phases introduced earlier were each associated with one of the four test section configurations required to complete the experimental testing for this investigation. A sketch of the test section and floor plate is provided in Figure 11, while complete technical drawings are contained in Appendix 1.

The four configurations under test were:

1) **Clean** – referring to no rod or cavity in the test section. Rod Support and Cavity Filler blocks were mounted onto the removable floor plate, and the whole assembly flush mounted with the floor of test section.

2) **Rod Signature** – With the Cavity Filler block still in place, Rod Support mounts were added to the ends of the Rod Support block depicted in Figure 11, and fastened to the removable floor plate. The supports were designed to position the centerline of the rod at a pre-selected height directly above where the leading edge of the cavity would later be. Three rod diameters were tested; 1/8", 3/16", and 1/4".

3) **Baseline** – created by removing the Cavity Filler block from the clean tunnel configuration described above. This resulted in a cavity in the floor of the test section with a Length, L = 3.5 inches, Depth, D = 1 inch, and Width, W = 2 inches, giving L/D = 3.5 and W/D = 2.0.

4) **Cavity+Rod** – the final configuration was obtained by removing the Cavity Filler block from the Rod Signature configuration. This left a rod in crossflow centered directly over the leading edge of the cavity.

Given the cavity dimensions noted in the Baseline configuration, and a anticipated average flow Mach number, M = 0.55, Table 2 highlights the resonant acoustic tones predicted by the Modified Rossiter equation described by Equation (2) in Chapter 2. These values were predicted using the convective velocity constant, $K_v$= 0.57, and length to depth delay factor, n = 0.25.

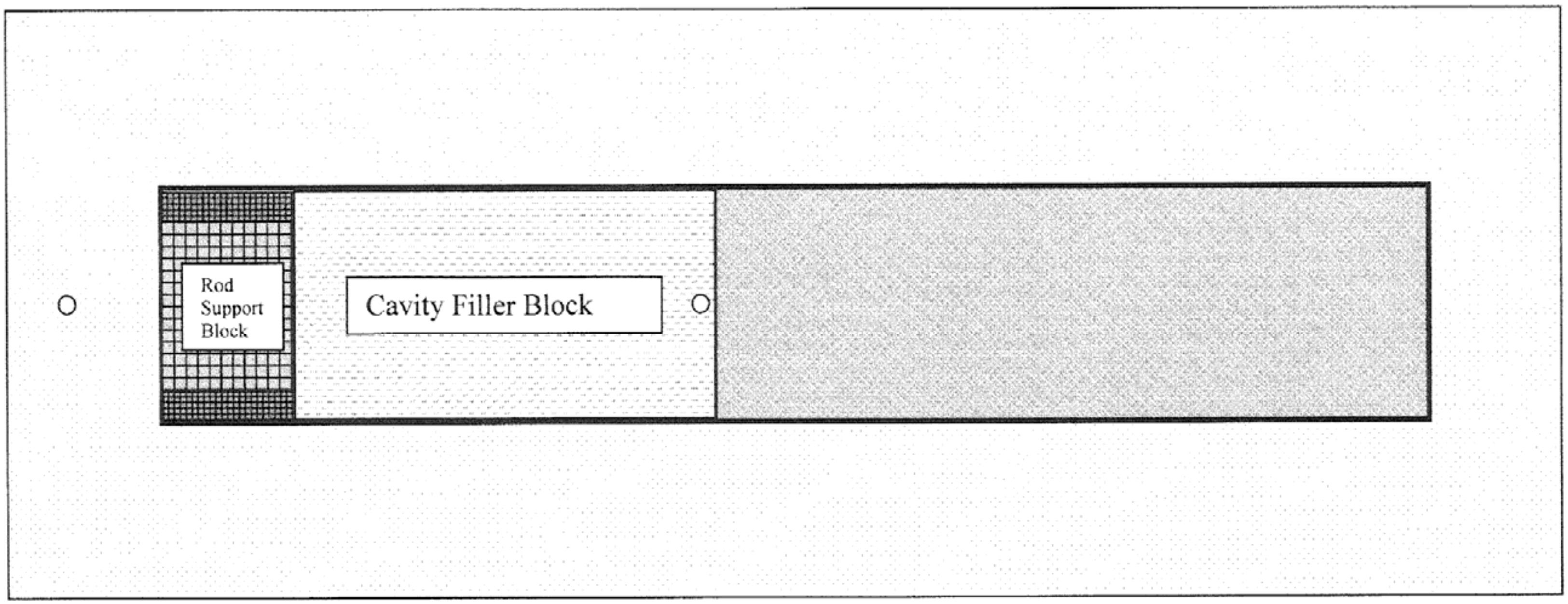


**Figure 11: Sketch of removable floor plate with filler blocks.**

**Table 2: Predicted Rossiter tones for L/D = 3.5 cavity and M = 0.55.**

| Rossiter Mode | Resonant Frequency |
|---|---|
| 1 | 690 Hz |
| 2 | 1610 Hz |
| 3 | 2530 Hz |
| 4 | 3450 Hz |

## HSWT Controls and Data Acquisition Systems

This investigation required the employment of several different instrumentation systems to facilitate both the operation of the wind tunnel as well as the collection of data from a variety of sources.

Tunnel Control System

The Tunnel Control System computer previously depicted in Figure 9 was used to monitor and control the HSWT flow conditions. This was accomplished through the use of National Instruments LabVIEW software and a customized Virtual Instrument (VI) designed, maintained, and operated by UTSI's Gas Dynamics Lab technician. Each of the flow parameters integral to the effective operation of the tunnel, including mass flow rate, total and static pressure, and static temperature, were interfaced to the Tunnel Control System via a National Instruments SCXI, 16 Channel Signal Conditioner, and sampled at a rate of 16 Hertz.

The tunnel operator indirectly controlled the flow Mach number by establishing a mass flow rate "set point" within the LabVIEW VI. This setpoint became the input to the ValTek FlowServe Logix 2000 controller, which in turn delivered a positioning signal to the FlowServe main control valve between the tank farm and the stilling chamber of the tunnel. The ValTek FlowServe valve is a pneumatically driven, computer controlled, positioning system that was designed to automatically adjust the mass flow rate of air measured on the downstream side of the valve to match the set point requested by the tunnel operator.

Downstream of the main control valve total pressure of the flow was measured by a pitot tube positioned inside the stilling chamber, while static pressure was obtained from a pressure port located just ahead of the leading edge of the cavity. Another static pressure port was located inside the stilling chamber for comparison to total pressure. A K-Type thermocouple also located inside the stilling chamber provided the static temperature necessary for application of the Ideal Gas Law and determination of fluid density. Together, these parameters were combined in a calculation of the freestream velocity, $\vec{V}$, and Mach number, M, of the flow entering the test section.

An Endevco, Model # 8507C-2, dynamic pressure transducer was centered on the floor at the rear of the cavity and was also interfaced to the Tunnel Control System computer. This sensor was used to detect pressure oscillations arising from shear layer interactions with the trailing edge of the cavity. The piezoresistive transducer with a dynamic range of 0 to 2 psig, full scale deflection of 300mV, and resonant frequency of 130 kHz, was sampled at a rate of two times the desired frequency spectrum band, e.g. 10KHz sample rate for a frequency spectrum of 0 - 5KHz, and 40KHz sample rate for frequency spectrum of 0 - 20KHz. A Fourier analysis module pre-programmed into the LabVIEW VI transformed the time domain pressure oscillations sensed by the dynamic transducer into a frequency domain spectrum suitable for plotting versus amplitude.

## Imaging Control System

Since one of the primary objectives of the research was to visually analyze cavity shear layer characteristics, a TSI LASERPULSE PIV System was used to capture instantaneous images of the seeded flow within the HSWT test section. The

LASERPULSE Synchronizer served as the link and timing control device ensuring synchronized operation between the Imaging Control System computer, Continuum Laser, and PIVCAM digital camera. A detailed summary of the LASERPULSE System components is provided in Table 3. The initial setup of the PIV system was accomplished through the INSIGHT™ software interface and involved both a Component and Process setup.

The first step required to prepare the PIV system was the Component setup. It included the selection and setting of specific camera and laser parameters. The PIVCAM 10-30 digital camera was set to operate with the following resolution and exposure settings: Pixels, x = 1000, y = 1016; Pixel Spacing, 9μm; Frame Rate, 30 Hz; Shutter Open Time, 255 μsec; and Shutter Open Delay Time, 0 msec . The Continuum SureLite Nd:YAG Laser delivered a single beam double pulse output with the following attributes: Wavelength, 532 nm (Green Light); Power, 200mJ/pulse; and Flashlamp Frequency, 10 Hz. The Q-Switch delay, which controls the power level of each Nd:YAG laser pulse, was set to 135μsec. From the start of a pulse sequence, initiated by the synchronizer trigger, the amount of pulse delay until the first pulse was 270 μsec, and the separation time, $\Delta t$, until the second pulse was 5μsec.

**Table 3: Detailed summary of TSI LASERPULSE Imaging System.**

| Component | Model # | Description |
|---|---|---|
| Continuum SureLite Nd:YAG Laser | Y200-C | Double Pulse, 532 nm Wavelength (Green Light), 200 mJ/Pulse |
| Articulating Laser Light Arm | 610015 | Delivers beam and laser light sheet to test section. |
| Synchronizer | 610032 | Master Timing Control Device |
| PIVCAM 10-30 | 630046 | CCD Camera with 28mm F/2.8 Nikkor Lens, capable of 30 frames/sec |
| INSIGHT™ PIV Software | Version 3.2 | PIV System setup, Image capture and analysis software |

The second step of preparing the PIV system was the Process setup. It entailed the selection of parameters defining how PIV images would be acquired and processed. The PIVCAM was selected as the image source and operated in the Frame Straddle exposure mode and the Sequence capture mode.

Physical memory of the Imaging Control System computer limited the number of images captured in each test run sequence to 14. Three other aspects of the Process setup were Grid Setup, Velocity Calibration, and Peak Search/Correlation Algorithms.

In order for the INSIGHT™ software to perform cross correlation of the image pairs as described earlier, the following factors were considered. It was anticipated that the maximum velocities of the subsonic flow field would be around 200 meters/sec. By using the PIVCAM to capture a still image of a scaled ruler, a velocity calibration measurement of 103.4 μm/pixel was obtained. The flow velocity and calibration measurement together with the elapsed time between laser pulses of five microseconds, indicated that the fastest particles would travel just under 10 pixels between laser pulses. To satisfy the recommendation of selecting a grid size four times larger than the maximum displacement, an interrogation spot size of 64 x 64 pixels was chosen, along with an equal spacing of 8 pixels between both the x and y columns. With these two selections, the distance between vector rows and columns was observed to be 0.827mm. The PIVCAM was operated with an aperture setting of F8.0.

With the u(x,t) and v(y,t) components of the velocity field known following the cross correlation process, Equation (5) was available within the Tecplot visualization software as a PIV macro and used to calculate vorticity, ω, throughout the flow field.

$$\omega = \frac{\left(\frac{\partial v}{\partial x}\right) - \left(\frac{\partial u}{\partial y}\right)}{2} \qquad (5)$$

The factor of 2 in the denominator is needed to account for the spatial geometry of the grid setup. To facilitate the comparison of experimental results, the practice in earlier cavity flow studies by Meganathan [23] and Radhakrishnan [24] was to normalize the local velocity, U, at points throughout the flow field by the freestream velocity, $U_\infty$, and to non-dimensionalize vorticity, ω, using the cavity depth, $D$, and the freestream velocity, $U_\infty$, through the relation, $\frac{\omega D}{U}$. This practice will be continued in this thesis, and non-dimensional velocity and vorticity contours will be presented in the results of Chapter 4.

## Determination of Rod Dimensions and Location

Recommendations on the sizing of a rod in crossflow, as well as where to position the rod with respect to the leading edge of the cavity are provided by Smith, Welterlen, Maines, Shaw, Stanek, and Grove [25], and Stanek, et al [19]. While the conclusion to Smith's work [25] indicated that effective suppression of the cavity flow oscillations could be realized with a rod diameter 30 to 40% of the upstream boundary layer thickness, δ, the report from Stanek [19] concluded that for optimal suppression of cavity tones, both the diameter of the rod and the centerline height of the rod above the leading edge of the cavity should be two-thirds of the boundary layer thickness, $\frac{2}{3}\delta$. Stanek also indicated that with the rod partially submerged in the boundary layer a "Modified" Strouhal number of 0.165 could be used to estimate the resulting shedding frequency of the rod in crossflow.

In the early stages of this current study, preliminary PIV imaging of the flow field ahead of the cavity at a flow Mach number around, M = 0.55, indicated that the boundary layer thickness was between 11 and 12 mm. Given the varied range of recommended diameters, 30 to 65% of δ, it was decided to test three rod diameters, ranging from 3 mm to 6.5 mm, more specifically 1/8", 3/16", and 1/4". The rods were all centered directly above the leading edge of the cavity at a height, h = 11.9 mm or 15/32". Applying

Stanek's "Modified" Strouhal number, St = 0.165, for the rod submerged within the boundary layer, it was estimated that shedding frequencies would range from 4900 Hz for the 1/4" rod out to 9700Hz for the 1/8" diameter rod.

## Test Procedures

Using the LabVIEW VI, the Tunnel Control System operator initiated the test by verifying sufficient pressure was available in the tank reservoir and remotely opened the FlowServe main control valve. The mass flow rate was steadily increased until it approached the setpoint for the desired flow Mach number, at which point the VI was set to "Auto". From the moment each test sequence was initiated, a data file of the Tunnel Control System parameters, including static and total pressures, temperature, Mach number, mass flow rate setpoint, and actual mass flow rate were recorded into an Excel data file spreadsheet. With the tunnel operating on condition, and the LabVIEW VI converting the dynamic transducer pressure oscillations to a frequency spectrum displayed on the computer monitor, the operator would select the VI button to collect a frequency spectrum sample. The tunnel operator then proceeded to open the seeding system valve, allowing seed particles to enter ahead of the nozzle and be atomized by the oncoming flow. This was the cue for the Imaging Control System operator to initiate the image capture process by making the selection in the INSIGHT™ software interface, causing the synchronizer to trigger the appropriate sequence for both the double pulse laser and digital PIV camera. Following the satisfactory collection of PIV images, the tunnel operator closed the seeding valve, collected a second sample of spectral data, switched the tunnel control to manual, reduced the mass flow rate back to zero, and ended the test sequence by remotely closing the main tunnel control valve. If sufficient tank pressure remained, the procedure was either initiated again and another sequence of images collected, or the model was changed out for the next phase of testing.

Following the collection of PIV images, INSIGHT™ software was used to carry out the cross-correlation and vector analysis of the selected area of interest in each of the images.  Following a simple validation of the original vector files to remove spurious vectors, a process that will be described in more detail in Chapter 4, the instantaneous and averaged vector files were imported into Tecplot visualization software for presentation as speed and vorticity plots.

## Experimental Factors Affecting Results

It is important to emphasize that the testing and data collection completed in support of this investigation makes up only one component of a more extensive cavity flow research initiative currently underway at UTSI.  The results and analysis of this study will be used to augment future results forthcoming from complementary rod in crossflow investigations.  With that in mind, there was one factor in particular that is believed to have affected the results obtained within this present body of work.

Although the objectives of this study focused on investigating cavity flow characteristics and the effects of a rod in crossflow in the subsonic range, specific constraints and time limitations arose that led to the decision to conduct the tests using the Mach 1.8 supersonic nozzle already installed in the wind tunnel.  Operating the tunnel at a condition outside of the intended design of the nozzle, e.g. $M < 1$, resulted in downstream flow conditions unique to the particular circumstances of this investigation. Specifically, the research was planned to have a turbulent boundary layer velocity profile entering the test section.  However, vector analysis of instantaneous and averaged results revealed the presence of a region near the tunnel floor of very low kinetic energy, which was more representative of a shear layer like velocity profile.  Although not preferred, it did not prevented the experiment from being completed, or detracted any value from the analysis of the results.  A more complete description of the observed flow characteristics is presented in the PIV analysis results of Chapter 4.

A second factor that was also identified as influencing the results was the use of mass flow rate as the tunnel control parameter.  With the current setup and control systems of the HSWT, it appeared that the effect of using mass flow rate as the controlling parameter was to reduce the degree of repeatability in obtaining one desired flow Mach number. It was observed that flow Mach number was not directly linked to a particular mass flow setpoint, several other system and flow parameters came into play. Further discussion of effects of this factor, along with an appropriate error analysis, will be presented alongside the results reported in Chapter 4.

The last experimental factor affecting the results that will be discussed was the condition of the PIVCAM's CCD. Although the camera remained functional throughout the experiment, one complete column of pixels and several other individual pixels of the CCD appeared to be inoperative. The effect of these inoperative pixels was to produce spurious vectors, and/or small voids where velocity measurements could not be made by the cross correlation process. The Baseline velocity calibration image shown in Figure 12 clearly shows the presence of the inoperative column of pixels at 14.9cm on the ruler, as well as at least three lone inoperative pixels above the ruler at 10.4cm, 11.2cm, and 13.1cm. These inoperative pixels gave rise to questionable results in each of the flow visualization images near the following x-coordinate locations; x = 24mm, 32mm, 51mm, and 69mm.

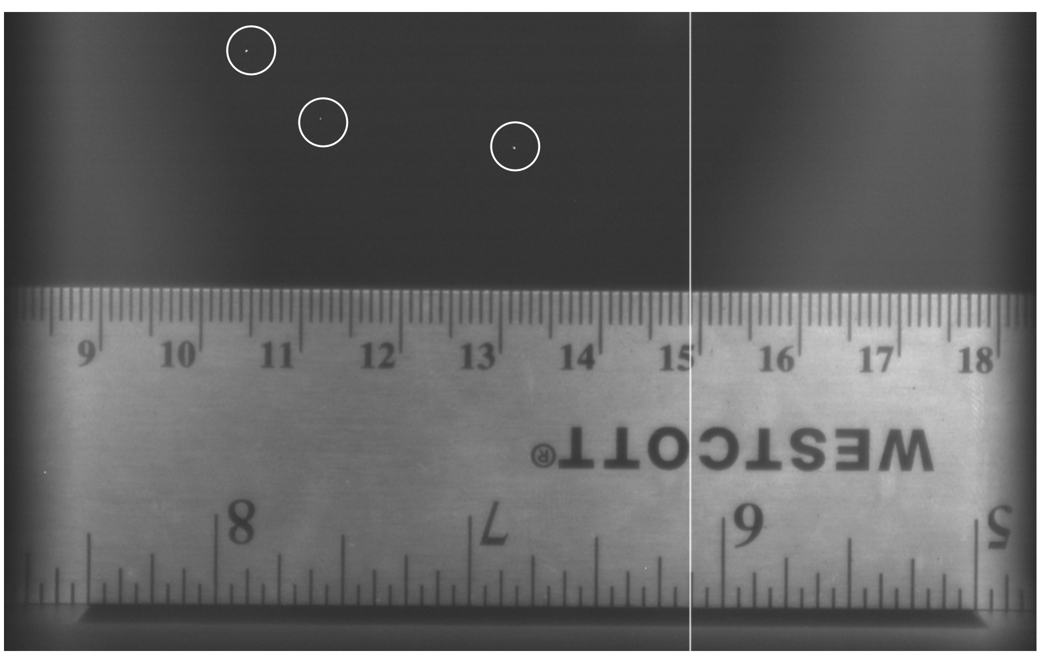


**Figure 12: PIV calibration image highlighting inoperative pixels.**

# CHAPTER 4

# EXPERIMENTAL RESULTS

To satisfy the objectives identified in the introduction, the approach of this chapter will be to begin with a discussion of the unique flow characteristic that was observed in the first phase of testing, and remained present to some degree throughout each phase of testing. Mention of the variations in Mach number through each phase of testing will also be made, along with comments concerning the associated error of those measurements. With the basic flow conditions described, the focus will turn first to a discussion of the spectral data that was collected in each of the four phases. This will include analysis of both the frequency spectra that were observed in each configuration, and the effect of the rod in crossflow on the resonant tones present in the Baseline configuration. The focus will then shift to a discussion of the flow visualization results produced from vector analysis of the PIV images. Both averaged speed and vorticity results will be presented and compared for each configuration, as well as a similar discussion of instantaneous vorticity measurements.

## HSWT Flow Conditions

As previously noted, the effect of using a Mach 1.8 supersonic nozzle to conduct this subsonic flow experiment was that a region of low kinetic energy flow was observed along the tunnel floor of the test section. One explanation for this region of low kinetic energy is that the flow remained subsonic downstream of the throat and was diffused by the diverging cross-section of the nozzle, leading to an increase in static pressure. In terms of the boundary layer developing along the walls of the tunnel, it would have encountered an adverse pressure gradient and is believed to have resulted in separated, or near separation, flow. Evidence suggesting the presence of this particular flow characteristic was first observed in a plot of the velocity measurements that became available following the vector analysis of individual PIV images.

In order to fully investigate this issue of very low kinetic energy flow near the floor and rule out the possibility that errors were introduced through the PIV images or vector analysis, validation, and smoothing process, further analysis of the PIV images and "unvalidated" vector files were conducted. To compare this region of interest in two different configurations, the U(x,t) component of the Clean and Baseline instantaneous velocity measurements are presented as normalized velocities, "$U/U_\infty$", in Figure 13. Each dataset was taken from the velocity calculations of a single image pair as the flow entered the test section just ahead of the leading edge of the cavity. The side-effect of this sudden drop in velocity, e.g. very large $\left|\frac{\partial u}{\partial y}\right|$, was realized when the data was imported into Tecplot and the vorticity calculation was executed. The flow field visualization of Figure 14, displaying non-dimensional vorticity contours overlaid with velocity vectors, reveals how the drop in velocity translated into a very well defined layer of negative vorticity spanning the image at approximately, Y = 5 mm. This layer of vorticity is another aspect of the low kinetic energy flow characteristic that persists, to varying degrees, throughout all of the flow visualization images to follow.

The other two features of Figure 14 that must be discussed are the large number of intense spots of negative and positive vorticity, and the presence of spurious vectors that are scattered throughout the image. The majority of those vorticity spots and spurious vectors can be attributed to the inoperative CCD pixels noted at the end of Chapter 3, particularly those areas in proximity to the locations noted earlier, above X = 24mm, 32mm, 51mm, and the vertical column near X = 69mm. The other explanation for the apparently erroneous results is that the data presented in Figure 14 was raw, unvalidated, data that had not yet been passed through the vector validation process.

To summarize, the purpose of presenting the unvalidated and instantaneous results in Figures 13 and 14 was to illustrate the unique flow characteristics that were observed entering the test section. Knowing that these features existed in the clean tunnel

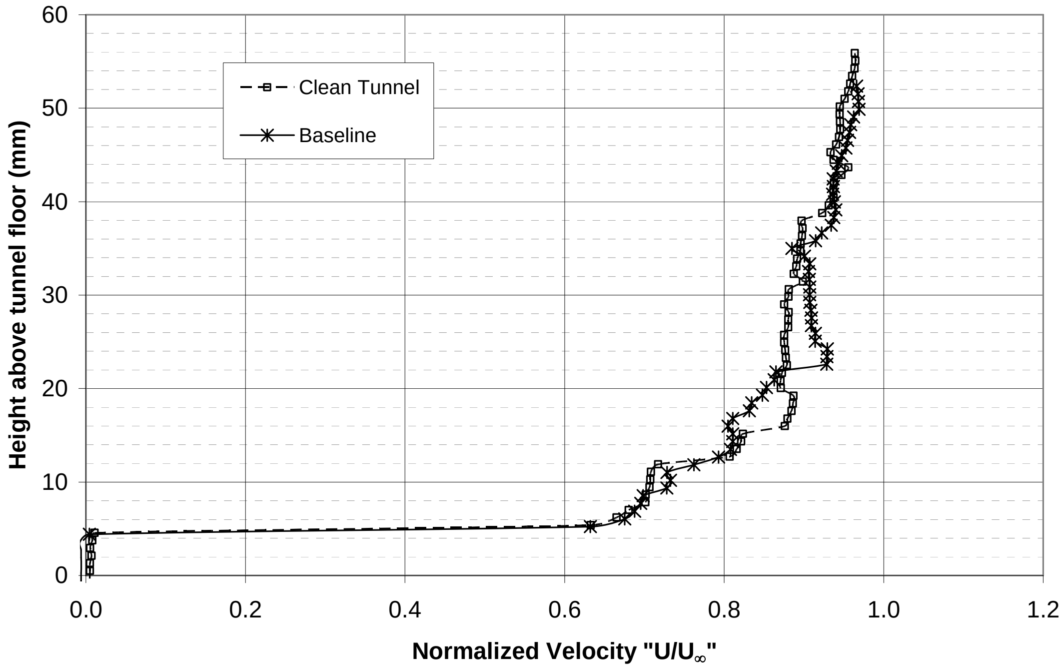


**Figure 13: Velocity profiles of flow entering the test section.**

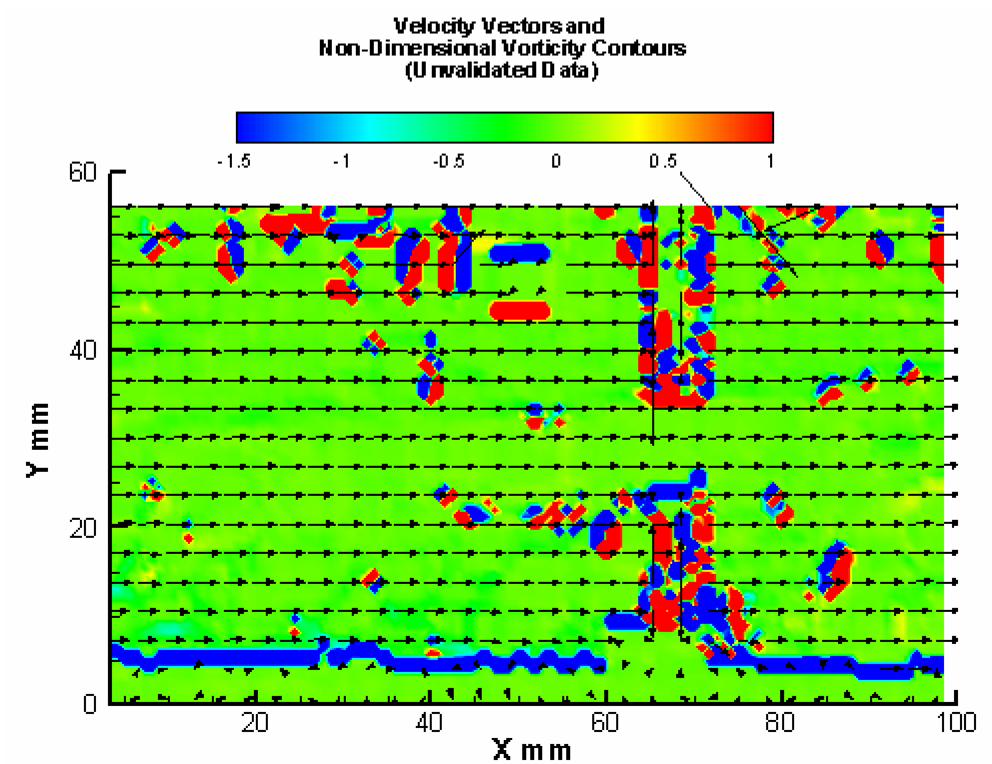


**Figure 14: Instantaneous velocity and vorticity of flow entering the test section.**

configuration will be useful when it comes to the flow visualization analysis of the remaining configurations.

One last issue related to the general flow conditions that remains to be discussed was the use of mass flow rate as the parameter selected to control tunnel Mach number. Despite the obvious connection between mass flow rate and Mach number, it was identified that the use of a particular mass flow rate setpoint in one test sequence did not mean that a similar Mach number flow would be achieved by using that same setpoint in the next sequence. To illustrate this point, Table 4 contains a snapshot of the Mach number variations that were observed for specific mass flow rate setpoints from several configurations and run sequences. Table 4 shows that although it was possible to achieve the desired test Mach number, M = 0.55, with a mass flow setpoint of 14.7 lbs/sec in Run 3 of the Clean configuration, by Run 5 of that same configuration the flow Mach number was up to almost M = 0.62, resulting in a percent error over this particular run sequence

**Table 4: Examples of Mach number variation for a given mass flow rate setpoint.**

| Configuration – Run # | Mass Flow Rate Setpoint (lbs/sec) | Instantaneous Mach Number | Percent Error |
|---|---|---|---|
| Clean – 3 | 14.702 | 0.556 | 5.8% |
| Clean – 4 | 14.702 | 0.584 | |
| Clean – 5 | 14.702 | 0.618 | |
| 1/8" Rod Signature – 9 | 14.405 | 0.571 | 13.6% |
| 1/8" Rod Signature – 10 | 14.405 | 0.551 | |
| 1/8" Rod Signature – 11 | 14.405 | 0.524 | |
| 1/8" Rod Signature – 12 | 14.405 | 0.498 | |
| 1/4" Rod Signature – 1 | 14.002 | 0.541 | 11.5% |
| 1/4" Rod Signature – 2 | 14.002 | 0.509 | |
| 1/4" Rod Signature – 3 | 14.002 | 0.493 | |
| 1/4" Rod Signature – 4 | 14.002 | 0.483 | |
| Baseline – 1 | 14.055 | 0.493 | 4.8% |
| Baseline – 2 | 14.055 | 0.505 | |
| Baseline – 3 | 14.055 | 0.517 | |
| Cavity + 1/8" Rod – 5 | 13.950 | 0.485 | 4.5% |
| Cavity + 1/8" Rod – 6 | 13.950 | 0.495 | |
| Cavity + 1/8" Rod – 7 | 13.950 | 0.495 | |
| Cavity + 1/8" Rod – 8 | 13.950 | 0.473 | |

of 5.8%. This was a fairly reasonable margin of error, but the percent error in Mach number for a given setpoint reached a value as high as 13.6% for the 1/8" Rod Signature configuration.

At the start of this experiment the intent was to conduct the cavity flow investigation at a flow Mach number around M = 0.55. However, as evident from the results in Table 4, the main challenge of the experiment became one of adjusting the mass flow setpoint to give a flow Mach number allowing for the identification of the peak resonant tone created by the cavity, while at the same time not moving so far away from the desired Mach number that the overall flow field conditions were different from one configuration to the next.

This concludes the review of the basic flow conditions that were observed over the course of this investigation, and attention will now turn to presenting and discussing the findings related to the two primary objectives of this thesis. The two categories of experimental results, namely Spectral and Flow Visualization, were each associated with one of the two objectives, and for ease of comparison and analysis they will each be presented separately starting with the Clean Tunnel results of Phase 1, and progressing through to the Cavity + Rod configuration results of Phase 4. It should also be mentioned that given the variation of flow Mach number described above, all of the results to follow will highlight the average flow Mach number that was recorded over the time it took to complete each configuration and run sequence. In addition, as the main trigger signal from the LASERPULSE synchronizer was not interfaced to the Tunnel Control System computer it was not possible to make direct correlations between the Spectral and Flow Visualization results.

## Spectral Data Results

Overall, the collection of transient pressure oscillations detected by the Endevco dynamic pressure transducer went relatively smoothly. There were some instances however, where the tunnel flow conditions had to be varied slightly so as to identify and maintain the peak acoustic tones, either being shed from the rod(s) alone in Phase 2, or being created by the cavity shear layer and rod interactions in Phases 3 and 4. The main features of interest in the Spectral data analysis are: 1) the Overall Sound Pressure Level (OASPL) of the broadband noise; 2) the presence and amplitude of any well defined resonant frequencies; and 3) the presence and amplitude of any harmonic frequencies. As a reminder, the data for the Rod Signature spectra was sampled at a rate of 40 KHz, for a frequency range of 20 KHz, while the spectral data for the remaining three configurations was sampled at 10 KHz, giving a range of 5 KHz.

It was stated earlier that the purpose of collecting data from the tunnel with no model or cavity in the test section was to identify any distinguishing acoustic characteristics inherent to the design or operation of the tunnel. The four test run sequences for this Phase 1 Clean configuration were conducted at an average flow Mach number of M = 0.57, and each of the other three datasets possessed similarly featured acoustic spectra to the sample presented in Figure 15. In this case, the main features of interest in the acoustic spectrum are: 1) an OASPL of approximately 120 dB was observed in the frequency range from 0 to 1750 Hz and then tended towards 114 dB above 1750 Hz; 2) there were no resonant frequencies present; and 3) consequently no harmonics were present. One observation however, was that with a broadband noise OASPL of approximately 115 dB, it was anticipated that the acoustic spectrum of the other test configurations would potentially be dominated by this broadband noise level as it was an inherent feature of operating the tunnel.

Moving on to the Rod Signature configuration of Phase 2, it was anticipated that by using the dynamic pressure transducer mounted flush with the floor of the tunnel, it would be possible to determine the frequency at which vortices were shedding from the rod(s) in crossflow. However, the dynamic transducer was only able to detect pressure oscillations in the wake of the 1/4" rod, and nothing of any interest in the wake of the 1/8" and 3/16" rods. Considering the height of the rod(s) above the floor of the

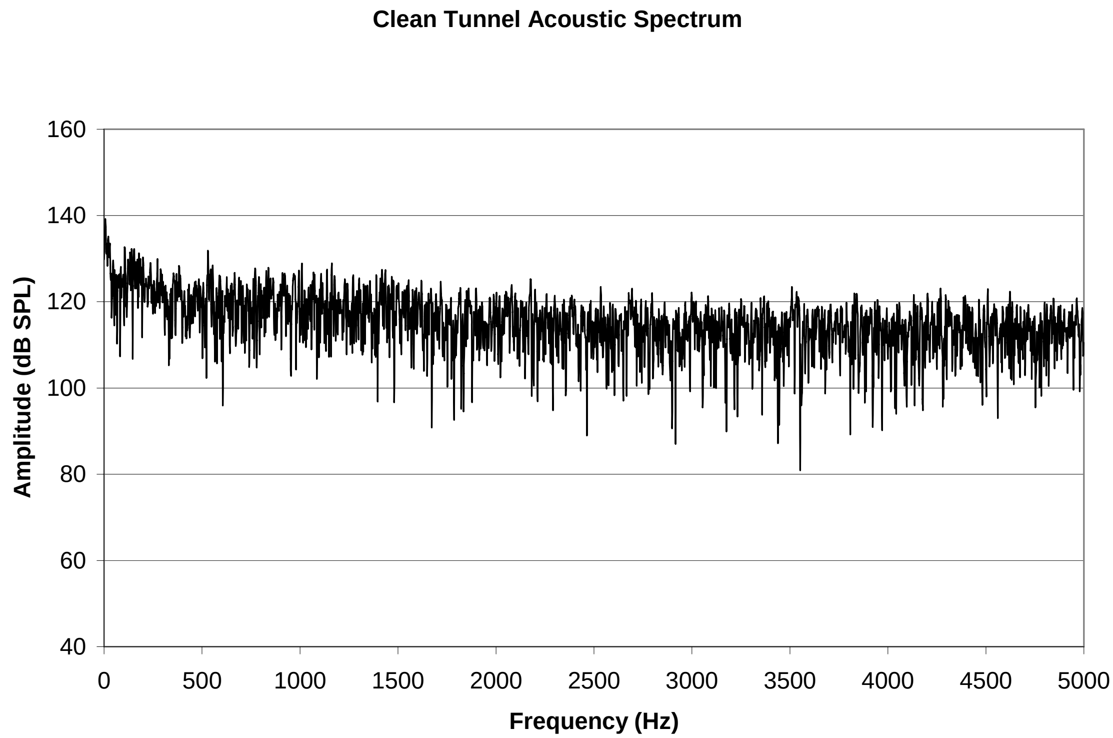


**Figure 15: Clean tunnel acoustic spectrum at average flow M = 0.57.**

tunnel, the initial smaller size of the wakes, the distance downstream to the transducer, and the growth rate of the wake(s), there just may not have been enough time and space for the wakes from the smaller rods to grow to the point where the amplitude of the pressure oscillations would have been "large" enough and/or close enough to be detected by the transducer. Whatever the reason, the results obtained for the 1/4" Rod Signature do contain specific features of interest. 1/4" Rod Spectrum # 3-2, contained in Figure 16, was one of six collected during the test sequence for this configuration, and was chosen because it possesses features that are representative of each of the other five spectra.

In particular, the features of interest in Figure 16 are: 1) a broadband noise OASPL between 0 and 1750 Hz of approximately 115 dB, an average level of 110 dB SPL between 1750 and 5000 Hz, and just above 100 dB SPL beyond 5 KHz; 2) the

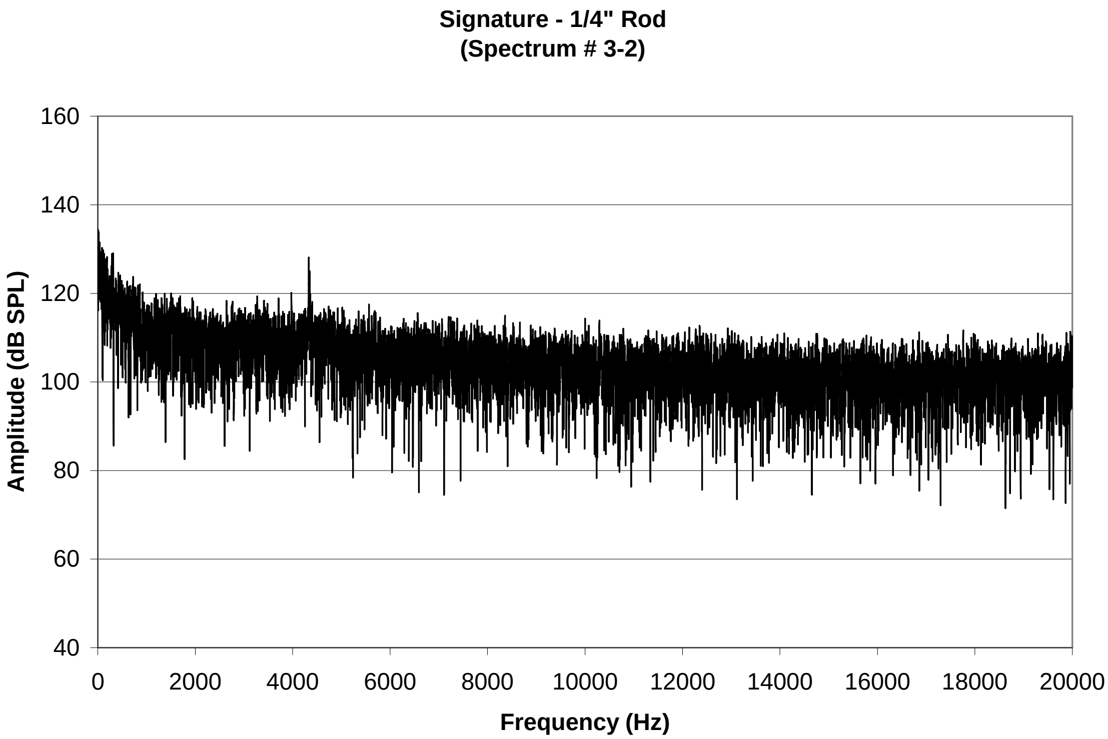


**Figure 16: Acoustic signature of 1/4" Rod at average flow M = 0.50.**

presence of a 128 dB SPL resonant peak at 4332 Hz; and 3) there does not appear to be any visible harmonics of the resonant peak across the 20 KHz range. In looking at the first feature, and comparing this configuration to the Clean Tunnel, there was consistently an OASPL reduction of approximately 5 db in the broadband noise below 5000 Hz. Because the average flow Mach number for this run sequence was M = 0.5, as compared to M = 0.57 for the Clean Tunnel, it is difficult to determine whether the reduced amplitude is attributable to the small reduction in velocity, or to the introduction of the Rod into the “noisy” tunnel. Although it was not a result that had specifically been anticipated, the fact that the rod in crossflow apparently reduced sound pressure levels of the clean tunnel is an interesting one and may require further investigation to verify and explain. As for the second feature, the shedding peak at 4332 Hz, it should be recalled from Chapter 3 that based upon an anticipated Mach number, M = 0.55, and modified Strouhal number, St = 0.165, the shedding frequency estimated for this diameter rod was

4900 Hz.  Considering the slightly lower than anticipated Mach number, the experimental results align very well with theoretical expectations.

For a more complete analysis of the results collected in this configuration, Table 5 summarizes the shedding characteristics from all six of the 1/4" Rod Signature spectra. Aside from the first shedding frequency, highlighted by (?), which will be discussed shortly, the rest of the data collected in this configuration agree relatively well from one sequence to the next.  In particular, the rod shedding frequencies measured by the dynamic pressure transducer display a very high level of agreement, with a percent error between them of less than 1 %.   Another feature of Table 5 worth discussing is the calculated Strouhal numbers, and their agreement with the modified Strouhal number, St = 0.165, mentioned earlier.  Considering the flow condition results introduced at the start of this chapter, the reasonable agreement of these calculated values with the modified value adds a measure of confirmation that the selected height of the rod above the leading edge of the cavity was similar to previous rod in crossflow studies [18, 19]. Actual levels of suppression achieved in this study remain to be discussed, but will offer final verification as to whether the selected cylinder characteristics and position were satisfactory.

**Table 5: Signature - 1/4" Rod shedding frequency at flow M = 0.50.**

| **1/4" Rod Run #** | **Shedding Frequency (Hz)** | **Peak Amplitude (dB SPL)** | **Avg Velocity (m/s)** | **Calculated Strouhal #** |
|---|---|---|---|---|
| 2-1 | 4722(?) | 121.1 | 172.7 | 0.1736 |
| 2-2 | 4342 | 122.4 | 172.7 | 0.1597 |
| 3-1 | 4324 | 124.6 | 167.1 | 0.1643 |
| 3-2 | 4330 | 128.0 | 167.1 | 0.1645 |
| 4-1 | 4356 | 125.1 | 163.8 | 0.1689 |
| 4-2 | 4338 | 123.8 | 163.8 | 0.1682 |
| % Error | 0.7 % | 4.5 % | 5.3 % | 5.6 % |

The question mark (?) in the first row of data of Table 5 indicates that the validity of this result remains in question.  Even with consideration given to the variation in Mach number previously noted, the highest velocity recorded over the possible sample range for this sequence was 180 m/s. A value not so much greater than the other average velocities that it would have caused the rod shedding frequency to be that much higher than the other samples.

Examination of the following results from Phase 3 of testing takes the analysis one step closer to the main area of focus for this study. Presented in Figure 17 is Baseline Spectrum # 2-1, recorded moments before the PIV images were captured during the second test sequence of the cavity only configuration, and representative of the other sampled datasets. The key elements of interest appearing in this figure are: 1) an elevated level of broadband noise varying from 125 db SPL below 1750 Hz, down to 116 dB SPL above 1750 Hz; 2) a well defined 151 dB SPL resonant tone at 1414 Hz; and 3) although some slightly elevated 'humps' appear just above 500 Hz and 2750 Hz the rounded humps are too broad in form to be considered harmonics of the resonant peak tone.

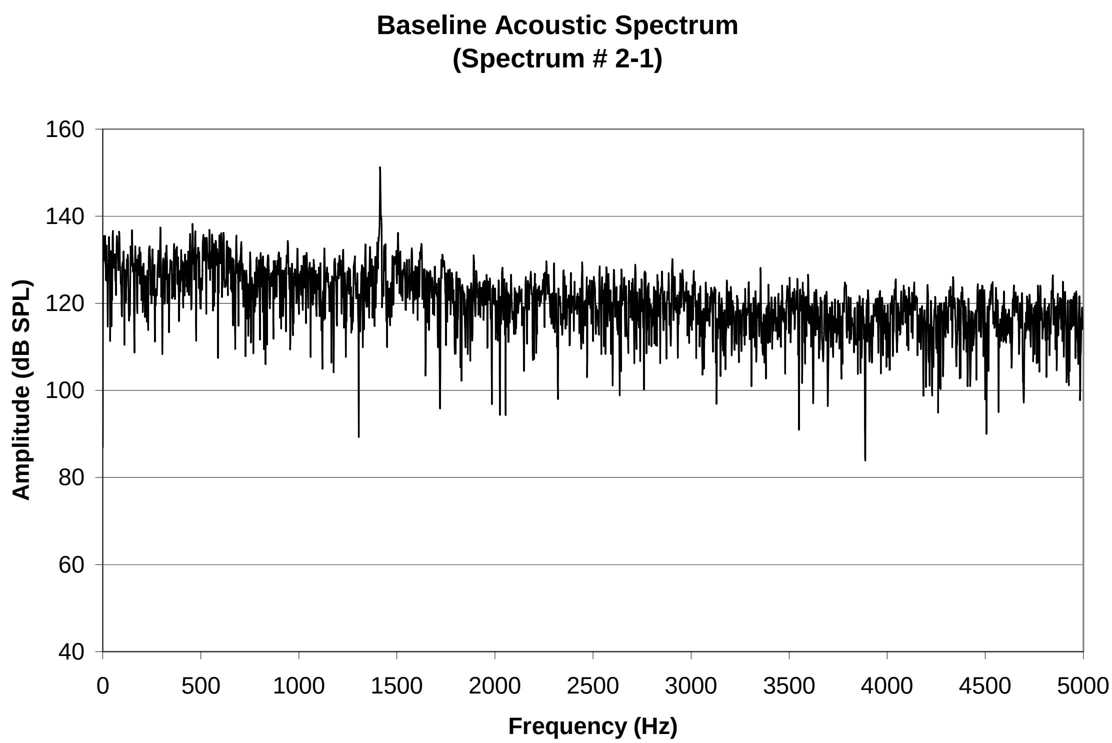


**Figure 17: Baseline acoustic spectrum of L/D = 3.5 cavity at average flow M = 0.51.**

In comparing the representative Clean Tunnel and Baseline acoustic spectra of Figures 15 and 17, there was an OASPL increase in the broadband noise between 2 to 5 dB SPL. The lower half of the frequency range of the Baseline sample appeared to be more affected by the presence of the cavity than the upper half of the frequency range, suggesting that the cavity added an amplifying effect across the whole range of lower frequencies. The presence of the 151 dB resonant peak tone generated by the cavity shear layer interactions at 1414 Hz was also likely to have been a large contributor to the overall increase. With regards to the frequency of the resonant peak being 1414Hz, it is closest to the Mode 2 Rossiter tone of 1610 Hz predicted earlier in Table 2. However, if the average flow Mach number, M = 0.51, for this sequence were applied to the modified Rossiter equation (Equation 2), the calculated Mode 2 tone would be 1517 Hz, closer yet to the observed value.

A summary of all the acoustic spectrum results from the Baseline configuration is provided in Table 6. The percent error calculations at the bottom of the frequency and amplitude columns, 0.85 % and 8.07 % respectively, reveal that the cavity showed a high degree of repeatability in producing resonant peaks at an average frequency of 1413 Hz, while there was slightly more variation in the average peak amplitude of 148.7 dB SPL. Using the average tunnel velocity for each sequence, which was added to the table to facilitate the calculation of the cavity length based Strouhal number, $St_L$, it was determined that the average calculated Strouhal number, $St_L = 0.7308 \pm 5.15\%$, available from this investigation of a cavity with L/D = 3.5 at a flow Mach number, M = 0.51, falls just short of Tam & Block's [10] theoretical prediction of approximately 0.85, estimated from Figure 2 presented earlier. Some of this Table 6 data from the Baseline configuration will be used again shortly for comparison with Phase 4 results.

With the analysis of the acoustic spectra from the first three configurations complete, the information necessary to complete an assessment of the suppression capabilities of each one of the three cavity + rod in crossflow configurations is available.

**Table 6: Baseline peak tones generated by L/D = 3.5 cavity at flow M = 0.51.**

| **Baseline Spectrum #** | **Frequency (Hz)** | **Amplitude (dB SPL)** | **Tunnel Velocity** | **Calculated Strouhal #,** $St_L$ |
|---|---|---|---|---|
| 1-1 | 1418 | 153.1 | 168.2 | 0.7495 |
| 1-2 | 1416 | 149.4 | 168.2 | 0.7485 |
| 2-1 | 1414 | 151.0 | 171.1 | 0.7349 |
| 2-2 | 1426 | 141.1 | 171.1 | 0.7411 |
| 3-1 | 1410 | 143.9 | 175.6 | 0.7139 |
| 3-2 | 1406 | 148.6 | 175.6 | 0.7119 |
| 4-1 | 1408 | 150.4 | 172.9 | 0.7238 |
| 4-2 | 1406 | 152.7 | 172.9 | 0.7227 |
| **Average Value** | 1413 | 148.7 | 171.9 | 0.7308 |
| **% Error** | 0.85 % | 8.07 % | 4.30 % | 5.15 % |

In this configuration, unlike the Phase 2 Rod Signature instance, the collection of dynamic pressure oscillations from each of the three different diameter rods positioned above the leading edge of the cavity was successful. The acoustic spectrum obtained from the Cavity + 1/8" Rod sequence is presented in Figure 18, the Cavity + 3/16" Rod acoustic spectrum in Figure 19 and the acoustic spectrum from the Cavity + 1/4" Rod configuration is provided in Figure 20. In an attempt to maintain a sense of flow in this potentially lengthy discussion, the format used to describe the main features of interest of the Phase 1, 2, and 3 results will be adjusted slightly. One feature will be discussed at atime, with comments related to the characteristics of that feature in each of the three representative spectra. Once the general features of Phase 4 have been described, a table summarizing the specific details of each configuration and test sequence will be presented and discussed.

Starting with a general description of the first feature of interest, the overall sound pressure level of broadband noise, a comparison of the spectra in Figure(s) 18, 19, and 20, reveals a direct correlation between the diameter of the rod in crossflow and the percent reduction in the OASPL of the broadband noise. As the diameter of the rod increased from 1/8", to 3/16", to 1/4", there was a definite, yet only slight, reduction of approximately 4 % in the OASPL of broadband noise. This trend was not just visible in the individual spectra of Figures 18, 19, and 20, but was consistent across all 19 of the spectra collected over the duration of the three different diameter test sequences. In comparing the broadband noise OASPL feature of these three figures to the Baseline spectrum of Figure 17, there appears to have been a slight increase in broadband noise with the first use of the 1/8" rod above the cavity. However, a comparison of the Baseline and the Cavity + 1/4" Rod spectra, Figures 17 and 20 respectively, shows a reduction of approximately 4 dB in the OASPL of the broadband noise.

The characteristics of the next feature of interest, the presence and amplitude of well defined resonant frequencies, are of primary importance as they will form the response to one of the two objectives of this investigation. From the Baseline results of Phase 3, it was known that the cavity produced a resonant peak in the spectrum at an average frequency of 1413 Hz. Knowledge of the successful application of the rod in crossflow technique suggested that it was possible to achieve acoustic suppression levels in the range of 10 to 30 dB. The representative acoustic spectra plotted in Figures 18, 19, and 20, satisfied expectations and exhibit the suppression capabilities of the rod in crossflow technique. In terms of the average values tabulated in Table 7, increasing levels of suppression, from 7.3 to 15.1 dB, were realized as the rod diameter increased from 1/8" to 1/4".

Finally, there are only a couple of points to make about the third feature of interest, the presence and amplitude of any harmonic frequencies. Examination of Figures 18, 19, and 20, reveals that no harmonics are present. However, if one recalls the small ‘humps’ that were detected in the Baseline acoustic spectrum, it appears that they too have been suppressed in these Cavity + Rod acoustic spectra.

That concludes the general description of the acoustic spectra from each of the three different Cavity + Rod configurations. Next, more specific details from each of the test run sequences will be presented and briefly discussed.

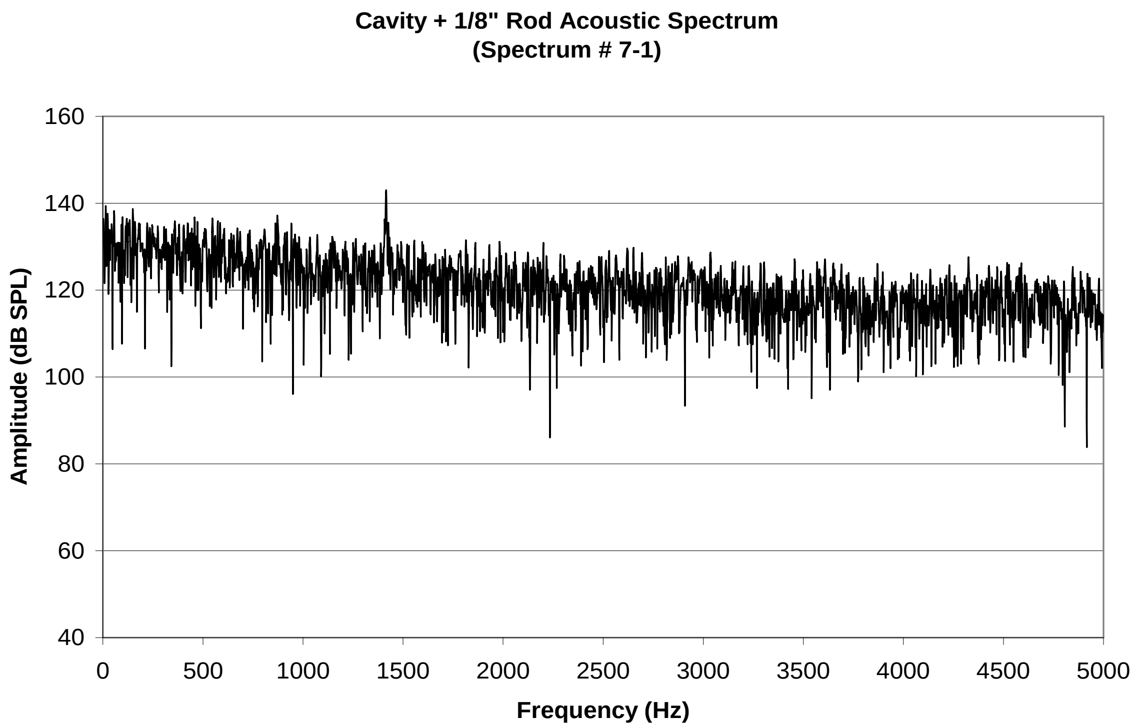


**Figure 18: Cavity + 1/8" Rod acoustic spectrum at average flow M = 0.49.**

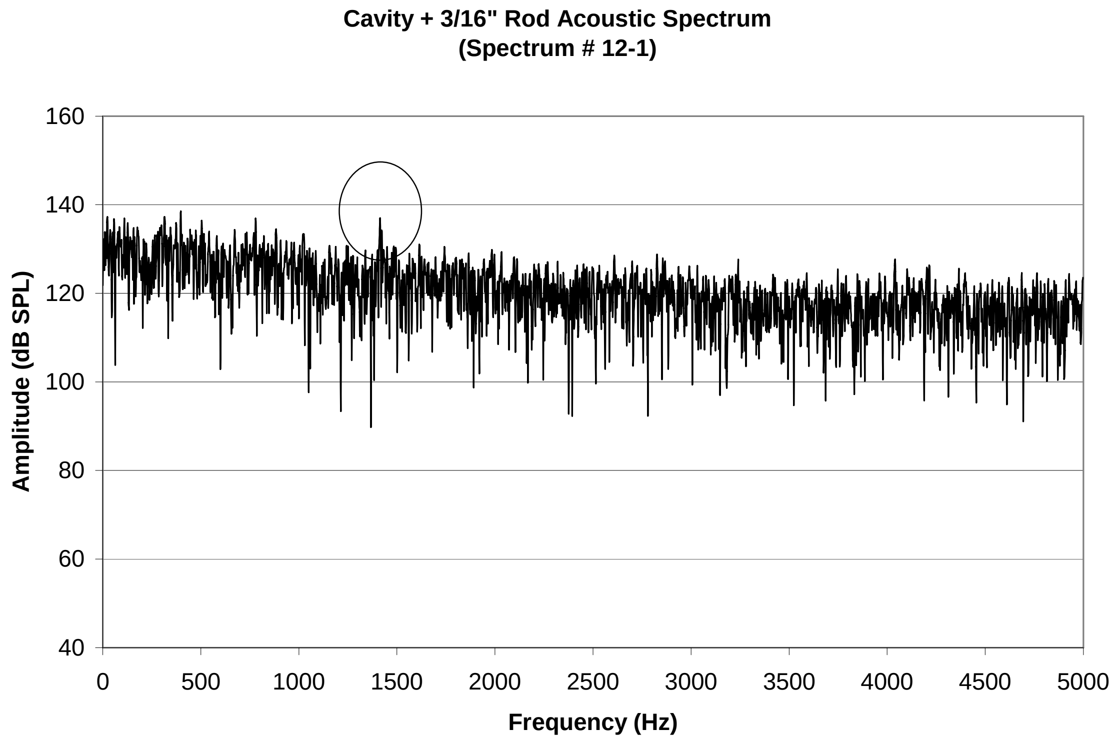


**Figure 19: Cavity + 3/16" Rod acoustic spectrum at average flow M = 0.51.**

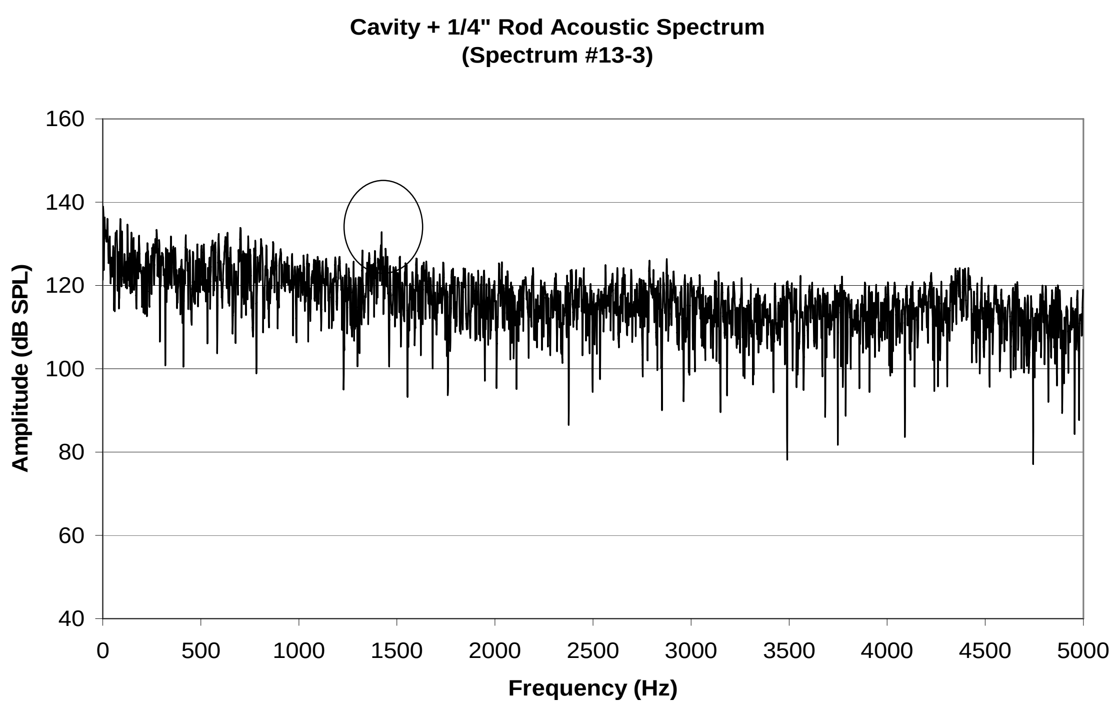


**Figure 20: Cavity + 1/4" Rod acoustic spectrum at average flow M = 0.50.**

Having completed the general review of the characteristic features of the Cavity + Rod acoustic spectra, more specific results of the resonant frequency and peak amplitudes recorded during each of the test run sequences from the fourth phase of testing are listed in Table 7. For comparison purposes, the first two columns of the table repeat the resonant frequency and peak amplitudes produced by the Baseline, cavity only configuration. The average values and error analysis percentages shown in the bottom two rows of Table 7 offer further quantitative support to the qualitative analysis already submitted. The average resonant frequency produced by the cavity, with or without the rod, ranged from 1413 Hz to 1425 Hz and never varied by more than 1.27%. As for the peak amplitude of the resonant frequency, its average value consistently dropped from the Baseline level of 148.8 dB SPL, and largest margin of error of 8.07%, down to the lowest average value of 133.7 dB SPL, and smallest margin of error of 2.70%, with the 1/4" Rod in crossflow.

So, despite the initial concern about the region of low kinetic energy entering the test section, not only was the collection of the dynamic pressure data from each of the Cavity + Rod configurations successful, but the analysis of the characteristics features of the associated frequency spectra convincingly proves the ability of the rod in crossflow technique to reduce the overall sound pressure level of the resonant peaks created by the cavity.

To conclude the review of Spectral data results, Figure 21 satisfies the first objectives of this study: *To compare the level of acoustic suppression offered by different diameter rods in crossflow above the leading edge of the cavity.* It illustrates the increasing level of acoustic suppression afforded by increasing the diameter of the rod placed in crossflow. These results will be considered together with the flow visualization results of the next section to arrive at an overall conclusion regarding this cavity flow investigation.

**Table 7: Comparison of suppression levels with different diameter Rods in Crossflow**

| | Baseline | | Cavity + 1/8" Rod | | Cavity + 3/16" Rod | | Cavity + 1/4" Rod | |
|---|---|---|---|---|---|---|---|---|
| | Frequency (Hz) | Amplitude (dB SPL) | Frequency (Hz) | Amplitude (dB SPL) | Frequency (Hz) | Amplitude (dB SPL) | Frequency (Hz) | Amplitude (dB SPL) |
| | 1418 | 153.1 | 1424 | 142.9 | 1428 | 136.7 | 1434 | 134.5 |
| | 1416 | 149.4 | 1424 | 137.8 | 1410 | 135.6 | 1422 | 132.4 |
| | 1414 | 151 | 1416 | 138.1 | 1412 | 137.3 | 1422 | 132.8 |
| | 1426 | 141.1 | 1416 | 142.9 | 1424 | 133.0 | 1424 | 133.0 |
| | 1410 | 143.9 | 1418 | 144.2 | 1412 | 132.2 | 1424 | 136.0 |
| | 1406 | 148.6 | 1416 | 142.4 | 1414 | 137.0 | | |
| | 1408 | 150.4 | 1422 | 142.3 | 1410 | 134.5 | | |
| | 1406 | 152.7 | | | | | | |
| **Average Value** | 1413 | 148.8 | 1419 | 141.5 | 1416 | 135.2 | 1425 | 133.7 |
| **% Error** | 0.85 % | 8.07 % | 0.56 % | 4.48 % | 1.27 % | 3.75 % | 0.84 % | 2.70 % |

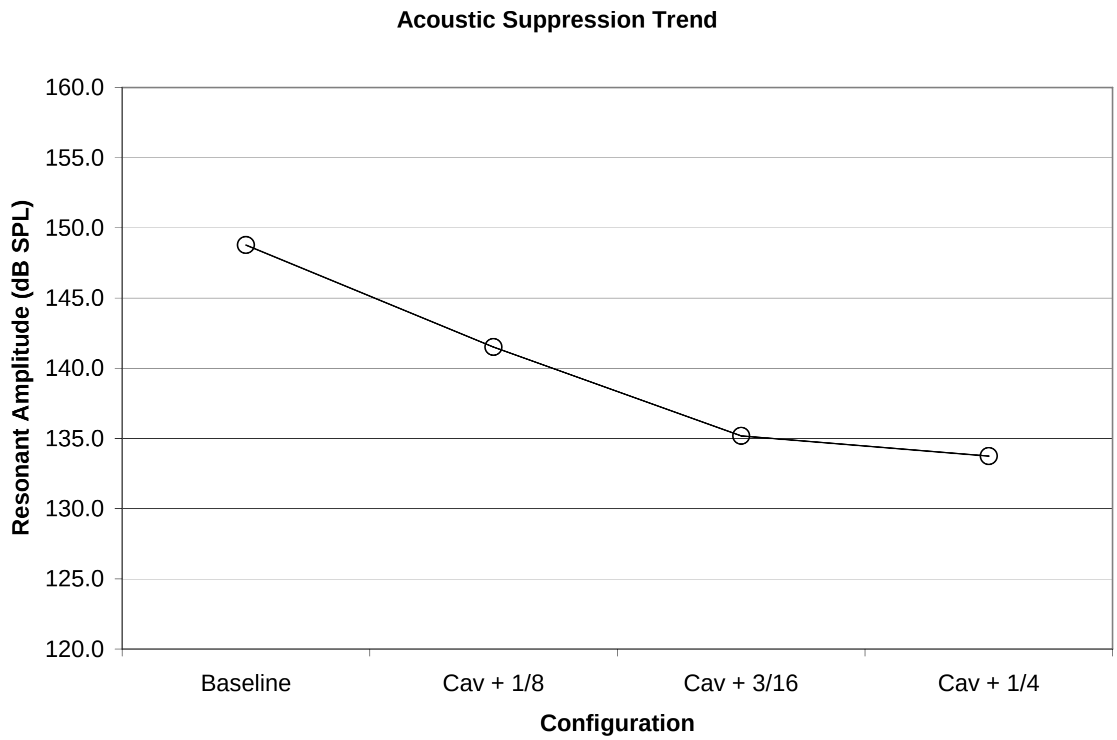


**Figure 21: Comparison of acoustic suppression by configuration.**

## Flow Visualization Results

To satisfy the second objective of this study, the velocity vector files obtained following the cross-correlation of the PIV image pairs were used to create plots of both the average and instantaneous flow field velocity and vorticity. However, prior to the vector files being used to calculate and interpret flow field behavior they were validated using the INSIGHT™ software filtering functions to remove spurious vectors and fill in void spots that had arisen due to a combination of the inoperative CCD pixels noted earlier and mismatches in the cross-correlation process.

The process used to validate the raw vector data files included application of the following filters:

1) Global Range – used to remove vectors with velocity values known to be outside the specified range. The minimum and maximum velocities specified in this range filter process were: $U_{min}$ = -125 m/s; $U_{max}$ = 205 m/s; $V_{min}$ = -100 m/s; $V_{max}$ = 100 m/s.

2) Local Mean – computed the simple average U and V velocity components of the vectors surrounding a point. A selected tolerance of 75 m/s specified the maximum difference between the mean and local velocity component at the point. Given the relatively large velocity gradients and small void spots present in the flow field, a Neighborhood Size of 3 x 3 was selected, as was the option to Interpolate Fill Holes.

3) Smooth – replaced each velocity vector with a weighted average of the velocity vector and the neighboring vectors. The smoothing filter is designed to filter out high frequency velocity variations caused by uncertainty in measuring the velocity. If at least one valid vector was present within the selected 3 x 3 Neighborhood of vectors the smooth filter filled in temporary blank, or void, spots as well as vectors that failed to satisfy the Signal to Noise Ratio.

The specific filter values described above were determined in the preliminary stages of testing, and were selected so as to identify a middle ground between not enough and too much validation. The effect of each filtering step on the vector field is illustrated in the representative flow fields provided in Figures 22 (a) through (d).

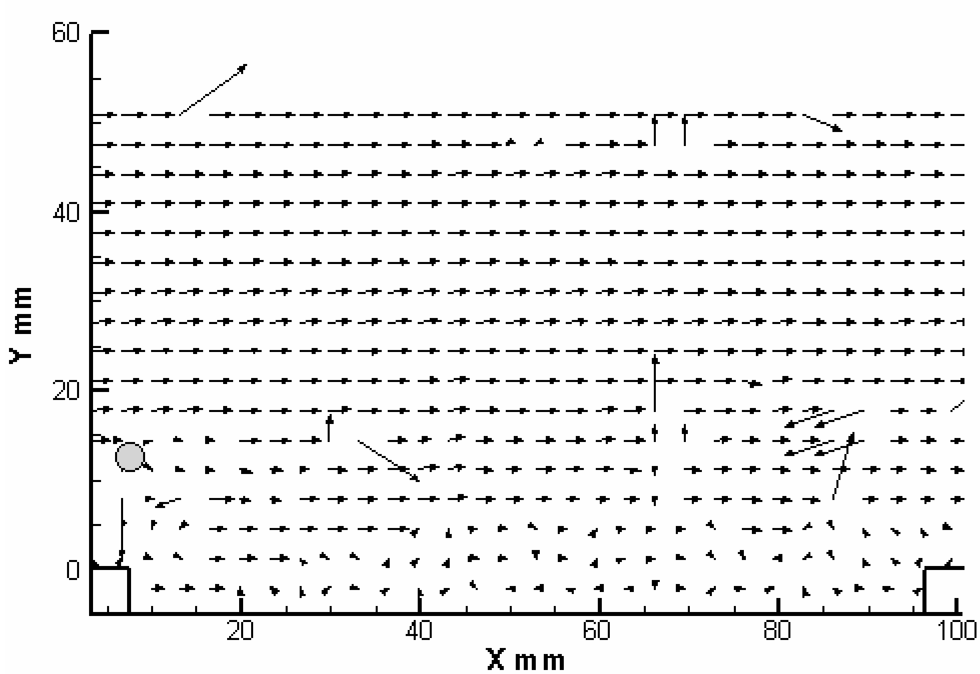


**Figure 22(a): Example of vector field prior to validation and smoothing.**

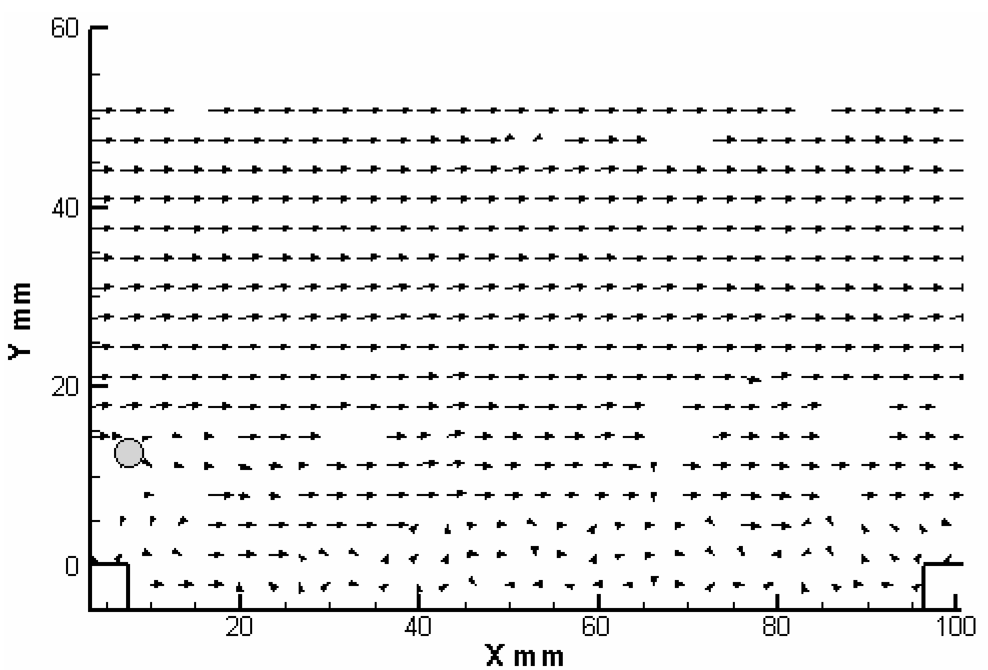


**Figure 22(b): Example of vector field after application of Global Range filter.**

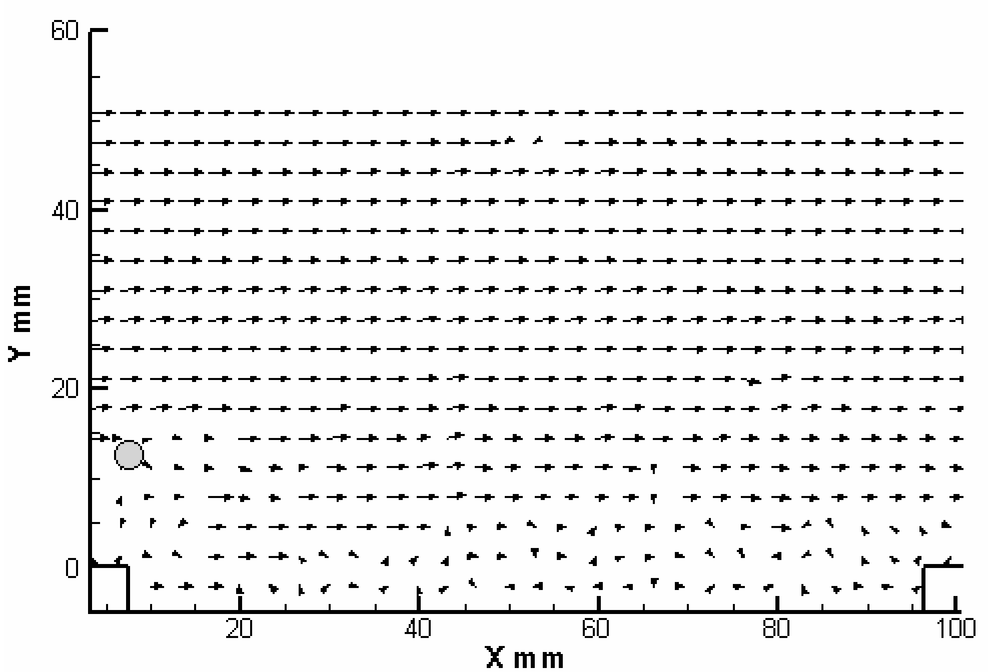


**Figure 22(c): Example of vector field after application of Local Mean filter.**

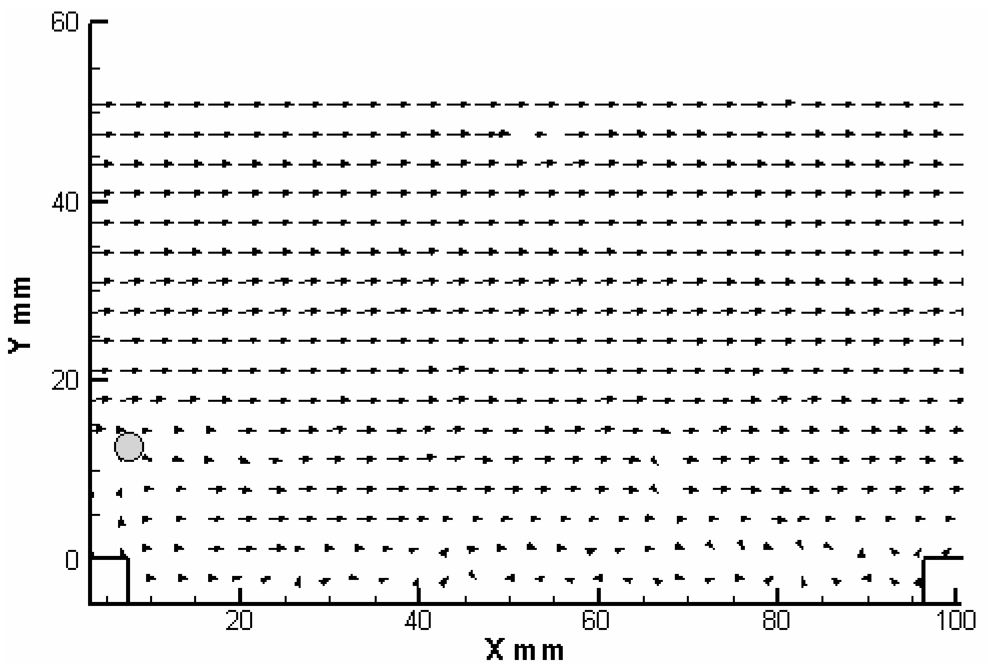


**Figure 22(d): Example of vector field after application of Smoothing filter.**

Despite the use of the filtering steps just described, the influence of the inoperative CCD pixels on the vectors in the areas above X = 24mm, 32mm, 51mm, and the vertical column near X = 69mm, remains immediately apparent. Although the contours in those areas detract from the accurate and complete representation of the flow field characteristics, there was little that could be done to eliminate them. The flow field features that are attributable to the erroneous results resulting from the bad pixels are fairly distinguishable from real flow field behavior and will not be specifically discussed every time.

Before presenting the average velocity and vorticity contour plots, it should be noted that scheduling and resource constraints outside the control of the current investigator limited the amount of time available to complete all four phases of testing. As a result, instead of being able to determine average values from several hundred image pairs, the number of image pairs used in this study ranged from 51 to 56, as specified by configuration in Table 8. The reason for the difference from one configuration to the next was that for some undetermined reason the synchronization between image (a) and image (b) would intermittently be lost and it was impossible to achieve a cross-correlation between the two images. The asterisk, (*), next to the 3/16" Rod Signature value denotes an operator error that resulted in the loss of 14 image pairs.

**Table 8: Number of PIV images pairs available for analysis by configuration.**

| Configuration | # of Available Image Pairs |
|---|---|
| Clean Tunnel | 52 |
| 1/8" Rod Signature | 54 |
| 3/16" Rod Signature | 39 (*) |
| 1/4" Rod Signature | 51 |
| Baseline – Cavity only | 52 |
| Cavity + 1/8" Rod | 52 |
| Cavity + 3/16" Rod | 54 |
| Cavity + 1/4" Rod | 56 |

Another element of the images to be discussed before proceeding concerns the identification of a common reference point across all images. In this case, that common reference point was identified as the centerline of the tunnel floor where the laser light sheet marked the lower boundary of the vector field. For that reason, the Y-component of each vector field was adjusted to ensure that the centerline along the tunnel floor corresponds to Y = 0 mm in each image. In the Phases 3 and 4, the tunnel floor ahead of, and behind, the cavity are positioned at Y = 0 mm, and black lines are used to represent the leading and trailing edges of the cavity. Where seeding particles entered the cavity and were captured in the PIV images, velocity and vorticity information is available within the upper portions of the cavity and are shown below Y = 0 mm.

The approach taken in this analysis will be similar that followed with the Spectral results. The Phase 1 and 2 average and instantaneous velocity and vorticity results are examined first to highlight any distinctive features of the Clean Tunnel and Rod Signature flow fields. This will be followed by a comparative analysis between both the average normalized velocity contours of the Baseline and Cavity + Rod configurations. A separate comparison of the average non-dimensional vorticity contours between the Phase 3 and 4 configurations will also be completed. Chapter 4 will close with a glimpse at several instantaneous non-dimensional vorticity images of the Cavity and Cavity + Rod flow fields.

Beginning with the Clean Tunnel configuration, the average normalized velocity and average non-dimensional vorticity plots captured at a Mach number of 0.57 are presented in Figures 23 and 24 respectively. Ignoring the regions related to the inoperative pixels, the main feature of interest in these two figures is the distinct region of low kinetic energy below Y = 5 mm, discussed at the beginning of Chapter 4. These two figures illustrate the velocity and vorticity flow field conditions inherent to the current setup and operation of the HSWT. Although the blue line of negative vorticity at Y = 5 mm, in Figure 24, will be visible in each of the vorticity figures to come, it will not

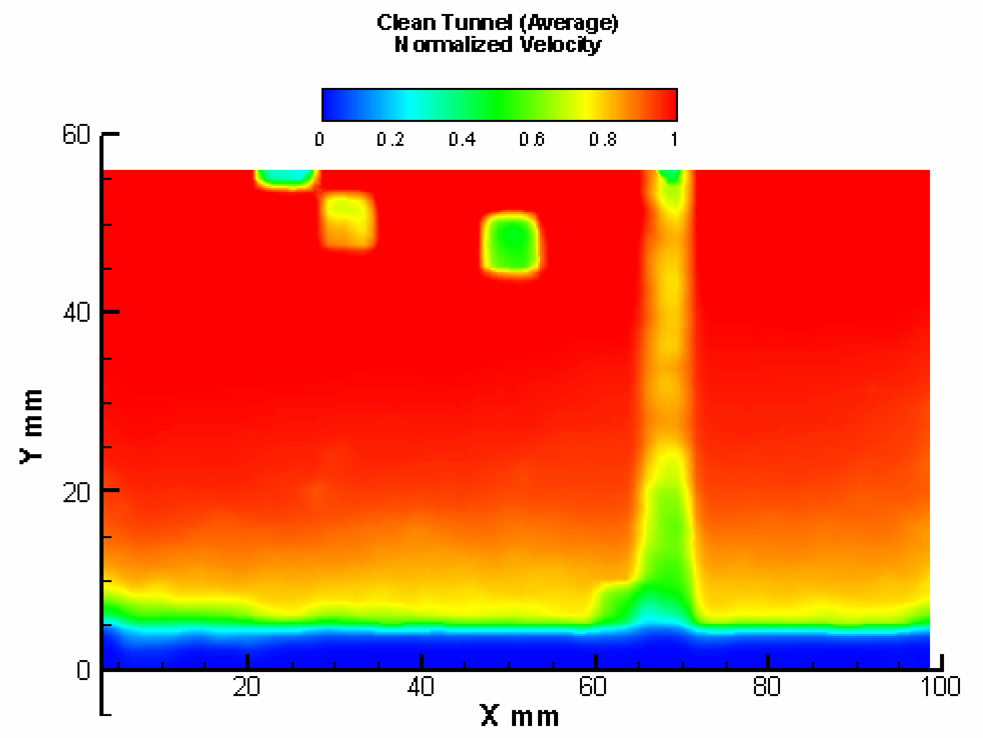


**Figure 23: Average Clean Tunnel velocity contours at flow M = 0.57**

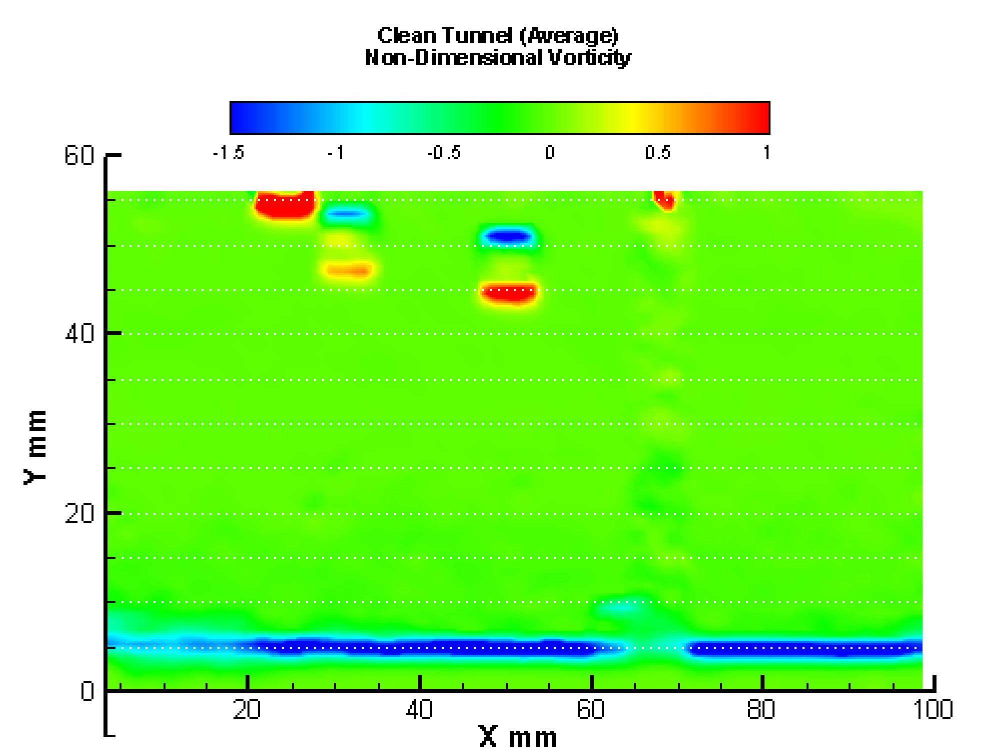


**Figure 24: Average Clean Tunnel vorticity contours at flow M = 0.57.**

always possess the same intensity or thickness, and as such will be used as an indicator of the amount of mixing, or viscous diffusion, that is present in other configurations.

In looking at the front portion of the vorticity line at Y = 5 mm in Figure 24, it is believed the intensity contour has been affected due to the reflection of the laser light sheet and partial saturation of the CCD from, this effect was more pronounced in the Clean Tunnel images near the front of the test section and diminishing downstream.

For ease of comparison, the velocity and vorticity flow fields of the Phase 2 - Rod Signature configurations will be discussed and presented separately. The circles near the front of the each image are scaled representations of the different diameter rods and are positioned appropriately based on the point of illumination by the laser light sheet and their location in the 2-D PIV images. The 1/8" rod in Figure 25 is positioned slightly further downstream of the others because in the process of changing the model from one configuration to the next, the camera was inadvertently disturbed and the small shift in field of view, both forward and slightly up, was not recognized until after the completion of the test sequence. The upwards shift of the camera resulted in the lower boundary of the vector analysis region starting approximately 1 mm above the centerline position along the floor of the tunnel. Despite the small shift in the field of view of the camera, the vector analysis was not affected.

The average normalized velocity contours maps for each of the different diameter rods, moving from smallest, 1/8", to largest, 1/4", are displayed in Figures 25, 26, and 27. As anticipated, the defining feature of this configuration is the wake as it develops downstream of the rod(s) in crossflow. In an effort to examine the development of the velocity flow field downstream of the rod(s), the wake region will be examined at two locations, the first at one cavity depth back from the center of the rod (same as the leading edge location), at X/D = 1.0, and the second just ahead of the trailing edge, at X/D = 3.25. In addition to the velocity contour maps, the averaged vector data files were also used to identify the “U” velocity components of the mean flow at the two locations, and are plotted as normalized velocity profiles in Figures 28 and 29.

The velocity contour levels, and velocity profile inflection points, contained in these five figures were used to examine the following three elements of the wake at the two downstream locations: 1) the vertical position of the greatest velocity deficit; 2) the thickness of the wake; and 3) the shape of the velocity profile.

Beginning with the vertical position of the velocity deficit at X/D = 1.0, each of the Figures, 25 through 28, show evidence that the greatest velocity deficit is located at approximately 12 mm.  In the contour map images the velocity deficit is marked by the contour lines that stretch downstream away from the center of the rods.  Moving downstream to X/D = 3.25 location, the velocity has almost completely recovered for each of the three rods, and the velocity profiles of Figure 29 remain almost unchanged from roughly Y = 9 mm up to Y = 12 mm, before they velocity begins to steadily increase again towards the next rapid change in slope.

The second feature of interest, the thickness of the wake, is easily identifiable with the addition of the velocity contour lines in Figures 25 to 27.  The upward transition of the contour color levels starts with the tight contour lines around Y = 5 mm, just above the region of low kinetic energy flow, and extends up towards the more diffused transition from green, through the yellow band, to the orange contour level.  For the purpose of identifying the wake thickness at each location, and hence the growth rate between the two locations, the inflection points below Y = 10 mm of the velocity profiles in Figures 28 and 29 served as the lower boundary, while the upper boundary was specified at a normalized velocity of 0.9.  With these criteria, the vector data files used to plot the velocity profiles were filtered for the corresponding values, and used to calculate the wake thickness and growth rate values presented in Table 9.  The thickness and growth rate information indicates that the majority of growth in the thickness of the wake occurs at the upper slope, which has increasing slope values to go with the increasing diameter of rod in the crossflow. In the case of the lower slope, the two smaller diameter rods have zero growth rates, while the lower boundary of the wake downstream of the 1/4" diameter rod has a slightly positive slope, suggesting an upward movement, or lofting, of the wake as it moves downstream.

It should be noted that, as a result of interference from the erroneous contours from the bad pixels above X/D = 1.0, the velocity profiles in Figure 28 have only been plotted to just above Y = 40mm. The velocity profile shapes for each of the rods, at the two locations, are clearly visible in Figures 28 and 29, and at each location there are no significant differences between the shapes as a result of the different diameter rods, just slight differences in the normalized velocities.

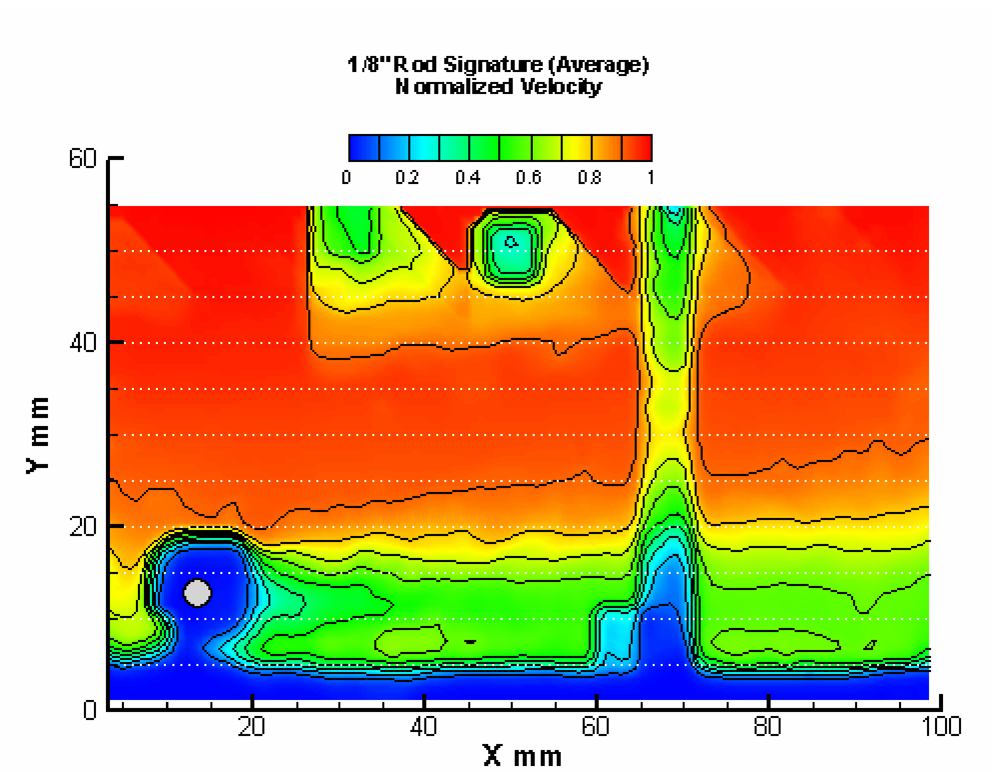


**Figure 25: Average velocity contours of 1/8" Rod at flow M = 0. 54.**

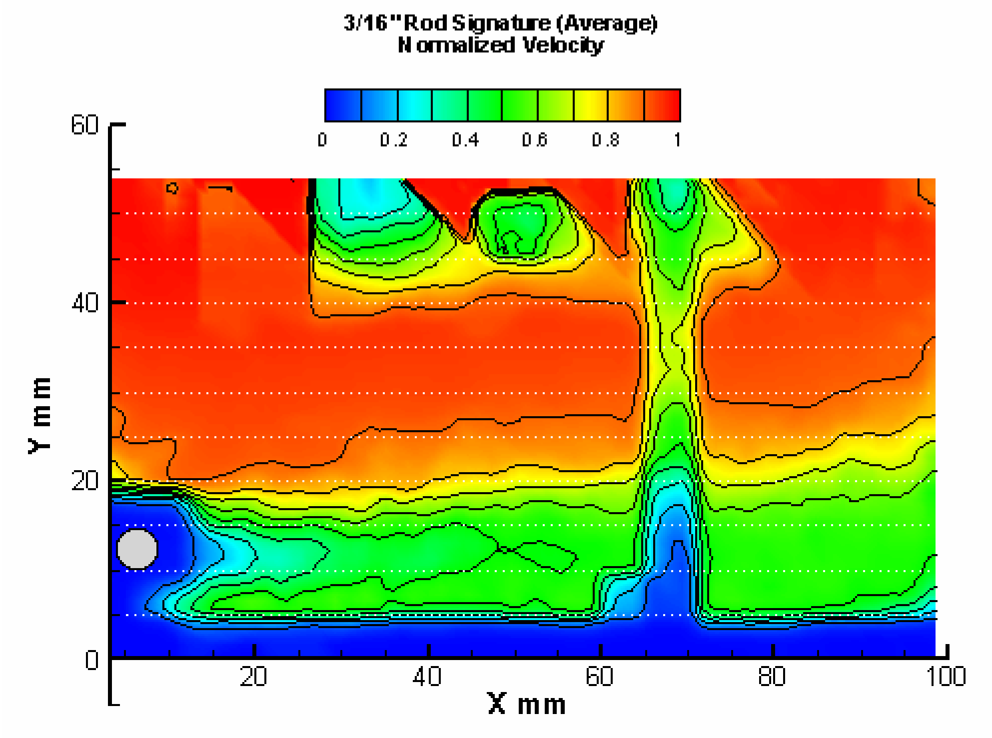


**Figure 26: Average velocity contours of 3/16" Rod at flow M = 0.57.**

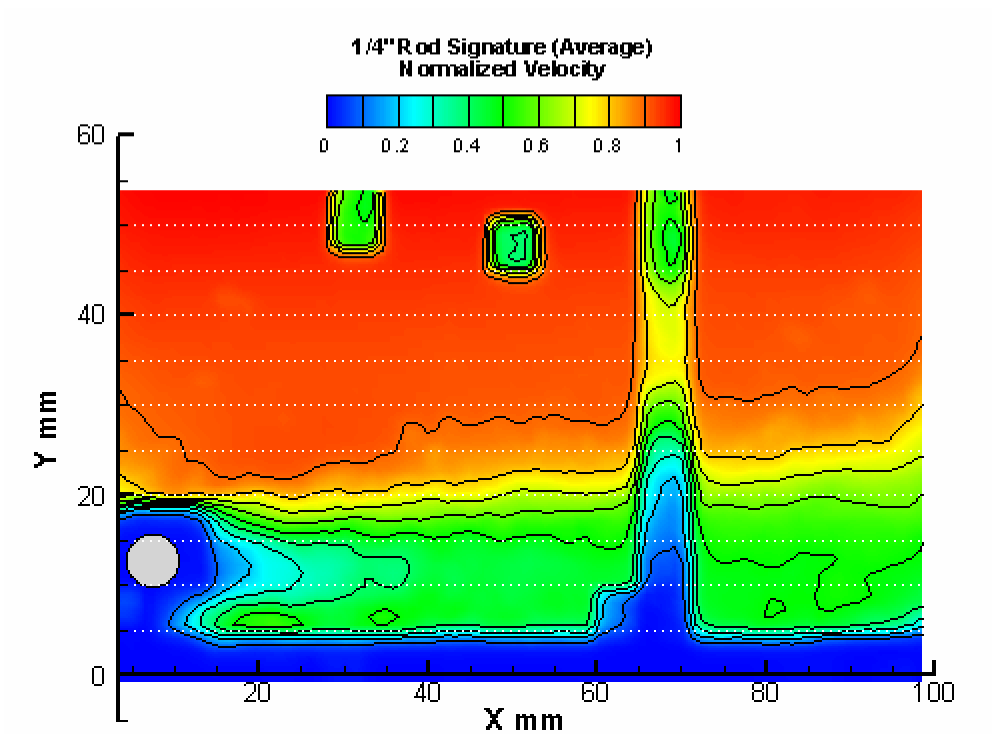


**Figure 27: Average velocity contours of 1/4" Rod at flow M = 0.50.**

**Table 9: Wake features of Phase 2 - Rod Signature configurations.**

| Rod Diameter Inches (mm) | Thickness at | | Growth Rate | |
|---|---|---|---|---|
| | X/D = 1.0 (mm) | X/D = 3.25 (mm) | Upper Slope (mm/mm) | Lower Slope (mm/mm) |
| 1/8" (3.175) | 16.29 | 23.78 | 0.131 | 0.000 |
| 3/16" (4.7625) | 18.73 | 28.53 | 0.172 | 0.000 |
| 1/4" (6.35) | 17.10 | 28.90 | 0.232 | 0.028 |

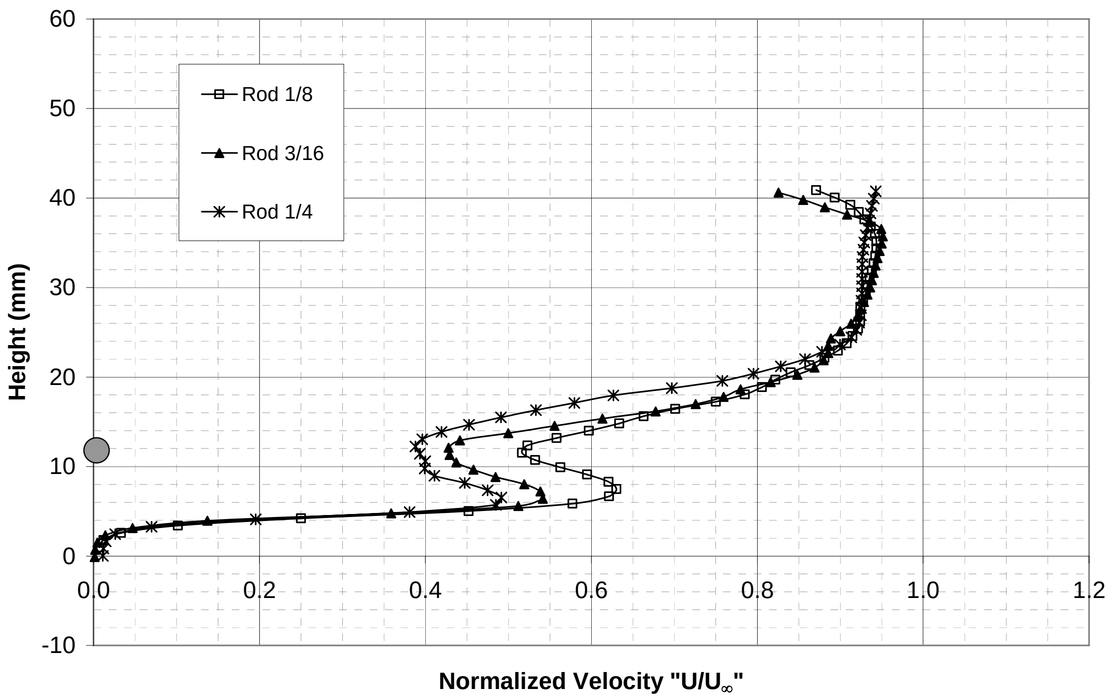


**Figure 28: Average Rod Signature Velocity Profiles at X/D = 1.0.**

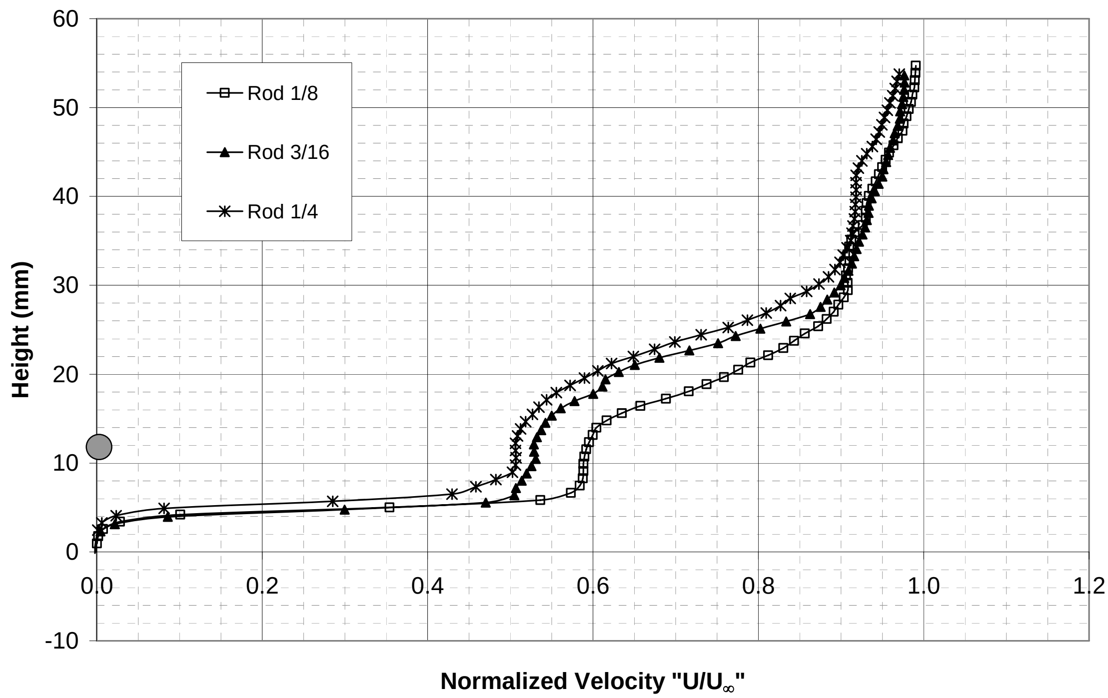


**Figure 29: Average Rod Signature Velocity Profiles at X/D = 3.25.**

The most significant difference in the overall shape of the velocity profiles occurs when moving from the forward location, X/D = 1.0, to the aft location, X/D = 3.25. As noted in the discussion of linear stability theory in Chapter 2, the asymmetric, “S” shape, velocity profiles at the X/D = 1.0 location, are highly unstable as a result of their two inflections points brought about by the velocity deficit downstream of the rod(s). However, as the flow develops and moves downstream to the X/D = 3.25 location, the flow velocities have recovered, and no inflection points are present in the profiles above Y = 5 mm, making them similar to the profile of Figure 4 (d), and as such, possibly unstable.

That concludes the presentation of the normalized velocity measurements, and attention now turns to the vorticity produced as a result of the vortices being shed from each of the rods. Ignoring the vorticity contours above Y = 30 mm, resulting from the inoperative pixels, and Figures 30, 31, and 32, clearly highlight both the regions, and intensity, of clockwise (negative/blue) and counter-clockwise vorticity (positive/yellow) downstream of the rods. As with all of the other flow field figures presented thus far, these too show the effects of the low kinetic energy flow below Y = 5 mm. The addition of the contour lines appear to make the thickness of the vorticity layer larger, but this is only a result of the validation process where the smoothing process has tried to give a more realistic transition to the large velocity gradient that was present in the unvalidated vector files.

A qualitative comparison of the vorticity regions downstream of the three different diameter rods suggests that overall there is a greater amount of vorticity present in the wakes downstream of the two larger rods, as compared to the regions of vorticity in the wake downstream of the 1/8" diameter rod.

From the contour maps alone, it was not possible to make a quantitative assessment of the differences from one figure to the next. One feature that is recognizable has similar features to the wake thickness and growth rates presented in

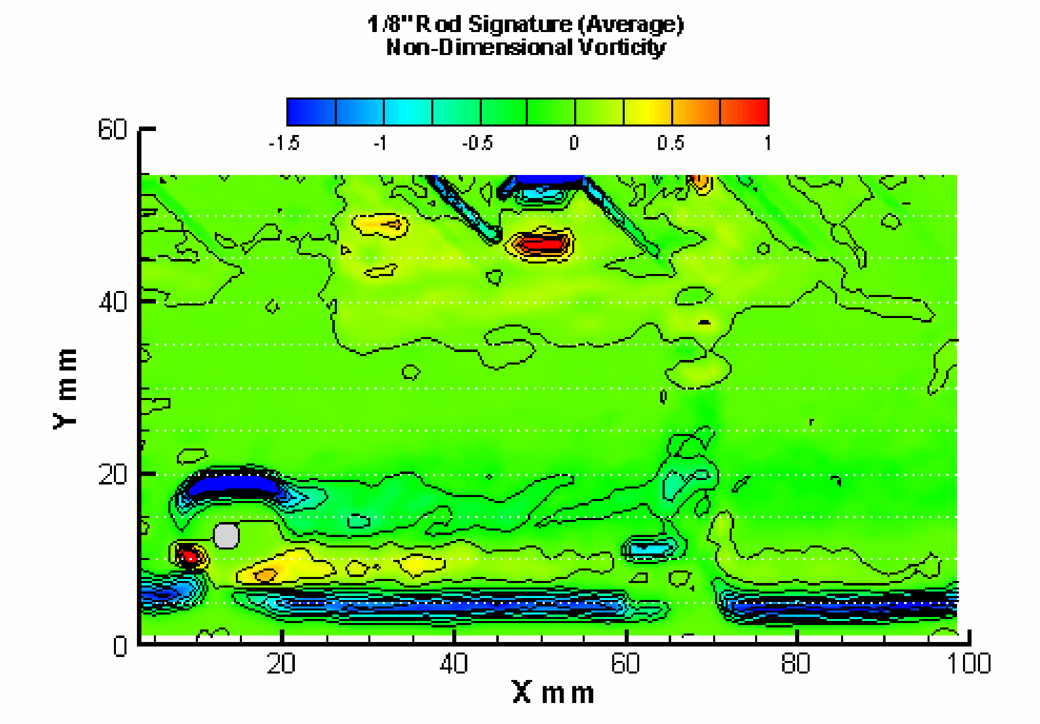


**Figure 30: Average vorticity contours of 1/8" Rod at flow M = 0.54.**

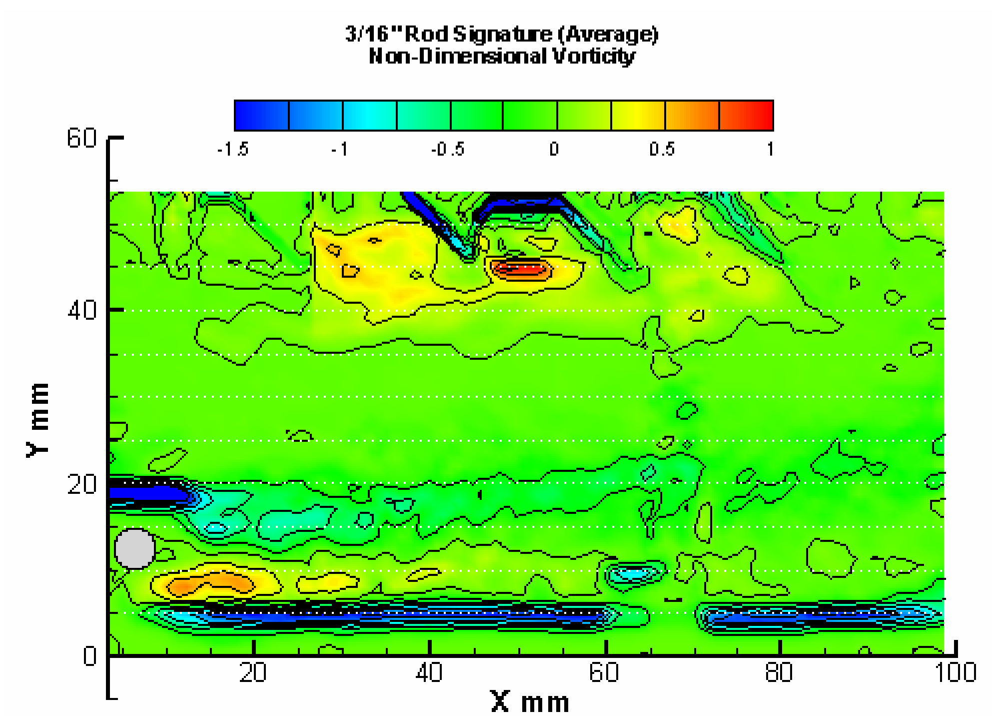


**Figure 31: Average vorticity contours of 3/16" Rod at flow M = 0.57.**

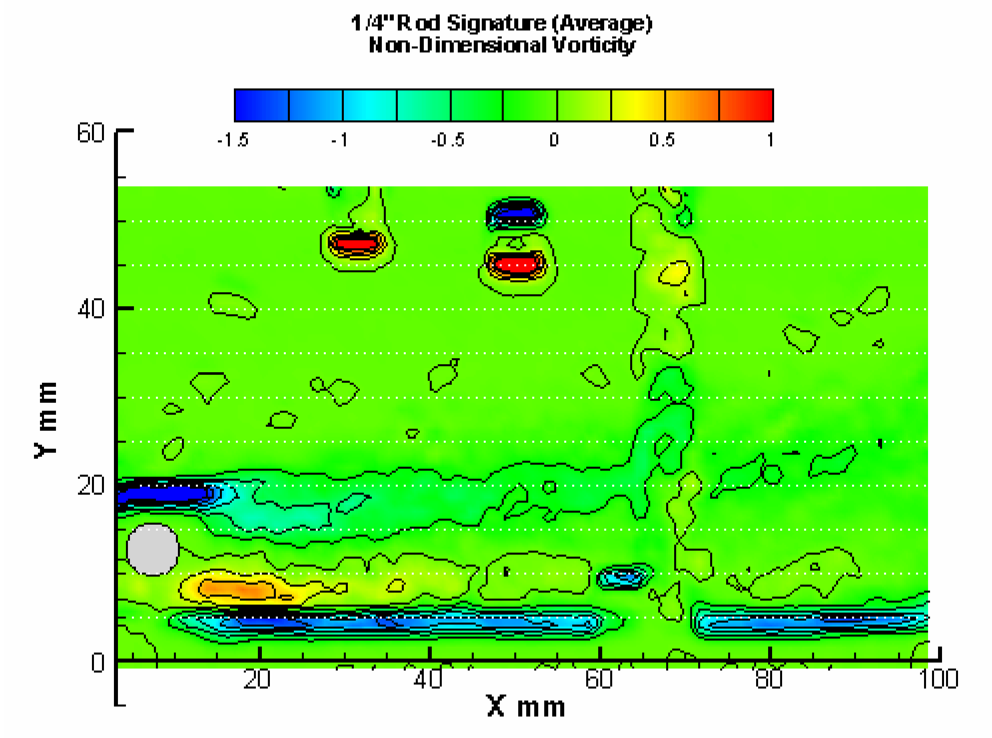


**Figure 32: Average vorticity contours of 1/4" Rod at flow M = 0.50.**

Table 9, which reflected increasing values with increasing diameter of rods. Being careful not to include the bad pixel effects above X = 69 mm, a comparison of the negative regions of vorticity being shed from the upper half of each rod also indicates that the vorticity, like the wake, is tending to move, grow, or be lofted, upward as it travels downstream of the rod.

In addition to the averaged non-dimensional vorticity contour images shown in Figures 30 through 32, six instantaneous snapshots of the vorticity from each of the three different flow fields are presented in Figures 33, 34, and 35. The images are not in any particular sequence or phase, and were chosen only to illustrate the features and dynamic nature of the wake downstream of the different Rod Signature configurations. One interesting feature to compare across the image sets is the effect that the shedding wake had on the predominantly coherent vorticity layer at X = 5 mm. These instantaneous images indicate that the shedding from the rods was able to affect the region of low kinetic energy. Figure 34 (a) and Figure 35 (f), are two of the images in particular that show the otherwise coherent vorticity layer near the floor being almost completely diffused, or mixed, amongst all of the other vorticity in the flow field.

Figure 35, marks the end of the Phase 2 Rod Signature velocity and vorticity results. The main points to be taken from this part of the discussion are the characteristic features identified in the Rod Signature average velocity and vorticity flow fields. In particular, following a similar discussion of Phase 3 and 4 data, it will be possible to compare the wake thickness and growth rate values outlined in Table 9 with those determined from the three different Cavity + Rod configurations.

The basis of the velocity and vorticity features of the Clean Tunnel and Rod Signature configurations were identified in the Phase 1 and Phase 2 results above, and the flow visualization results from the configurations of primary interest to this cavity flow study will now be reviewed.

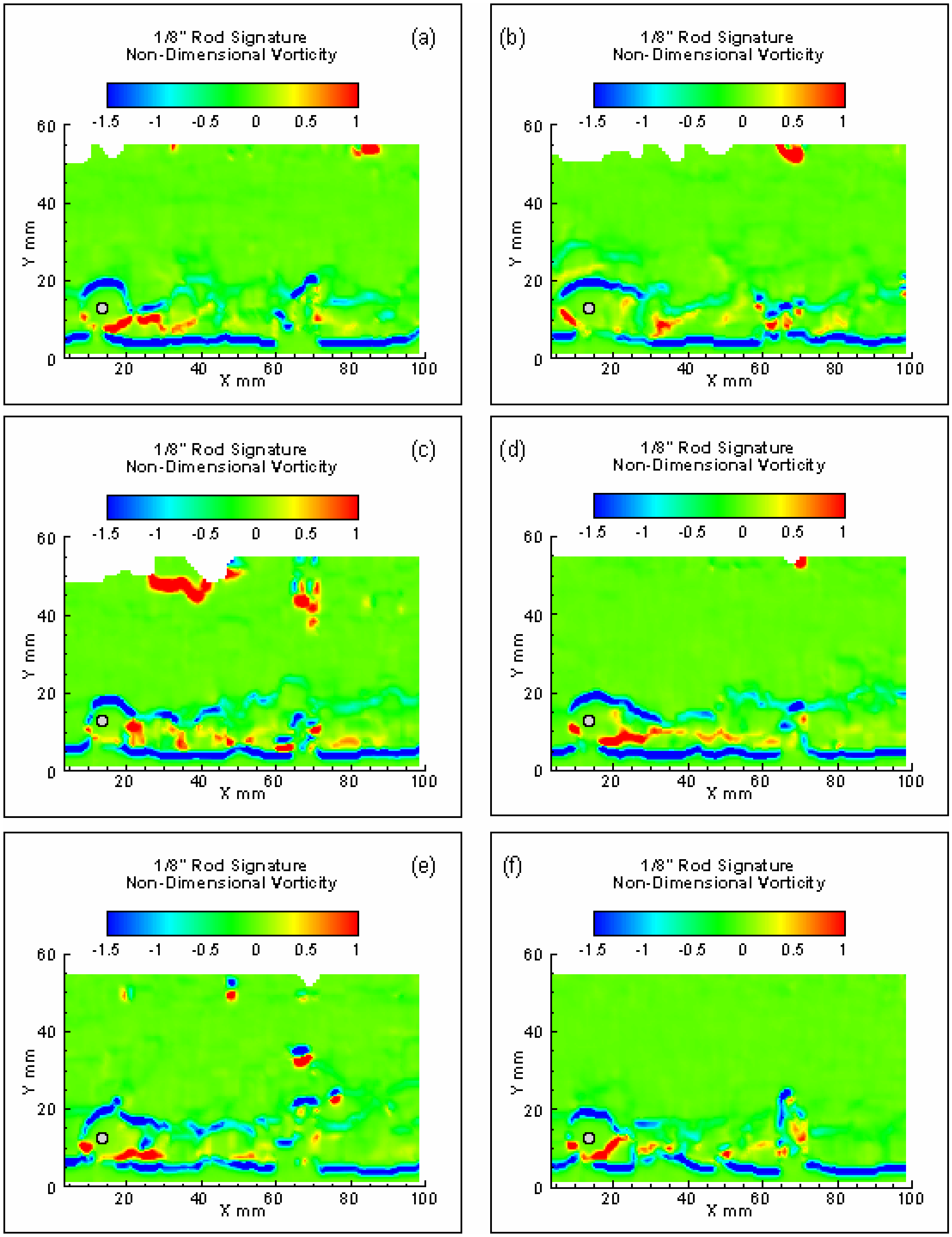


**Figure 33: Instantaneous vorticity contours of 1/8" Rod at average flow M = 0.54.**

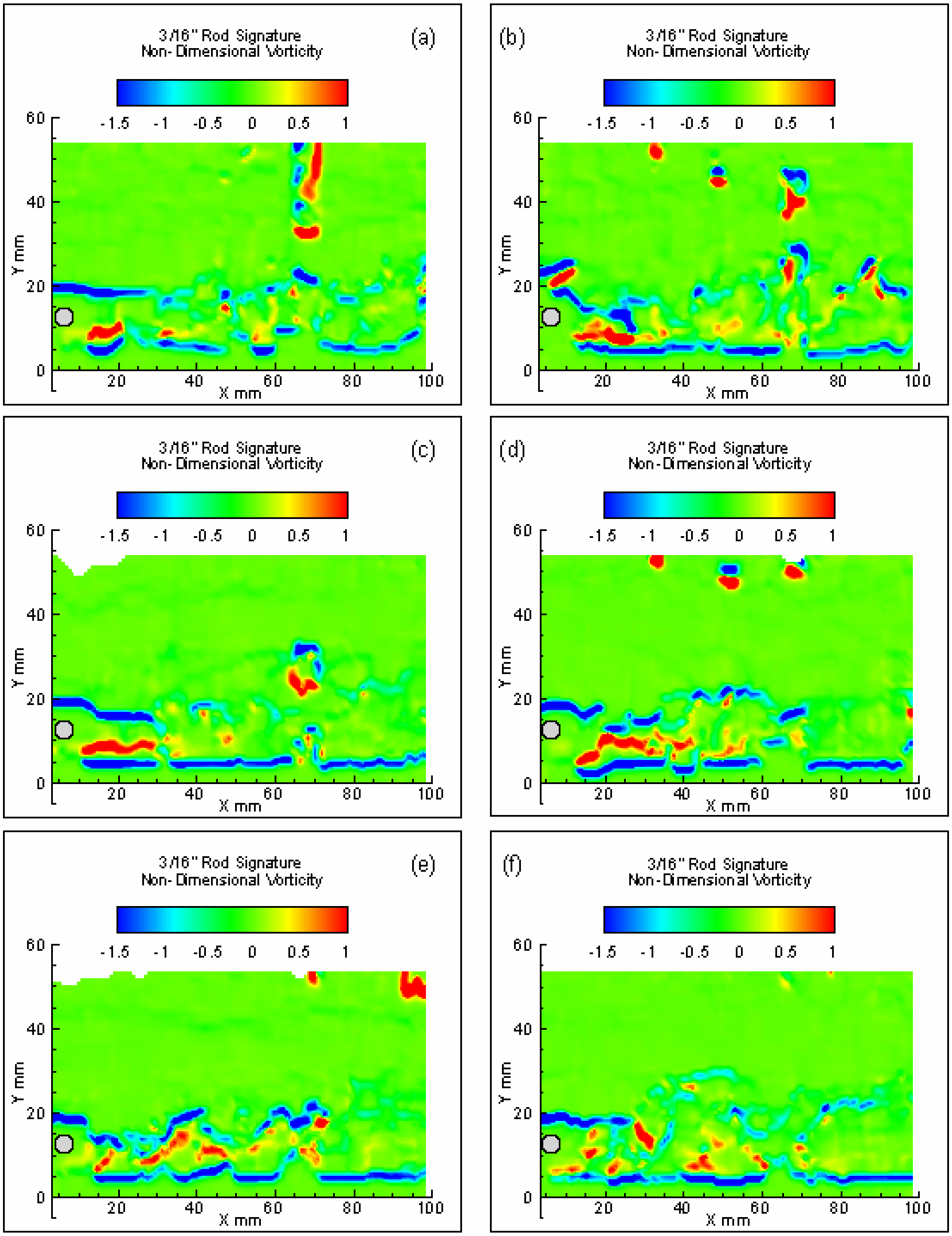


**Figure 34: Instantaneous vorticity contours of 3/16" Rod at average flow M = 0.57.**

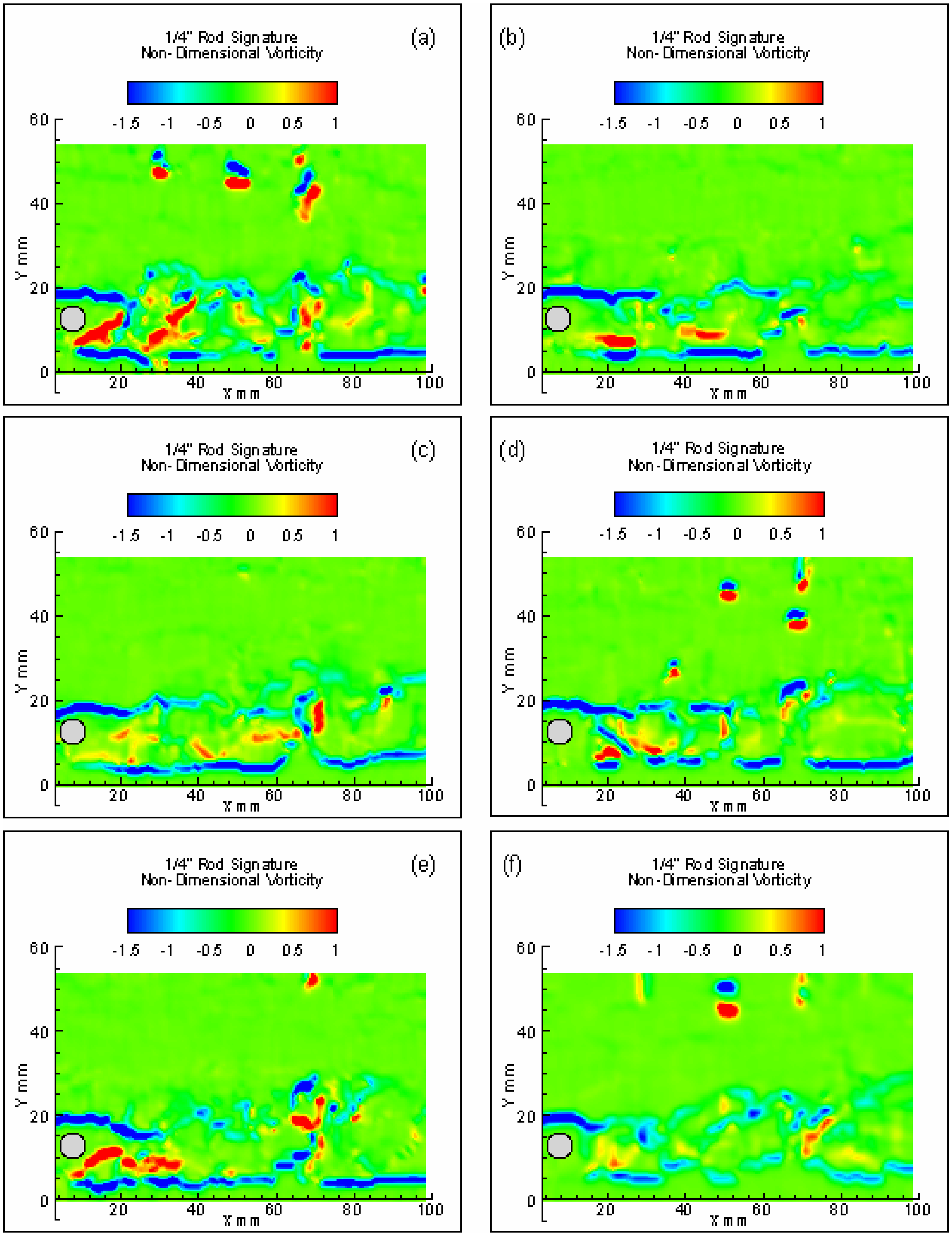


**Figure 35: Instantaneous vorticity contours of 1/4" Rod at average flow M = 0.50.**

Starting with the Baseline, cavity only, configuration, Figure 36 contains the normalized velocity contours for an L/D = 3.5 cavity, in an average Mach number flow of 0.51. Once again, the effects of the inoperative pixels detract from the important features of the main flow field and should be ignored. Evidenced by the light blue velocity contours at the front of the cavity, the region of low kinetic energy flow drops down off the leading edge of the cavity, and from the light blue contours that can be seen below Y = 0 mm, there are small regions of accelerated flow present within the cavity. Despite the region of low kinetic energy flow that has been seen to persist in each one of the flow field images, these velocity features, along with the vorticity features at the rear of the cavity in Figure 37, are indicative of the cavity shear layer interactions that resulted in the 148.7 dB SPL resonant acoustic tones presented in the Spectral data results.

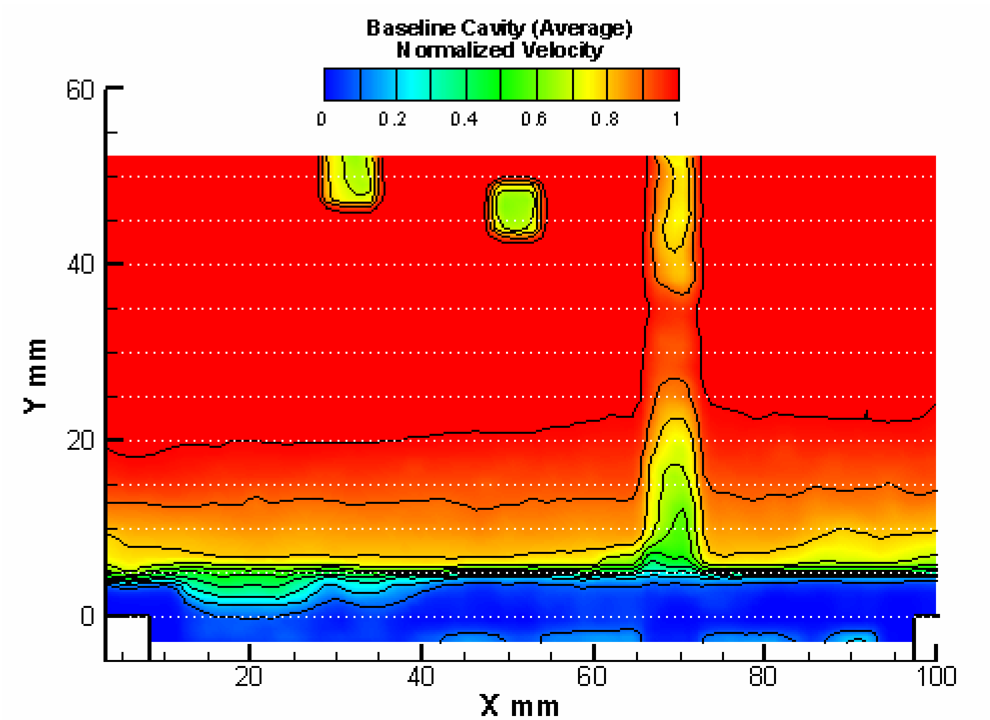


**Figure 36: Average Baseline velocity contours over L/D = 3.5 cavity at flow M = 0.51.**

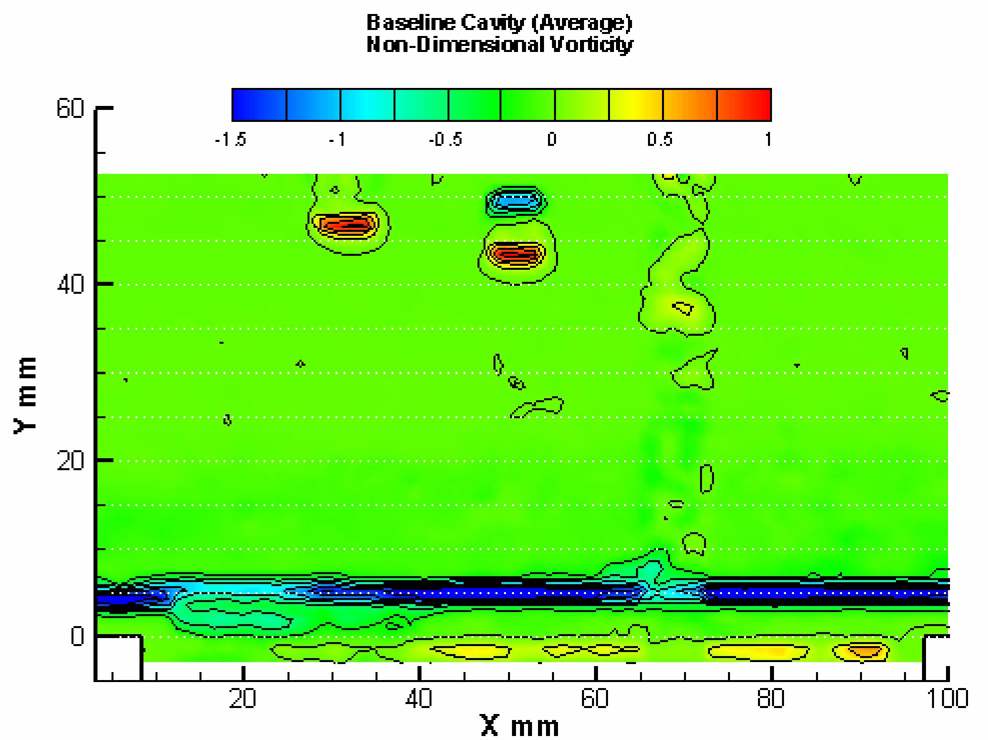


**Figure 37: Average Baseline vorticity contours over L/D = 3.5 cavity at flow M = 0.51.**

The very tight contour lines visible in Figures 36 and 37 at Y = 5 mm are further evidence of the dramatic velocity and vorticity gradients that appear in the flow field as a result of the undesirable flow conditions resulting from the use of the supersonic nozzle to conduct subsonic tests. Even with the cavity in place, Figure 37 shows that the vorticity layer remains stable, coherent, and bridges the full length of the cavity. In would be expected that if this inherent feature of the tunnel operation could be eliminated, the cavity would experience greater shear layer interactions and the amplitude of the resonant tones would be even greater.

For interest, instantaneous snapshots of the Baseline vorticity flow field are provided in Figure 38. The six images, Figure 38 (a) through (f) do show that there is some oscillation of the vorticity layer above the cavity, and they also give a better indication of the strength of the vorticity structures that occur near the rear of the cavity where the shear layer impinges upon the trailing edge.

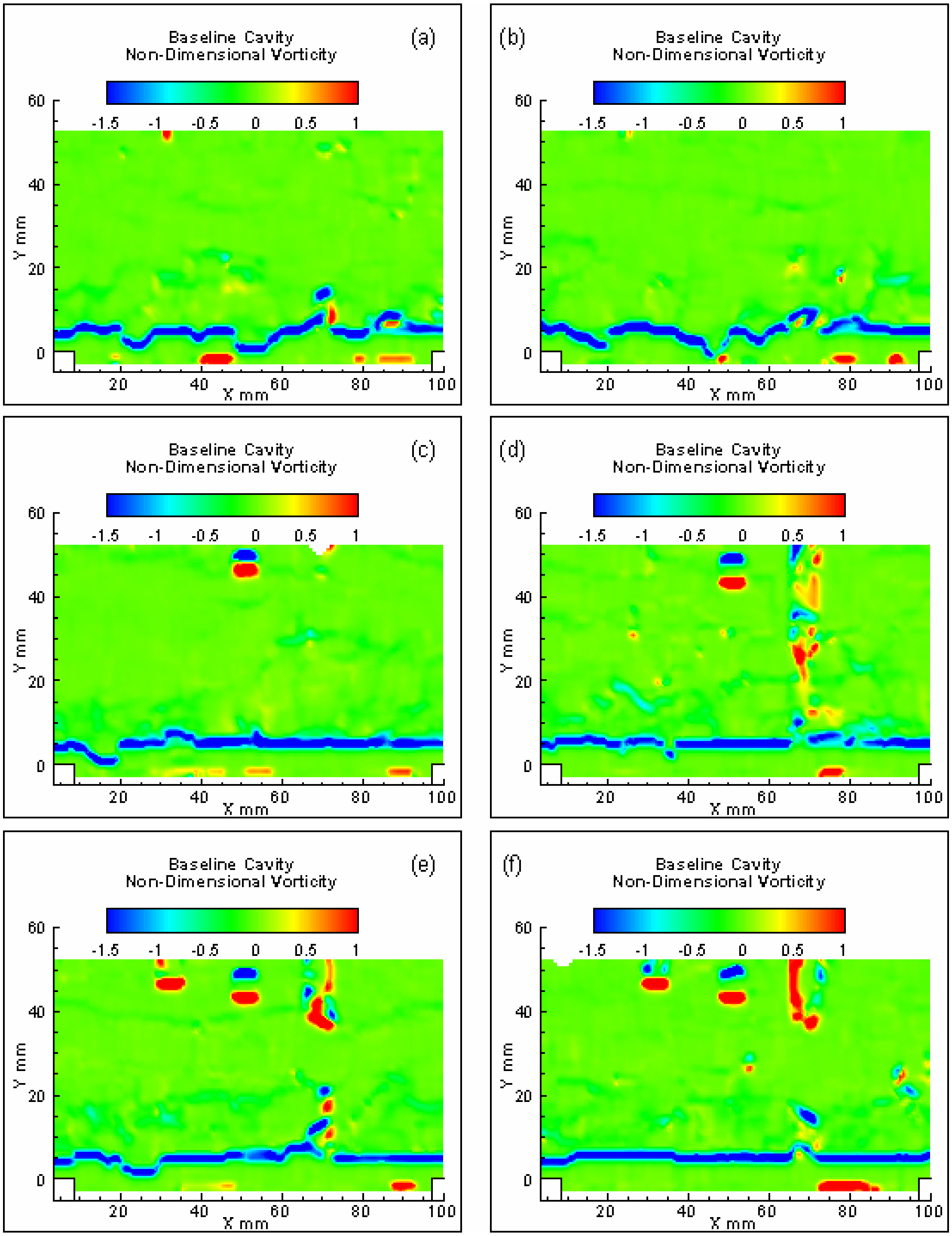


**Figure 38: Instantaneous vorticity contours over a L/D = 3.5 cavity with average flow M = 0.51.**

With the Baseline cavity features depicted in Figures 36 through 38, the Phase 4, Cavity + Rod results are expected to provide evidence of how the different diameter rods in crossflow affect the cavity shear layer interactions. The analysis of these Cavity + Rod configurations will follow a similar pattern to the Rod Signature discussion, focusing on the three specific features of the normalized velocity flow field at two locations, X/D = 1.0 and X/D = 3.25, downstream from the leading edge of the cavity: 1) the vertical position of the greatest velocity deficit; 2) the thickness of the wake; and 3) the shape of the velocity profile.

Figures 39 through 42 show that the greatest velocity deficit at downstream location X/D = 1.0, remains parallel to the rod center at a vertical location between 12 and 13 mm, similar to the deficit behind the Rod only configuration. As with the Phase 2 results, ignoring the vertical contours above X = 69 mm, the velocity has recovered and there is no longer a velocity deficit at the X/D = 3.25 location. However, in this configuration, instead of the profile being vertical and velocity remaining constant from Y = 9 to 12 mm as was the case in Figure 29, Figure 43 indicates that the three Cavity + Rod velocity profiles each have a positive slope and the mean flow velocity begins increasing above Y = 8 mm. For comparison purposes, the averaged Baseline velocity profile has been plotted alongside the averaged Cavity + Rod velocity profiles in Figures 42 and 43, and will be discussed in the analysis of feature 3).

In examining the second feature of wake thickness, a comparison of the velocity contours in Figures 39, 40, and 41, show similar characteristics to those from Phase 2. Looking for combined effects between the presence of the cavity and the rod wakes, a closer analysis of Figure 42, using the inflection point and normalized velocity of 0.9 criteria already described for the lower and upper boundary, should help to more clearly described any wake thickness or growth rate differences. In addition to the Phase 4, Cavity + Rod, wake thickness and growth rate values determined from the vector data used to plot the velocity profiles at the two downstream locations, Table 10 also repeats the Phase 2 values from Table 9 for comparison.

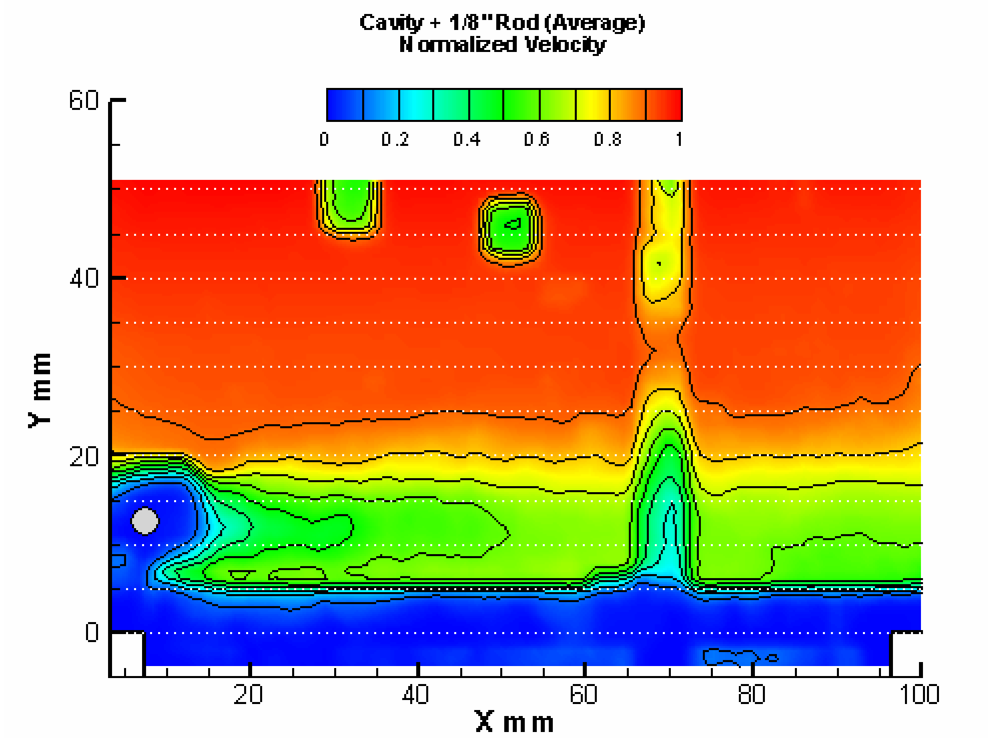


**Figure 39: Average velocity contours of Cavity + 1/8" Rod at flow M = 0.49.**

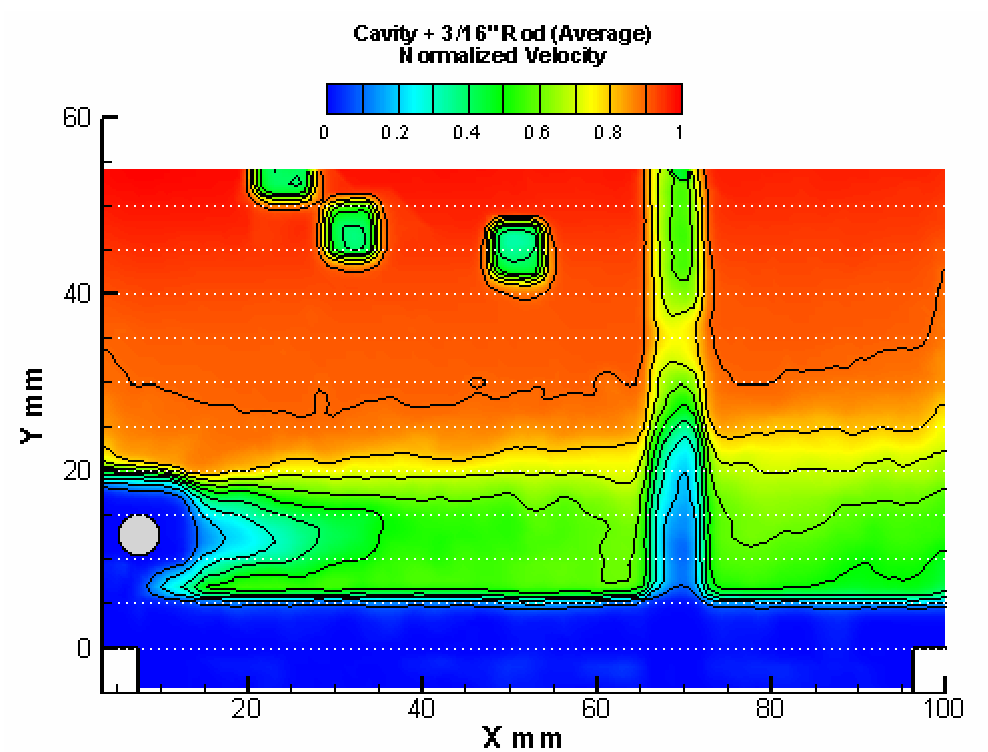


**Figure 40: Average velocity contours of Cavity + 3/16" Rod at flow M = 0.51.**

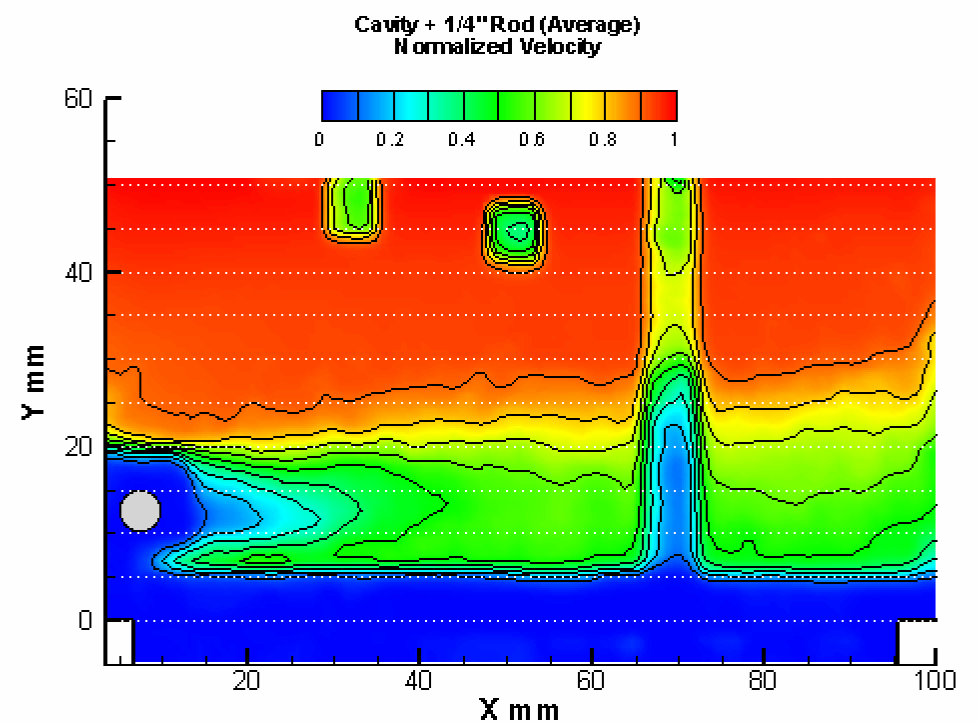


Figure 41: Average velocity contours of Cavity + 1/4" Rod at flow M = 0.50.

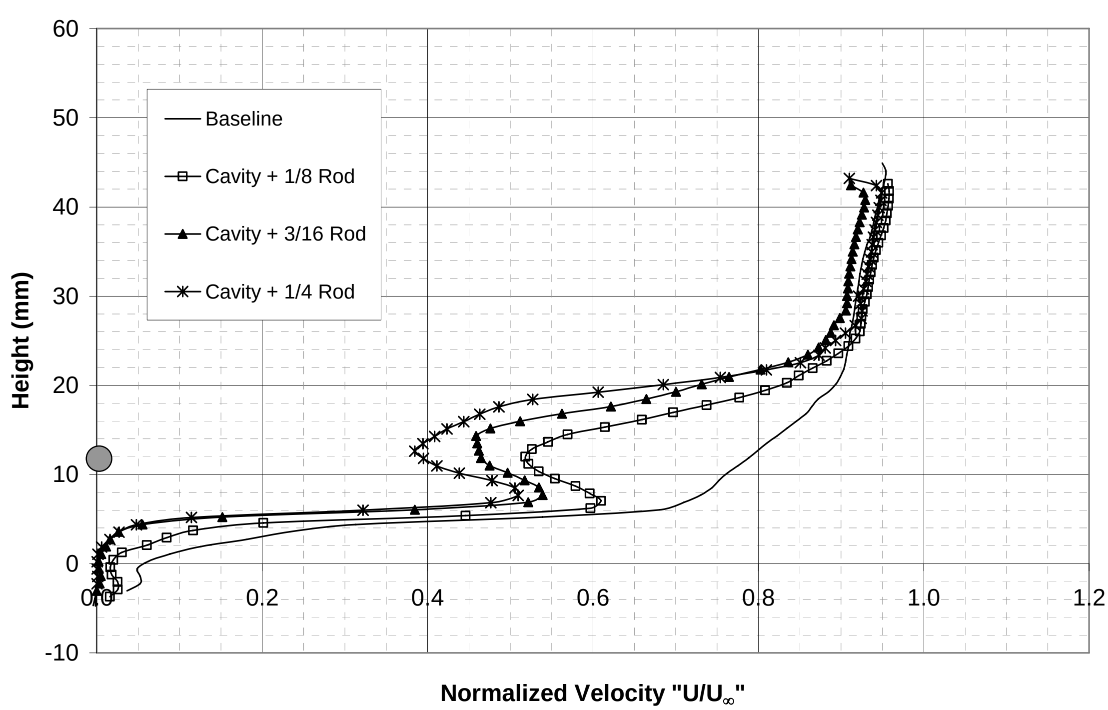


Figure 42: Average Cavity + Rod velocity profiles at X/D = 1.0.

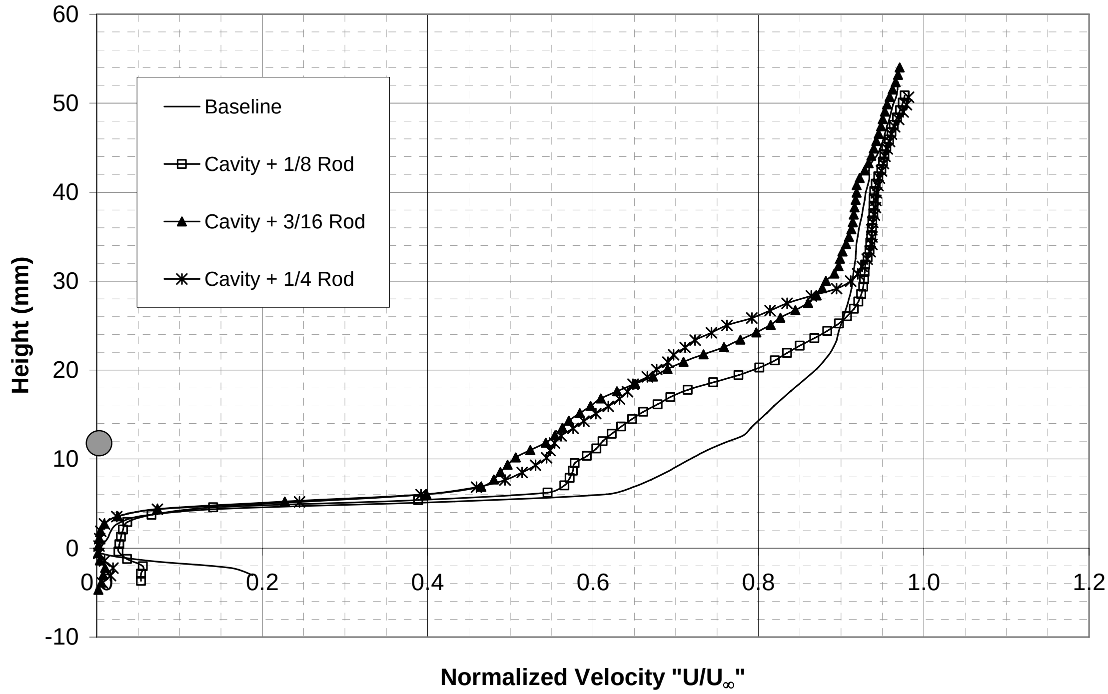


**Figure 43: Average Cavity + Rod velocity profiles at X/D = 3.25.**

**Table 10: Comparison of wake features from Phase 4 and Phase 2.**

| Rod Diameter Inches (mm) | Thickness at | | Growth Rate | |
|---|---|---|---|---|
| | X/D = 1.0 (mm) | X/D = 3.25 (mm) | Upper Slope (mm/mm) | Lower Slope (mm/mm) |
| 1/8" (3.175) | 17.36 | 17.36 | 0.029 | 0.029 |
| 3/16" (4.7625) | 20.67 | 23.15 | 0.087 | 0.043 |
| 1/4" (6.35) | 18.19 | 19.84 | 0.071 | 0.043 |
| **Repeat of Phase 2 - Rod Signature results for comparison** | | | | |
| 1/8" (3.175) | 16.29 | 23.78 | 0.131 | 0.000 |
| 3/16" (4.7625) | 18.73 | 28.53 | 0.172 | 0.000 |
| 1/4" (6.35) | 17.10 | 28.90 | 0.232 | 0.028 |

The wake thickness information contained in Table 10 is enlightening and from it, the following can be determined:

a) At X/D = 1.0, each of the Cavity + Rod configurations had a wake thickness between 1 to 2 mm greater than the without the presence of the cavity;

b) At X/D = 3.25, the thickness of the wake with the presence of the cavity was less than it was in Phase 2 without the cavity, except for the Cavity + 1/8" Rod value which remained constant; and

c) As a result of a) and b), the growth rate slope of the upper boundary was less for each of the Cavity + Rod configurations, on average, only 35 % of the complementary value with just the rod and no cavity; but

d) The other telling difference of the Phase 4 results appears in the growth rate of the lower boundary. In comparison to the Phase 2 results, where the lower boundary of the 1/8" and 3/16" rod wakes had a zero growth rate, and the lower boundary of the 1/4" rod wake had a growth rate with a positive slope, each of the three Cavity + Rod configurations exhibited a positive growth rate slope. These positive growth rate values indicate that the wake flow is gently being lofted upward.

The lower slope growth rate values listed in Table 10 are relatively small, but over the distance from X/D = 1.0 to the trailing edge at X/D = 3.5, the positive slope value of 0.043 mm/mm, for the 3/16" and 1/4" rods, translates into the lower edge of the wake being raised 2.7 mm higher at the critical trailing edge, than where it started.

The third feature of interest at each of the wake locations downstream of the rod, is the difference in shape of the velocity profile as the wake develops. As was the case in Phase 2, for the rod only velocity profile at X/D = 1.0, each velocity profile at X/D = 1.0

downstream of the Cavity + Rod(s) in crossflow, with its “S” shape resulting from the velocity deficit, is unstable as defined by linear stability theory. However, as the flow develops and moves back towards the trailing edge the profile recovers but remains potentially unstable as it resembles the profile of Figure 4(d).

One other interesting feature of the velocity profiles at the downstream location, X/D = 3.25, presented in Figure 43, is visible within the cavity below Y = 0 mm. Comparing the Baseline profile in this region to the 3/16" and 1/4" Cavity + Rod profiles, it is evident that average normalized velocity inside the cavity just ahead of the rear wall has been significantly reduced by the presence of the larger rods in crossflow. From $U/U_\infty = 0.19$ for the Baseline flow, down to less than $U/U_\infty = 0.002$ as a result of the 3/16" and 1/4" rods in crossflow.

The normalized velocity contour maps and averaged velocity profile plots of the Cavity + Rod configurations have revealed characteristics that suggest the shear layer is being lofted over the cavity and helping to minimize the effects of interactions occurring at the cavity trailing edge. Streamtraces are another analysis tool available within the Tecplot PIV Macro Panel, and the addition of 20 streamtraces, running tangent to the velocity vectors that make up the normalized velocity contour maps, offers more visual evidence of the lofting effect created by the addition of the rod(s) in crossflow.

To illustrate the point, streamtraces added to the average normalized velocity contour map of the Baseline configuration in Figure 44 highlight the interactions that occur between the cavity shear layer and the trailing edge. The streamtraces of Figure 45 show that the 1/8" Rod does provide some lifting of the flow field over the cavity, but as is known from the spectral data this configuration offered only minimal suppression of the peak amplitude cavity tone. Figures 46 and 47, on the hand, clearly visualize the lofting effect created by the 3/16" and 1/4" rods in crossflow and provide evidence of the mechanism that suppressed the peak amplitude tone by an average of 13.6 and 15.1 decibels respectively.

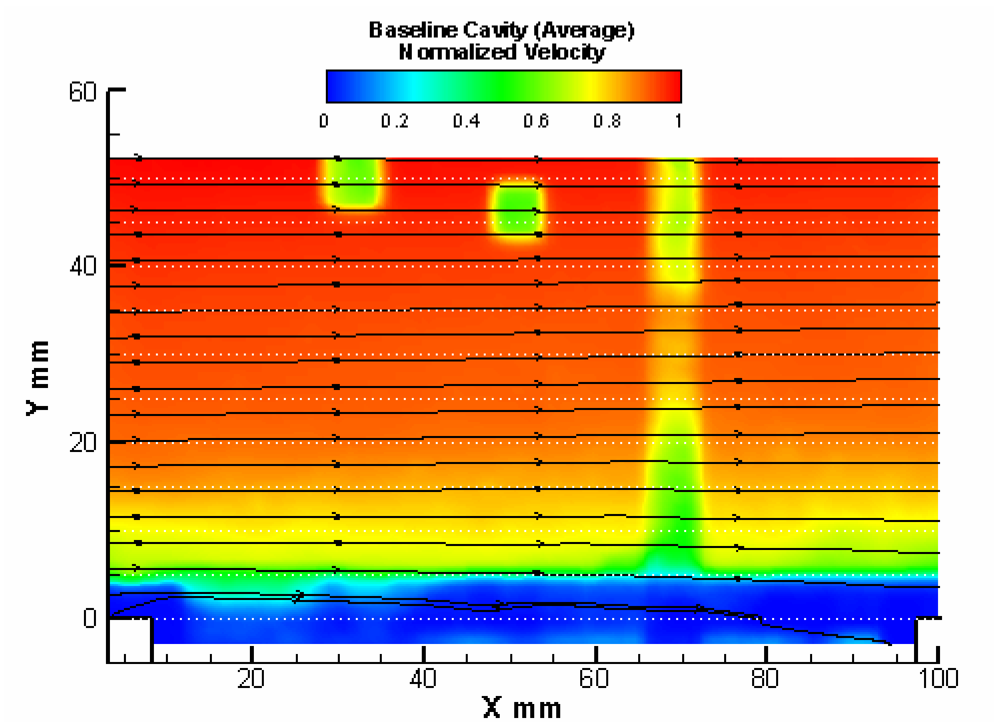


**Figure 44: Baseline velocity contours with streamtraces.**

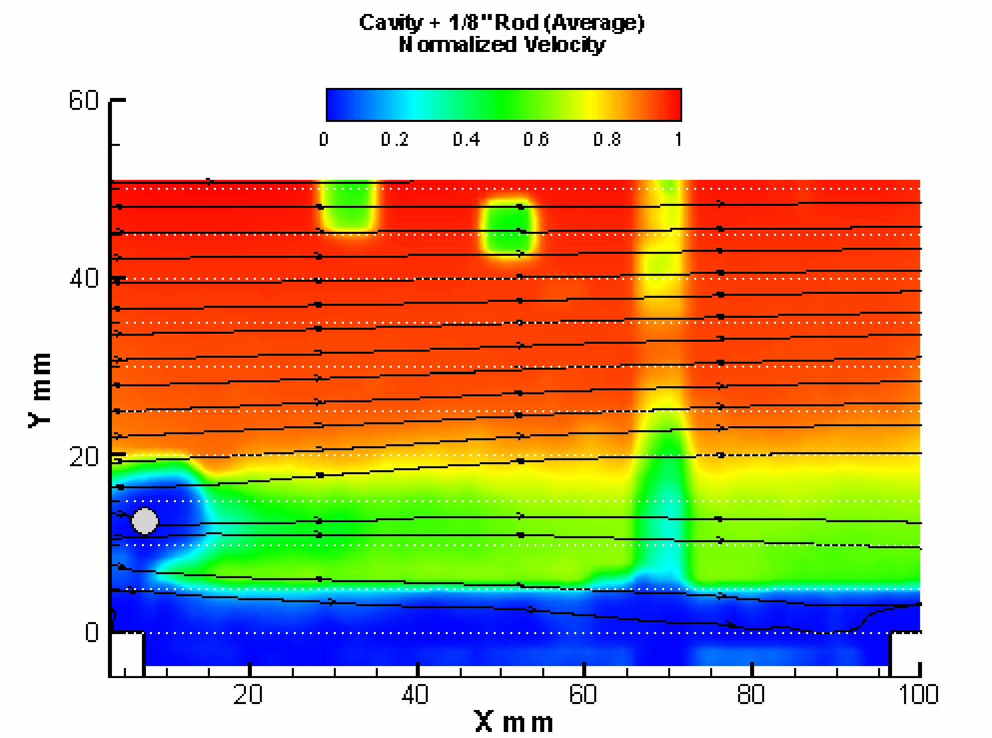


**Figure 45: Cavity + 1/8" Rod velocity contours with streamtraces.**

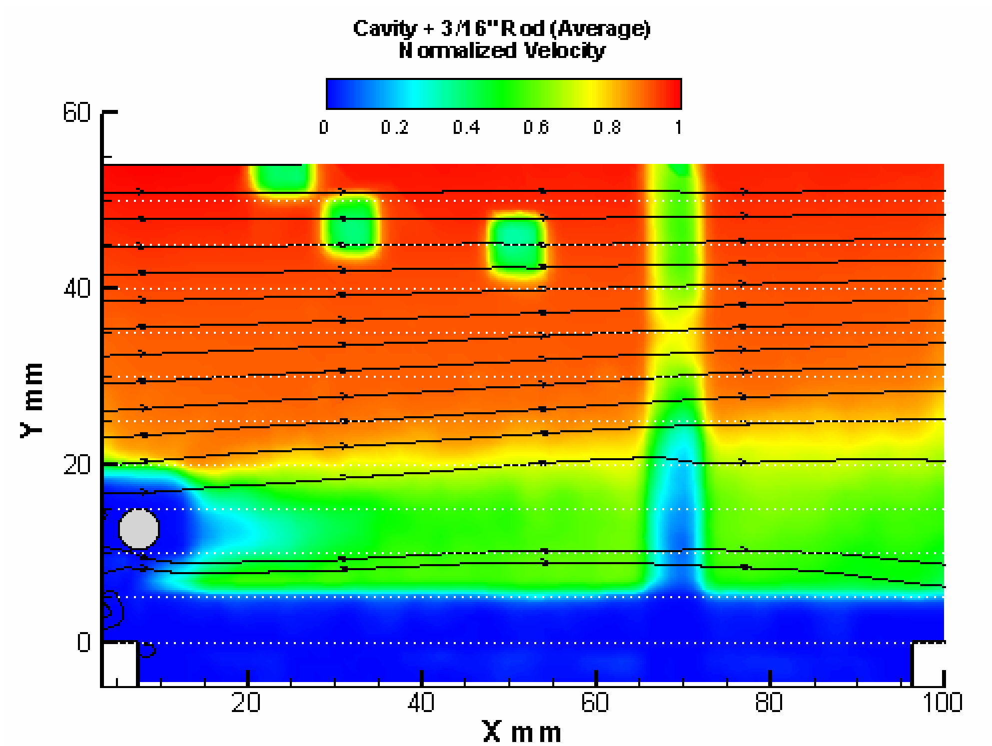


**Figure 46: Cavity + 3/16" Rod velocity contours with streamtraces.**

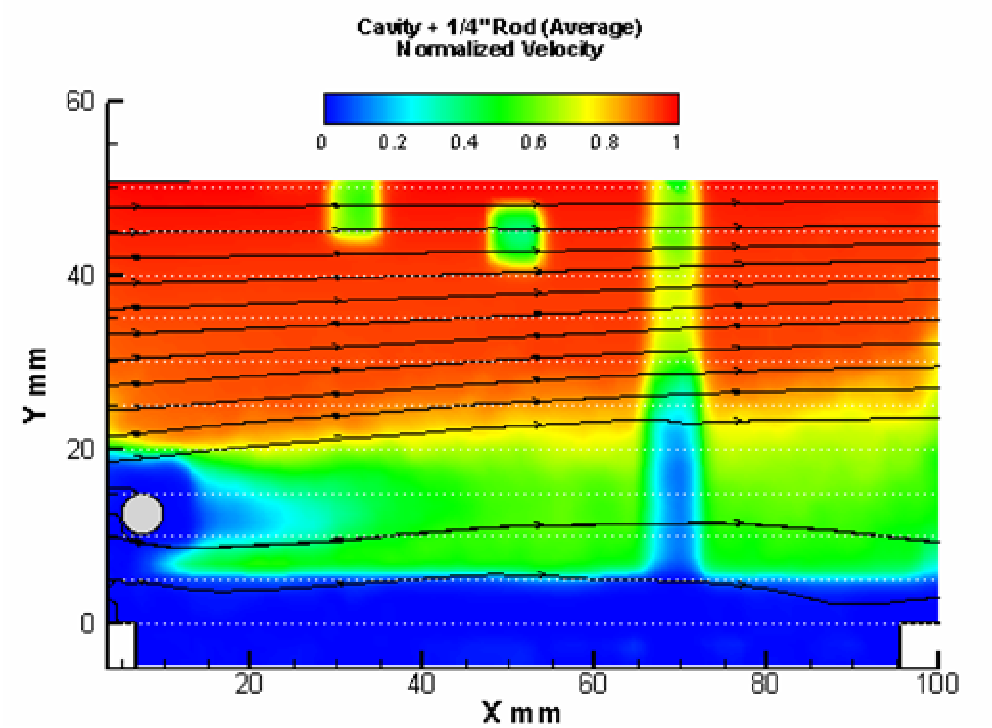


**Figure 47: Cavity + 1/4" Rod velocity contours with streamtraces.**

This effect of the rods to loft the shear layer and reduce the trailing edge interactions is also reflected in the averaged vorticity contour images contained in Figures 48, 49, and 50. In comparison to the Baseline vorticity contours of Figure 37, the reduction in the amount, and intensity, of the contour color levels in Figure 48, illustrates that the 1/8" rod in crossflow did offer some suppression of the shear layer interactions, but not to the same degree as the suppression afforded by the 3/16" and 1/4" rods depicted in Figures 49 and 50. Another feature of the vorticity contour images to take note of is the reduced intensity of the vorticity layer related to sharp velocity gradient toward the region of low kinetic energy flow. Recall it being mentioned in the analysis of the Baseline images, that this feature could hold some clues to the net effect of the rods in crossflow, and over the whole span of the vorticity layer the increasing diffusion of vorticity with increasing diameter rod is evident, but no where more clearly than in the 25 to 30 mm ahead of the trailing edge of each of the three images. From Figure 48 down through Figure 50, the contour lines become more spread out, and the intensity of the negative (blue) vorticity becomes less negative, and a lighter shade of blue.

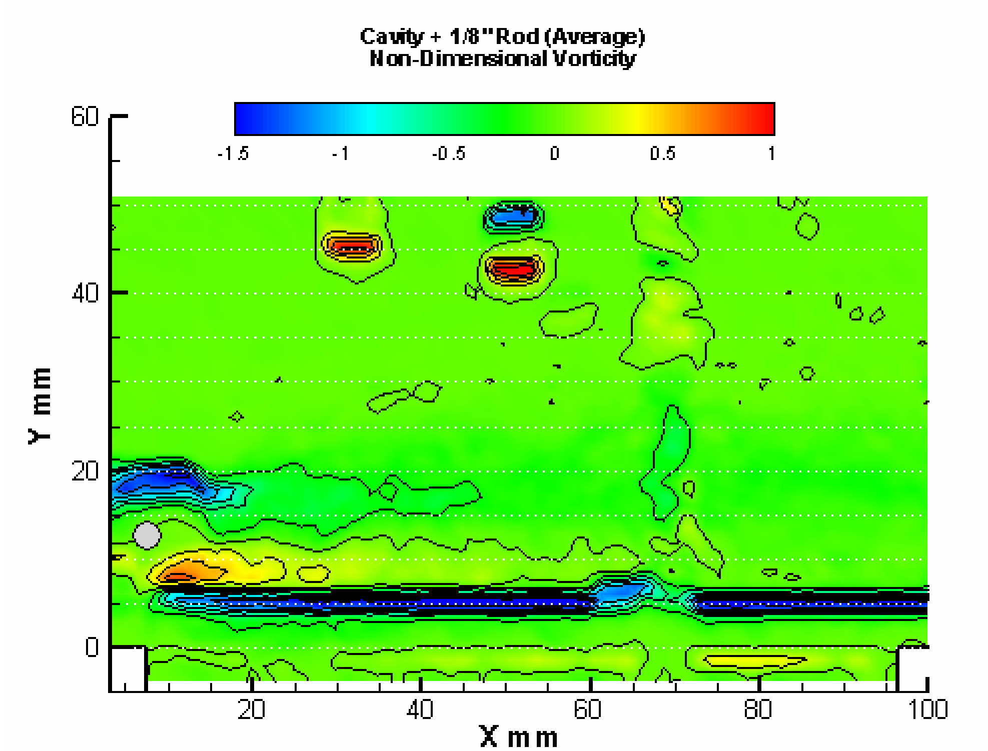


Figure 48: Average vorticity contours of Cavity + 1/8" Rod at flow M = 0.49.

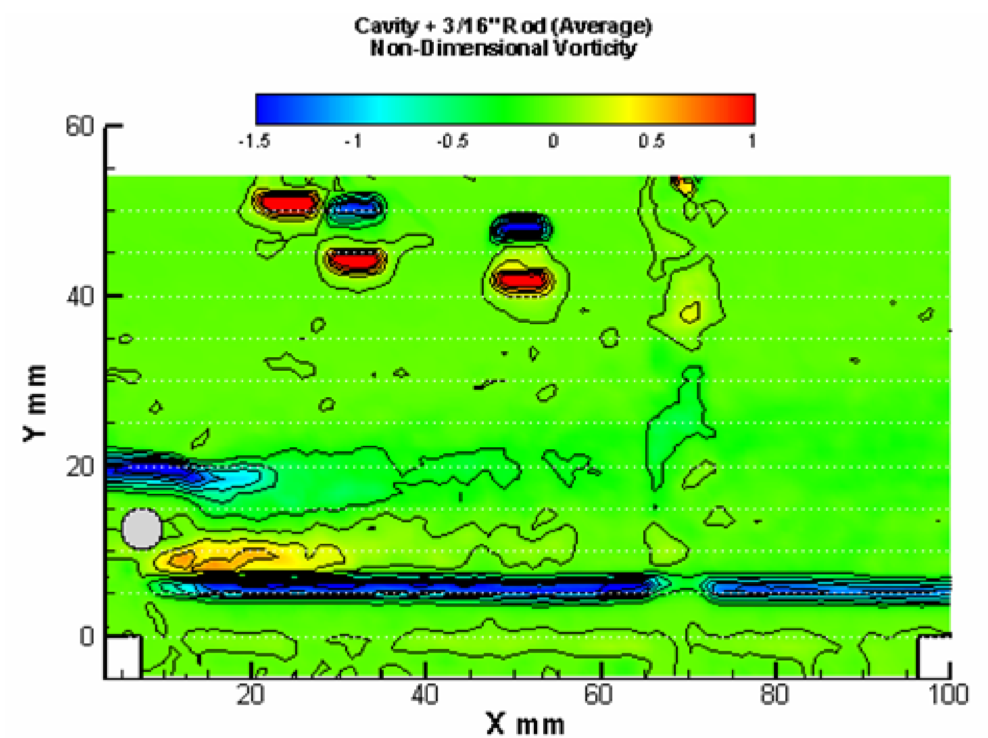


Figure 49: Average vorticity contours of Cavity + 3/16" Rod at flow M = 0.51.

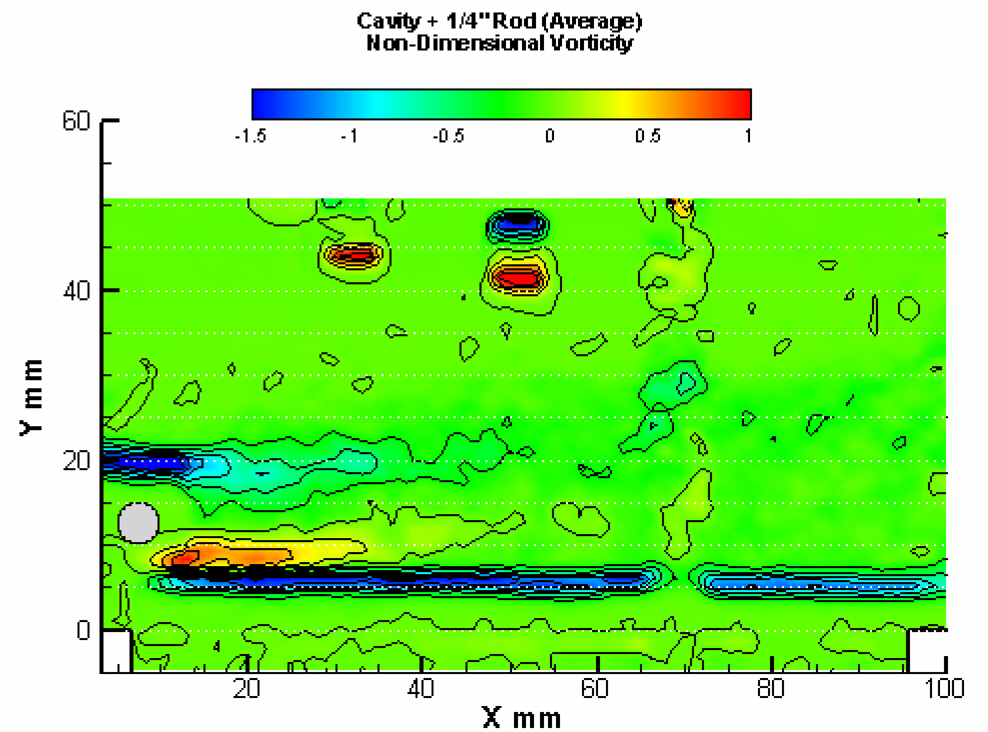


**Figure 50: Average vorticity contours of Cavity + 1/4" Rod at flow M = 0.50.**

To conclude the presentation of Flow Visualization data, snapshots of instantaneous vorticity contours for each of the Cavity + Rod configurations are provided in Figures 51, 52, and 53. As noted earlier, although they are not necessarily sequential, or in any particular phase, they are representative of the distribution of vorticity as a result of putting the different diameter rods in crossflow above the leading edge of the cavity. A comparative look across the three image sets for the effect of the rod on both the vorticity layer at Y = 5 mm, and the presence of vorticity within the cavity near the trailing edge, adds to illustrate the differences noted in the averaged contour maps presented above.

The four analysis methods just described, velocity contours, velocity profiles, streamtraces, and vorticity contours, each offer a different, but complementary, perspective of the shear layer effects created by the introduction of different diameter rods in crossflow above the cavity leading edge. These flow visualization results together with the frequency spectra results present a complete response to the primary objectives of thesis work.

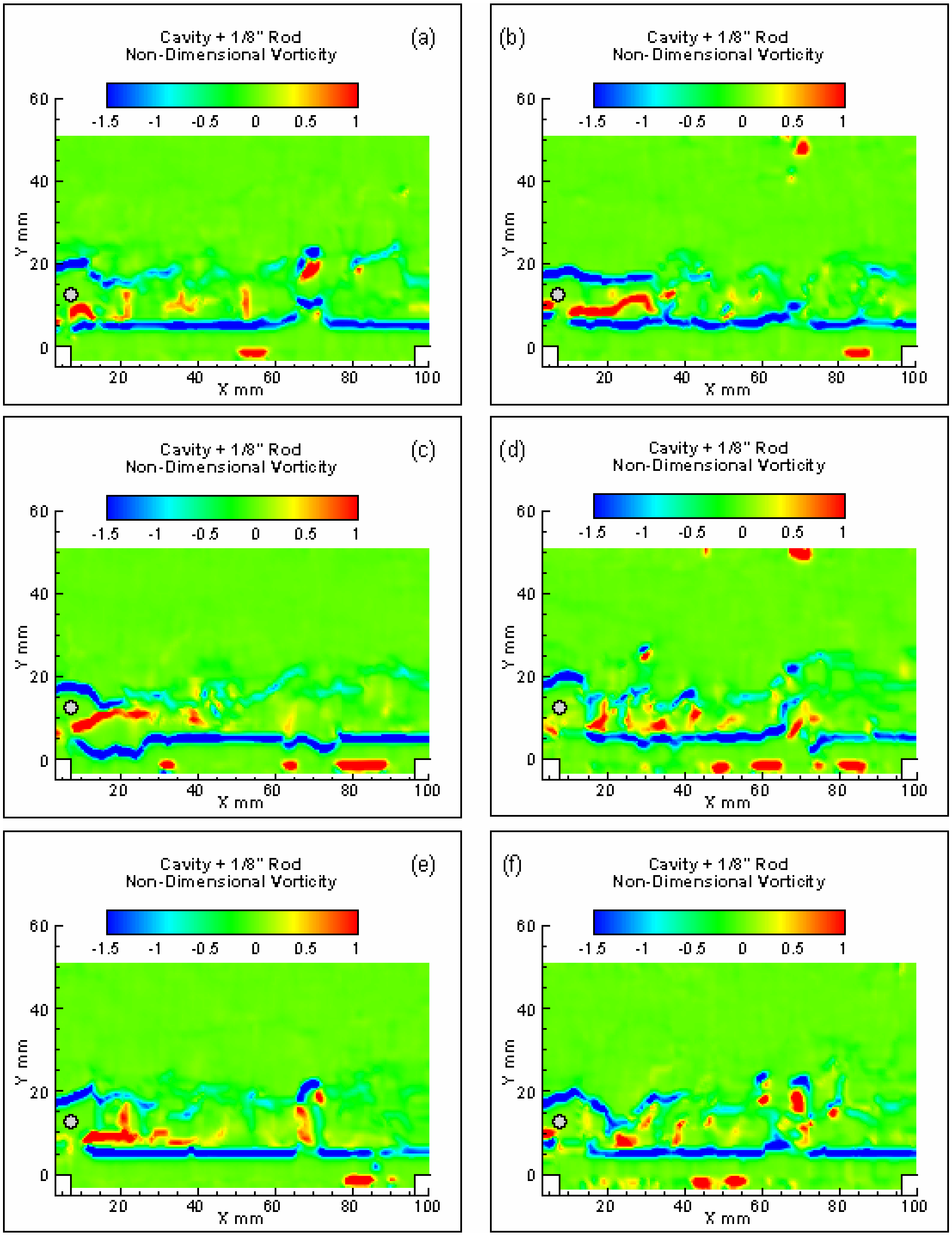


**Figure 51: Instantaneous vorticity contours of Cavity + 1/8"Rod at flow M = 0.49.**

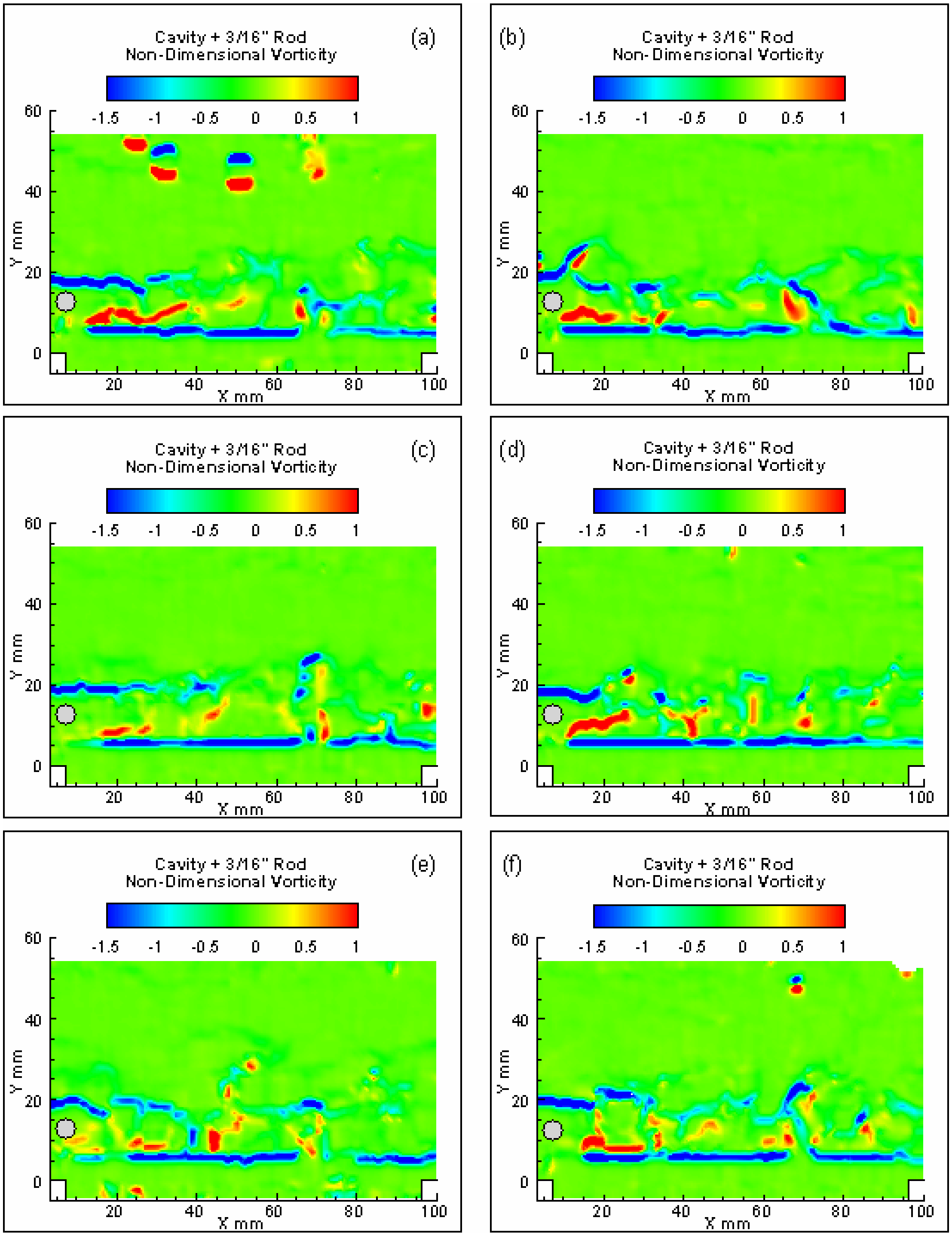


**Figure 52: Instantaneous vorticity contours of Cavity + 3/16"Rod at flow M = 0.51.**

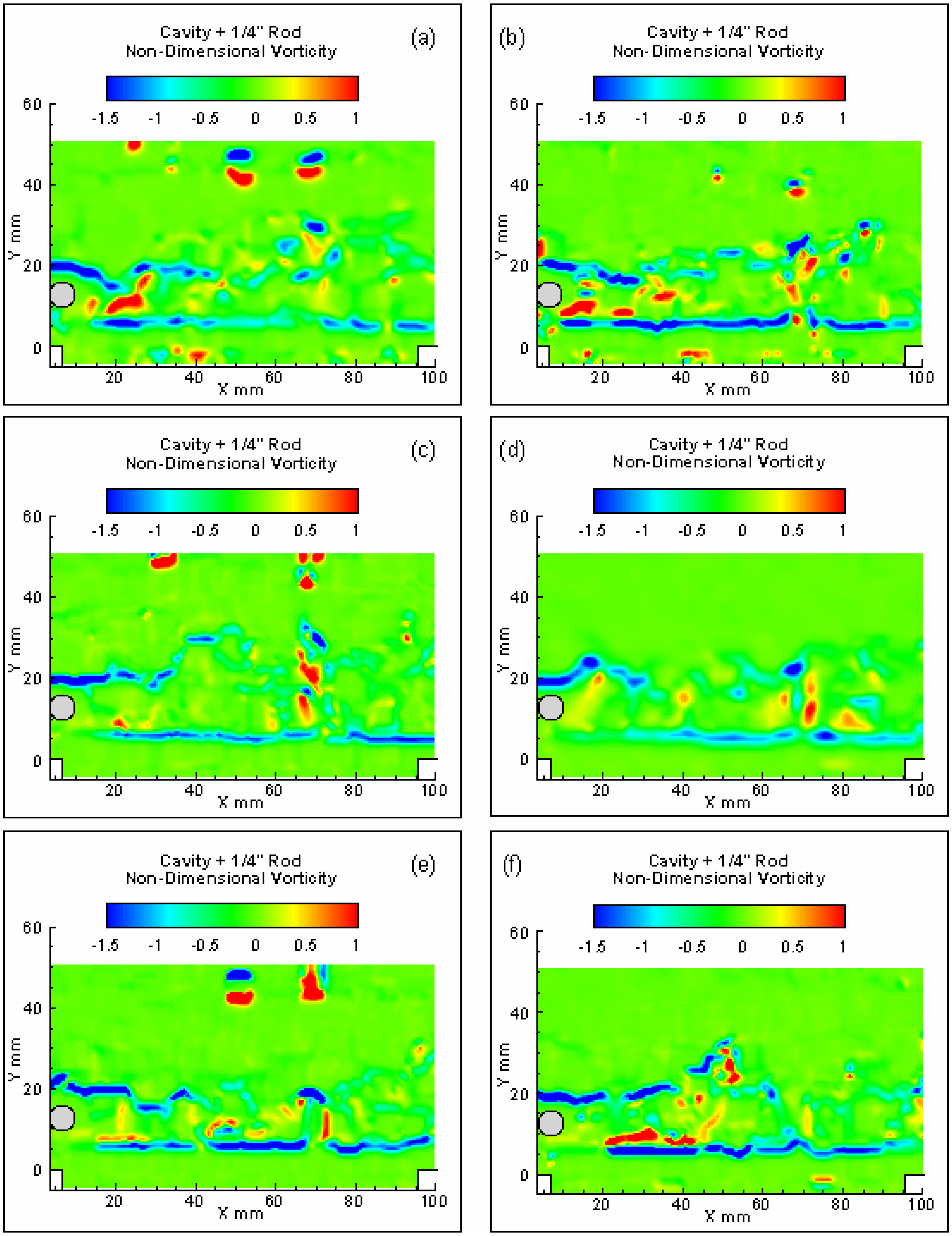


**Figure 53: Instantaneous vorticity contours of Cavity + 1/4"Rod at flow M = 0.50.**

# CHAPTER 5

# CONCLUSIONS AND RECOMMENDATIONS

## Conclusions

The effects of placing different diameter rods in crossflow above the leading edge of an L/D = 3.5 cavity, in an average subsonic Mach number flow of 0.52, and a nominal Reynolds number of $13.8 \times 10^6$ have been investigated. Flow conditions entering the tunnel test section were found to be less than desirable. However, satisfactory Frequency Spectra, velocity, and vorticity fields were obtained using dynamic pressure transducers and PIV.

Analysis of the results from this investigation, leads to the following conclusions:

a) Even with the non-uniform flow entering the tunnel, cavity flow processes were observed.

b) A 1/4" diameter rod positioned upstream of the cavity, near the edge in crossflow, affected the cavity shear layer by adding approximately 2.7 mm of loft onto the wake being shed from the rod. This visibly reduced the extent, and intensity, of vorticity at the rear wall of the cavity and resulted in suppressing the peak resonant amplitude by as much as 20.7 dB SPL (from a peak of 153.1 dB SPL down to a minimum of 132.4 dB SPL).

c) The 3/16" and 1/8" diameter rods in crossflow displayed similar shear layer and vorticity characteristics but to a lesser degree, and provided an average of 13.6 and 7.3 dB SPL of suppression respectively.

d) Considering the particular flow conditions observed in this investigation, the primary feature leading to the suppression of cavity tones was apparently the blockage and lofting effect from the rod, as opposed to a high frequency effect.

## Recommendations

To conduct further testing of this configuration at the design Mach number of the current supersonic nozzle, M = 1.8, or replace it with a subsonic nozzle and repeat a similar test program. This will eliminate the non-uniformity of the velocity profile entering the test section, and focus the efforts towards achieving acoustic suppression with high frequency effects.

It would be valuable if the timing signal from the synchronizer could be used to trigger the collection of spectral data so that it may be correlated to the flow field structures captured in the PIV images;

With regards to the variation of flow Mach number, the feasibility of developing a more precise controlling algorithm, or selecting a parameter other than the mass flow rate to be used as the operating condition setpoint, could be considered.

# LIST OF REFERENCES

[1] Rossiter, J.E., (1966), “Wind Tunnel Experiments on the Flow over Rectangular Cavities at Subsonic and Transonic Speeds.” Aeronautical Research Council R. & M. No. 3438.

[2] Heller, H.H. and Bliss, D.B., (1975) “The Physical Mechanism of Flow-Induced Pressure Fluctuations in Cavities and Concepts for their Suppression.” AIAA Paper 75 – 491, AIAA 2nd Aero-Acoustics Conference, Hampton, VA., March 24 – 26, 1975.

[3] Krishnamurty, K., (1955) “Acoustic Radiation from Two-Dimensional Rectangular Cutouts in Aerodynamic Surfaces.” NACA TN 3478.

[4] Roshko, A., (1955) “Some Measurements of Flow in a Rectangular Cutout.” NACA TN 3488.

[5] Plumblee, H.E., Gibson, J.S., and Lassiter, L.W., (1962) “A Theoretical and Experimental investigation of the Acoustic Response of Cavities in an Aerodynamic Flow.” WADD TR 61 – 75.

[6] Shaw, L.L., and Mcgrath, Lt. S., (1996) “Weapons Bay Acoustics – Passive or Active Control.” AIAA-96-1617-CP.

[7] Heller, H.H., Holmes, D.G., and Covert, E.E. (1971) “Flow Induced Pressure Oscillations in Shallow Cavities.” Journal of Sound and Vibrations 18(4), 545 – 553.

[8] Bilanin, A.J., Covert, E.E., (1973) “Estimation of Possible Excitation Frequencies for Shallow Rectangular Cavities.” AIAA Journal, Vol. 11, No. 3, 347 – 351.

[9] Tam, C.K.W., and Block, P.J.W., (1978) “On the Tones and Pressure Oscillations Induced by Flow Over Rectangular Cavities.” Journal of Fluid Mechanics, Vol. 89, Part 2, 373 – 399.

[10] Gauthier, C.R., (1990) “Experimental Study of Cavity Flow Oscillations with Upstream Mass Injection.” Master of Science Thesis, University of Tennessee, Knoxville.

[11] Ho, C-M., and Huerre, P., (1984) “Perturbed Free Shear Layers.” Annual Review of Fluid Mechanics, Vol. 16, 365-424.

[12] White, F.M., (1991) Viscous Fluid Flow – Second Edition, McGraw-Hill, New York.

[13] Betchov, R., and Szewczyk, A.B., (1963), “Stability of a Shear Layer Between Parallel Streams,” Phys. Fluids, Vol. 6, 1391-1396.

[14] Vakili, A.D., and Gauthier, C.R., (1991) "Control of Cavity Flow by Upstream Mass Injection." AIAA 22nd Fluid Dynamics, Plasma Dynamics, and Lasers Conference, AIAA 91-1645.

[15] Cattafesta III, L.N., Williams, D.R., Rowley, C.W., and Farrukh, S.A. (2003) "Review of Active Control of Flow-Induced Cavity Resonance." 33rd AIAA Fluid Dynamics Conference and Exhibit, AIAA 2003-3567.

[16] Wiltse, J.M., and Glezer, A., (1998) "Direct Excitation of Small-Scale Motions in the Free Shear Layer." Physics of Fluids, Vol. 10, No. 8, 2026 – 2036.

[17] Stanek, M.J., Sinha, N., Seiner, J.M., Pearce, B., Jones, M.I., (2002) "High Frequency Flow Control – Suppression of Aero-Optics in Tactical Directed Energy Beam Propagation & The Birth of a New Model (Part I)." 33rd AIAA Plasmadynamics & Lasers Conference, AIAA 2002-2272.

[18] Stanek, M.J., Raman, G., Ross, J.A., Odedra, J., Peto, J., Alvi, F. and Kibens, V., (2002) "High Frequency Acoustic Suppression – The Role of Mass Flow, The Notion of Superposition, and the Role of Inviscid Instability – A New Model (Part II)." 8th AIAA/CAES Aeroacoustics Conference & Exhibit, AIAA 2002-2404.

[19] Stanek, M.J., Ross, J.A., Odedra, J., Peto, J.W., (2003) "High Frequency Acoustic Suppression – The Mystery of the Rod-in-Crossflow Revealed." 41st AIAA Aerospace Sciences Meeting and Exhibit, AIAA 2003-0007.

[20] Panickar, P., and Raman, G., (2008) "Understanding the Mechanism of Cavity Resonance Suppression Using a Cylindrical Rod in Crossflow." 46th AIAA Aerospace Sciences Meeting and Exhibit, AIAA 2008-54.

[21] Panickar, P., and Raman, G., (2008) "Cavity Resonance Suppression using High Frequency Excitation: The Mystery of the Cylinder-in-Crossflow Revisited." 14th AIAA/CAES Aeroacoustics Conference (29th Aeroacoustics Conference), AIAA 2008-2853.

[22] TSI INSIGHT™ PIV Software Version 3.1 Instruction Manual (January 2000), TSI Incorporated, St. Paul, MN, 55164.

[23] Meganathan, A.J., (2000) "An Experimental Study of Low Speed Open Cavity Flows." Master of Science Thesis, University of Tennessee, Knoxville.

[24] Radhakrishnan, S. (2002) "An Experimental and Numerical Study of Open Cavity Flows." Doctor of Philosophy Dissertation, University of Tennessee, Knoxville.

[25] Smith, B.R., Welterlen, T.J., Maines, B.H., Shaw, L.L., Stanek, M.J., Grove, J.E., (2002) "Weapons Bay Acoustic Suppression from Rod Spoilers." 40th AIAA Aerospace Sciences Meeting & Exhibit, AIAA 2002-0662.

# APPENDIX

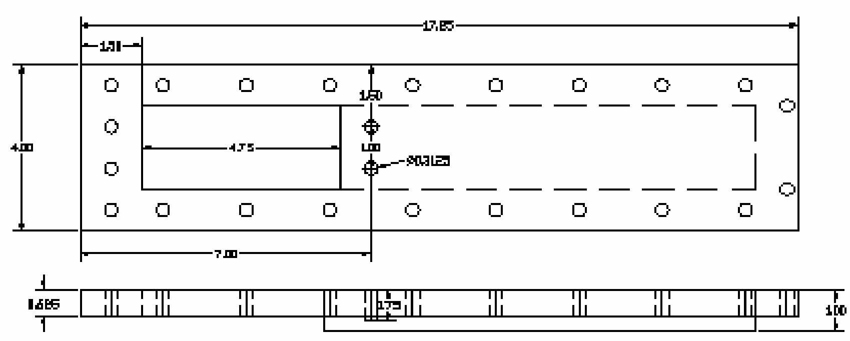


**Figure A. 1: Removable floor plate designed for L/D = 3.5 cavity with use of rod support block.**

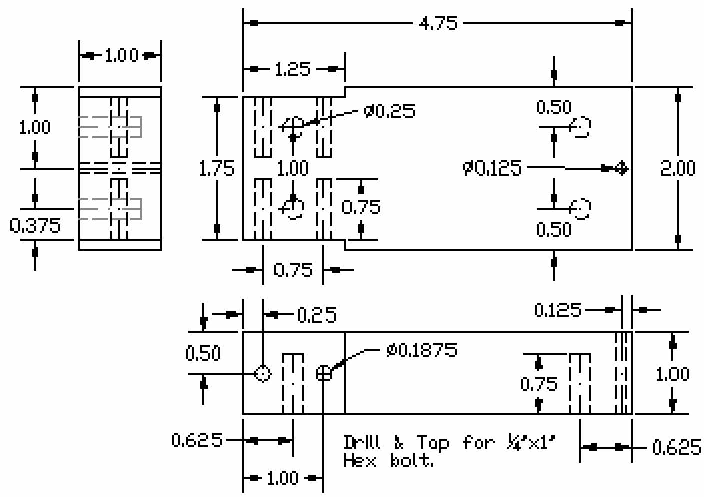


**Figure A. 2: Cavity filler block used in Phase 1 Clean Tunnel and Phase 2 Rod Signature.**

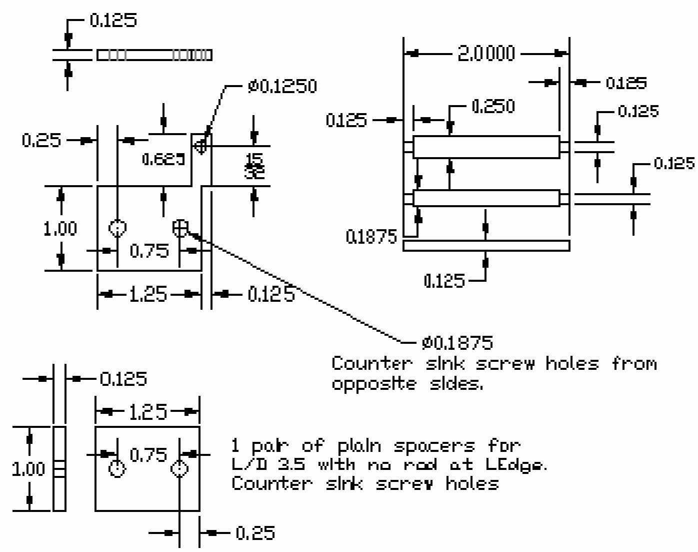


**Figure A. 3: Rod support plates used in Phase 2 and 4 to position cylindrical rods above cavity leading edge.**

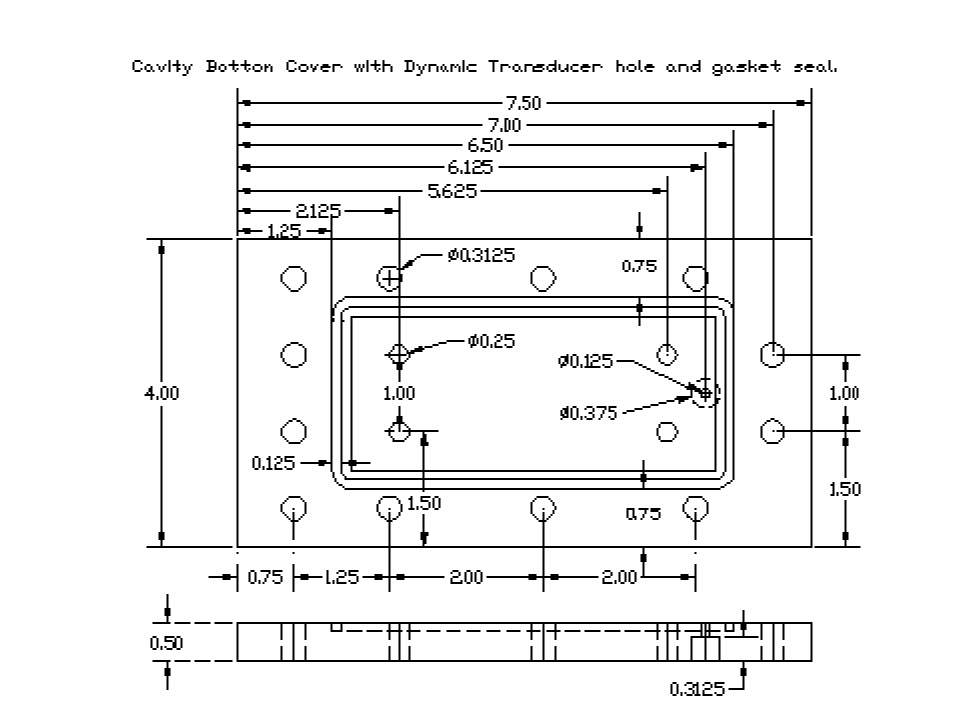


**Figure A. 4: Cavity bottom plate secured to the base of the removable floor plate in each configuration.**

# VITA

Richard David Loewen was born 22 October 1971 in Ashcroft, British Columbia, Canada to Clifford and Dianne Loewen. He spent all of his childhood years in Western Canada, graduated from Salmon Arm Senior Secondary School in June 1989, and in September of the same year followed in his Grandfather's footsteps and began a career in the Canadian Armed Forces.

Richard started out in the Canadian Navy as a Naval Electronic Sensor Operator, and after attending the Fisheries College at Memorial University in St. John's, Newfoundland, graduated with an Electrical Technology Diploma in 1993, and began his service as a Naval Electronics Technician. Having always wanted to be in the Air Force, Richard applied for, and in 1996 was accepted into a University Training and Commissioning program that led him to the Royal Military College of Canada in Kingston, Ontario, where he completed a Mechanical Engineering Degree and was commissioned as a Lieutenant in the Canadian Air Force.

Following successful completion of his Aerospace Engineering training at Borden, Ontario in 2001, Richard was posted to 12 Wing Shearwater, in Nova Scotia, Canada where he had the privilege to serve in several capacities within the aircraft maintenance environment of the Maritime Helicopter community. In 2006, Richard was accepted to enter a Post Graduate Training program at the University of Tennessee Space Institute, and in August 2008 successfully completed a Master of Science Degree in Aerospace Engineering.

Richard has been truly blessed with a beautiful wife, Sandra, and two wonderful daughters, Anna & Katie, all of whom thoroughly enjoyed their time in Tullahoma, Tennessee, and have since relocated to their Nation's Capital in Ottawa, Canada.